UNIVERSITY OF MIAMI

STRUCTURAL ANALYSIS AND FORM-FINDING OF MYCELIUM-BASED MONOLITHIC DOMES

By

Riccardo Andrea Baricci

A THESIS

Submitted to the Faculty
of the University of Miami
in partial fulfillment of the requirements for
the degree of Master of Science

Coral Gables, Florida

August 2016

UNIVERSITY OF MIAMI

A thesis submitted in partial fulfillment of
the requirements for the degree of
Master of Science

STRUCTURAL ANALYSIS AND FORM-FINDING OF MYCELIUM-BASED MONOLITHIC DOMES

Riccardo Andrea Baricci

Approved:

_____	_____
Landolf Rhode-Barbarigos, Ph.D. Assistant Professor of Civil Engineering	Antonio Nanni, Ph.D. Professor of Civil Engineering
_____	_____
Marco Savoia, Ph.D. Professor of Civil Engineering University of Bologna, Italy	Guillermo Prado, Ph.D. Dean of the Graduate School

BARICCI RICCARDO ANDREA (M.S., Civil Engineering)
Structural Analysis and Form-finding (August 2016)
of Mycelium-based Monolithic Domes

Abstract of a thesis at the University of Miami.

Thesis supervised by Professor Landolf Rhode Barbarigos.
No. of pages in text. (126)

As sustainability becomes an integral design driver for current civil structures, new materials and forms are investigated. The aim of this study is to investigate analytically and numerically the mechanical behavior of monolithic domes composed of mycological fungi. The study focuses on hemispherical and elliptical forms, as the most typical solution for domes. The influence of different types of loading, geometrical parameters, material properties and boundary conditions is investigated in this study. For the cases covered by the classical shell theory, a comparison between the analytical and the finite element solution is given. Two case studies regarding the dome of basilica of “San Luca” (Bologna, Italy) and the dome of sanctuary of “Vicoforte” (Vicoforte, Italy) are included. After the linear analysis under loading, buckling is also investigated as a critical type of failure through a parametric study using finite elements model. Since shells rely on their shape, form-found domes are also investigated and a comparison between the behavior of the form-found domes and the hemispherical domes under the linear and buckling analysis is conducted. From the analysis it emerges that form-finding can enhance the structural response of mycelium-based domes, although buckling becomes even more critical for their design. Furthermore, an optimal height to span ratio for the buckling of form-found domes is identified. This study highlights the importance of investigating appropriate forms for the design of novel biomaterial-based structures.

ACKNOWLEDGMENT

I would like to express my deepest gratitude to my advisor, Landolf-Rhode Barbarigos, for his guidance, support, valuable discussions during my MS studies here at the University of Miami.

I would also like to greatly acknowledge my committee members, professor Antonio Nanni (University of Miami) and Professor Marco Savoia (University of Bologna), as well as Professor Edward Segal for his insightful comments during the discussion of this thesis.

I am also grateful to Omar Aloui and Omid Gooran for their generous help with the finite element software Abaqus. Finally I also wish to express my appreciation to Andrea Galletti and Eleonora Spisni for their support and friendship.

TABLE OF CONTENTS

LIST OF FIGURES

Page

Chapter

LIST OF TABLES

PUBLICATIONS

The content of this MS is part of a paper submitted at the ASCE/SEI 2017 Structures Congress entitled: “Preliminary Investigation of Thin-Shell Mushroom Biomaterial Roofs”.

Chapter 1: Introduction

Shell structures always had an important role for architecture and engineering. Besides their aesthetic value, they also possess interesting mechanical properties and they are able to resist loads efficiently. Due to their curvature, shell structures are able to decompose stresses in multiple directions combining membrane and bending action and consequently enhancing the overall load carrying capacity. However, shell behavior is really susceptible to shape changes and other parameters such as support conditions. In fact, even the smallest change in the geometry or in the boundary conditions can completely alter the response of the structure. Moreover, multiple geometrical solutions can be considered for shell design, promoting different advantages and disadvantages as well as structural performance. Thanks to their extraordinary but also often unpredictable behavior, shells are termed the “prima-donnas” among structures. Therefore, the goal of the designer is to find the shell shape which, according to the given design constraints, optimizes the mechanical behavior without sacrificing the aesthetic value. Although industrialization and research have made materials less expensive, labor costs have increased in the developed countries. As a result, shells have lost popularity and the number of applications has diminished favoring other type of large-scale constructions since 1960s. However, new construction techniques based on pneumatic air-form may revamp shell structures. These new construction techniques allow to obtain various shell shapes without using the conventional formwork and false-work, which usually represents a major component in the construction cost of shell structures. Moreover, nowadays numerical tools give great support to designers. The development of finite element software has made possible the structural analysis of complex shell shapes that

go beyond the limits of the classical shell theory. However, the finite element results should always to be questioned and rightfully interpreted. The aim of this study is to investigate analytically and numerically the mechanical behavior of monolithic hemispherical and form-found domes, employing a new biodegradable material, based on mycological fungi, with very limited structural applications. In architecture and engineering, the production of concrete is particularly energy intensive and responsible for the emission of a significant amount of CO_2, as well as construction wastes. Consequently, sustainability is becoming a key aspect for civil structures to the point that it occupies a prominent role in the design. Thanks to its low energy and environmental friendly production process, as well as biodegradable nature, mycological fungi opens new horizons and may represent a valid alternative construction material. However, due to its low stiffness in situations where high loads are involved, such as civil structures, the mechanical properties of mycological fungi may not be sufficient to provide the desired structural response. Therefore, the first application of such material should focus on light-weight structures, such as shells. Since the mechanical behavior of shells is based on their shape, it can be improved through “form-finding”. Form-finding describes the process of identifying an optimal geometry in static equilibrium with a design loading under given constraints. This technique has become very popular in the last decades and has produced remarkable results, both from structural and aesthetic point of view. Hence, optimizing the material use through “form-finding” could open a realm of biodegradable shell structures.

Chapter 2: State of Art

2.1 Literature review

Shell structures, such as domes, have a long historical tradition which started more than two thousand years ago. The first pioneers of this structural system were the Romans and the first shell, in particular a dome with an opening, was the Pantheon (Fig. 2.1) realized by the architect Agrippa in 27 B.C.

Figure 2.1. The Pantheon [1]

Although the Romans may have not been aware of the exact mechanics governing shell structural behavior, they were able to understand the potential load-carrying capacity of shells. Pantheon is still considered a masterpiece of architecture and civil engineering to the point that its outstanding features inspiring generations until this day. Another emblematic shell structure is the famous “Dome of Santa Maria del Fiore” (Fig.2.2) in Florence realized by Filippo Brunelleschi in 1461. It has been the biggest dome of the world and it is still the biggest masonry dome ever built. Due to the extreme importance it has played in the development of architecture and the modern conception of building,

the dome of Brunelleschi is still considered the most important architectural work ever realized in Europe from the Roman age.

Figure 2.2. The Dome of Brunelleschi [2]

The passage from stocky to thin shell structure took place with the beginning of the last century, when a deeper knowledge about shells behavior started to develop and an extensive literature was made available to engineers. A structure that reflects this transition is the Leipzig Market Hall (Leipzig, Germany 1929). In the context of thin shell structures, the most relevant figures are Anton Tedesko (1903-1994), Pier Luigi Nervi (1891-1979), Eduardo Torroja (1891-1961) and Felix Candela (1910-1997). The work of Tedesko was fundamental for the historical development of thin shell structure in United States. His article in 1932 was the first to introduce shell structures in American literature. According to Billington [3], the contribution of Tedesko can be summarized by three thin shell concrete structures which were also the first of their types realized in Unite States: the barrel shell roof of Brook Hill Farm Dairy Exhibit (Chicago, Illinois, 1933), the hemispherical dome of Hayden Planetarium (New York City, New York

1934), and the short barrel shell of Hershey Sports Arena (Hershey, Pennsylvania, 1936) (Fig.2.3).

Figure 2.3. The Hershey Sports Arena [4]

Pier Luigi Nervi's work is equally important to Tedesko. According to "Costruire Correttamente" [5], the main contribution of Nervi to the history of thin shell structure and in general in the field of reinforced concrete was the invention of ferro-cemento. This composite material consists in a high quality cement mortar which covers a combination of few bars and layers of steel mesh. The outstanding features of "ferro-cemento" allowed Nervi to realize several structures characterized by daring technical-structural solutions and extraordinary elegance. Among his best-known works are the stadium Artemio Franchi (Florence, Italy, 1931), the hangar for the Italian aviation (Orbetello, Italy, 1940), the Turin Exhibition saloon (Turin, Italy, 1949) (Fig. 2.4), the Thompson Arena of Dartmouth College (New Hampshire, 1962), the Cathedral of St, Mary (San Francisco, California, 1971) and the Unesco venue (Paris, French,1958).

Figure 2.4. The Turin Exhibition saloon [6]

Another pioneer of the thin shell structures was the engineer and architect Eduardo Torroja. His building technique influenced all the following generations of architects and engineers nowadays. Two of his most famous works are the Hipodromo de la Zarzuela (Madrid, Spain, 1931) and the Algeciras market (Algeciras, Spain, 1933). Another key character in the development of shell structure was Felix Candela. Candela is probably the most famous designer of hyperbolic paraboloids, to the point that his name became a synonymous of those shells. His works were based on the concept that an adequate strength for a structure should be achieved by the optimization of the shape rather than addition of mass. The most famous works of Candela are the Cosmic Ray Pavilion (Mexico city, Mexico 1950), the church of La Virgen Milagrosa (Mexico City, Mexico, 1953), the Manantiales restaurant (Xochimilco, Mexico, 1958) and the Queensgate Market (Huddersfield, Great Britain, 1970) (Fig.2.5).

Figure 2.5. The Queensgate Market [7]

The overview of the history of thin shell structures highlights the potentialities both from a structural and aesthetic point of view. However, as it has been already mentioned, the global behavior of shells sometimes may be difficult to predict and this fact makes the design more complex respect to standard constructions. A simplified analysis can be conducted by considering a series of assumptions which bring to the formulation of the membrane theory. Thanks to the work of Tymoshenko, “Theory of Plates and Shells” [8], the global behavior of thin shells was determined through analytic equations. The theory is based on a linear analysis predicting the distribution of the stresses, as well as the level of deformations. With the development of finite element software, it has been possible to compare the analytical with the numerical results. This is the content of two studies: “Analysis Methods for Thin Concrete Shells of Revolution” by A. Hauso [9] and “ A Finite Element Analysis of Monolithic Domes” by N. South [10]. Nonetheless, both

studies didn't take in consideration buckling as a type of failure. Buckling is a critical aspect, especially for shells, such as domes, where instability is a main issue, which often governs the design. Buckling is defined as an instability which can result to a failure mode. Although the buckling of shells has been treated extensively, just few cases have been formulated analytically. In fact, the most part of the studies on buckling are case-dependent and they combine theoretical predictions with experimentally determined correlation factors. This is particularly true for domes, where the buckling theory covers only the load case of a uniform external pressure. The study "Buckling of Spherical Shells" by Taylor and Francis Group, LLC (2008) [11] focuses on this load case for complete spherical configurations, hemispherical heads and shallow spherical caps. Even though the study recognizes the discrepancy between theory and experiments, the obtained results are based on numerical methods solely. They identified the buckling loads and the related correlation factors for different geometries and materials considering also the effect of initial imperfections. The study "Numerical Calculations of Stability of Spherical Shells" by T. Niezgodzinski et al (2010) [12] analyzed the stability of thin-walled spherical shells under uniform radial pressure through static and dynamic analyses. The authors also took into account different geometries and boundary conditions. The results obtained with FE calculations were compared to the available results obtained with analytical and other numerical methods, showing a good conformity [12]. Moreover, they found that the initial imperfections have a strong influence on the deflection modes, but not on the values of the corresponding buckling loads. In fact, the maximum difference between them resulted to be around 3%. Also the study "Buckling Analysis of Concrete Spherical Shells" by I. Mekjavic [13] focused on the buckling under

uniform external pressure of concrete spherical shells by taking into account large deflection and plasticity effects. A non-linear analysis with and without geometrical imperfections was performed numerically revealing that a lower value of the critical buckling load compared to the theoretical one, which is valid only in linear analysis.

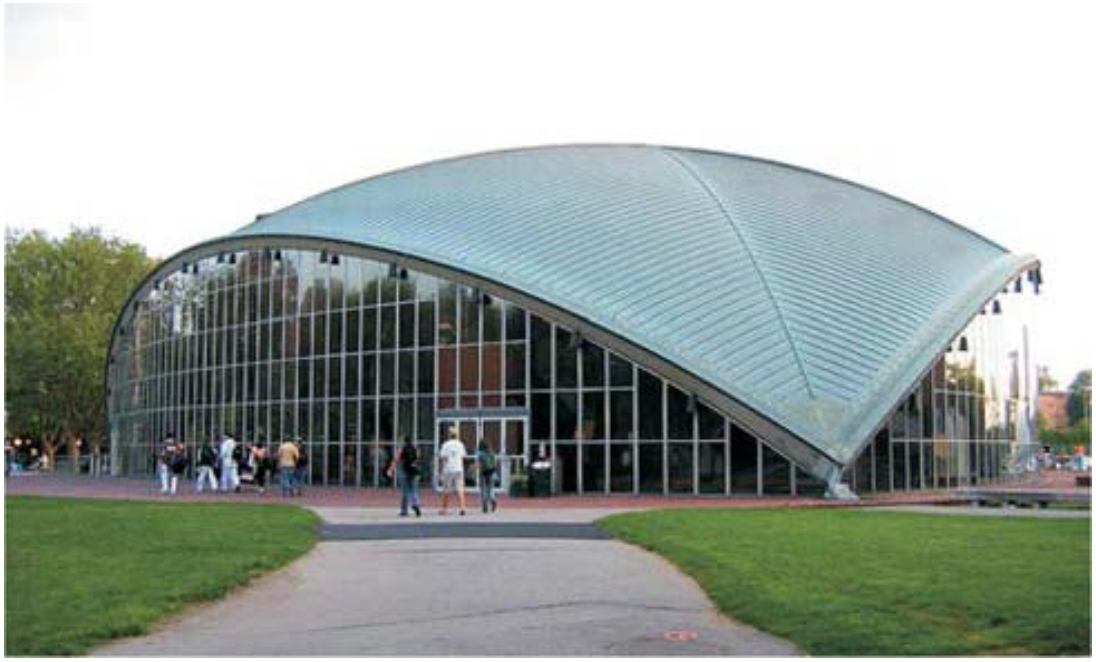

Figure 2.6. Kresge-MIT Auditorium, Boston, USA [13]

A real experiment on a spherical concrete cap was conducted in the study " Short-term behavior of shallow thin-walled concrete dome under uniform external pressure" by Z.T. Chang et al (2010) [14]. The dome, which was without reinforcement, was subjected to short-term loading by pressurized water entrapped in a rubber bladder. The testing showed how the dome failed due to a non-axisymmetric buckling mode well before the concrete reached its compressive strength [14]. From previous experiences in buckling it was known that there is a big discrepancy between the theoretical and the experimental results. Therefore symmetric and asymmetric initial imperfections were considered as a part of the non-linear deflection theory. In fact, the value of experimental failure pressure

was found to be only 31% of the classical theoretical, but really closed to the “lower” buckling load derived by Von Karman and Tsien [15]. Moreover, the experimental results identified the location of the failure where a significant non linearity was registered as well as bending effect. Although all the aforementioned studies investigated buckling, employing analytical and numerical methods as well as experiments, they only focused on one type of geometry (spherical domes) under one type of loading (uniform external pressure) and based on a common structural material (concrete). A more extensive study, “Buckling of Thin-Walled Doubly Curved Shells” was conducted by NASA (1969) [16]. The study focused on spherical caps under uniform external pressure, concentrated load at the apex, ellipsoidal shells under both external and internal pressure, toroidal shells and shallow toroidal segments under uniform external pressure, complete oblate spheroidal shells and torispherical bulkheads under uniform internal pressure. In this study the reduction of the buckling loads caused by initial imperfections and boundary conditions was taken into account by multiplying the theoretical buckling loads by a correlation factor in order to obtain a lower-bound conservative estimate [16]. Although different shell geometries were treated, the concept of optimization of the shapes to increase the performance of the mechanical response was not explored. This is the main idea behind the form-finding process. According to “Form Finding and Optimization of Shell Structure” [17], Form-finding can be defined as a forward process in which parameters are controlled to find an “optimal” geometry which is in static equilibrium with a design loading [17]. An expert in physical form-finding of shells was Heinz Isler. The paper “Concrete Shells Derived from Experimental Shapes” [18] summarizes his experiences in

design and construction of form-found shells using pneumatic, hanging and flow-generated shells.

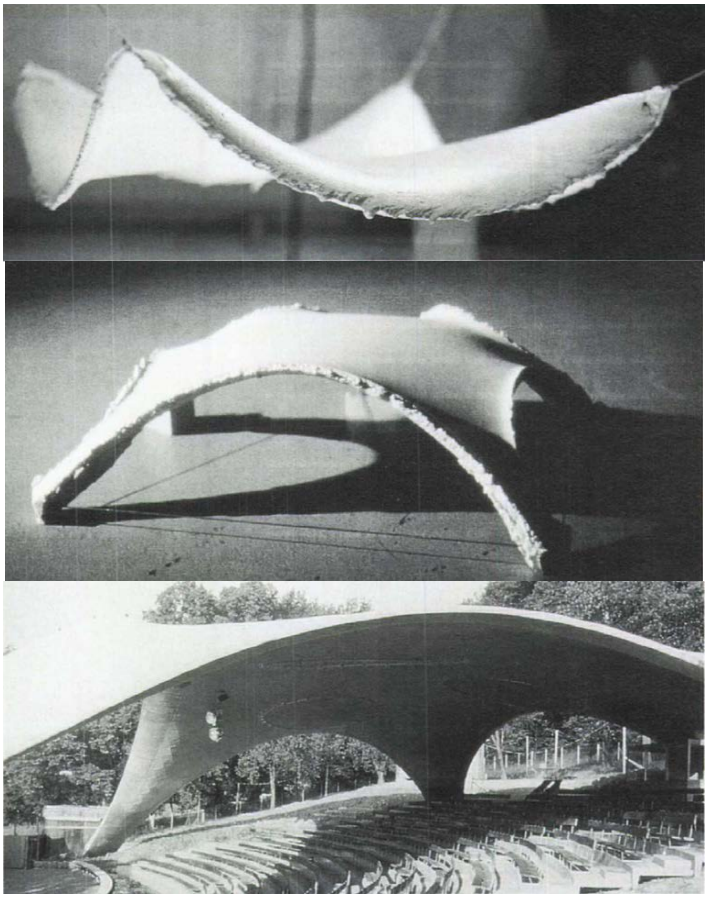

Figure 2.7. Open-air theater, Grotzingen, Germany shape found by hanging model [18],

Shells are typically made of concrete where formwork and cladding are two principal problems encountered during their construction process. Steel and glass were considered as construction materials in “Finding the Form of an Irregular Meshed Steel and Glass Shell Based on Construction Constraints” by S.Adriaenssens et al [19],. The form-finding process was based on two principal construction constraints: the height and the maximum bearing capacity of the existing historic masonry walls [19]. Even though the principle of inverting hanging models is the most popular application of the form-finding process, the optimization of the shape can be conducted also considering different design objectives.

The paper “Form-Finding of Shells by Structural Optimization” by K.-U. Bletizinger et al (1993) [20] analyzes different objective functions, such as minimum cost, minimum weight or minimum natural frequencies, where the criterion for optimality is not the generating rule itself, as it happens for hanging models. According to the author, in order to reach the best compromise between multiple objective functions, methods of multi-criterion optimization have to be applied to leading to non-linear problems with possible multiple solutions. In terms of non-linearity and multiple solutions, a similar situation is found when the optimization process considers multiple load cases. This is the case of the study “On Shape Finding Methods and Ultimate Load Analyses of Reinforced Concrete Shells” by E. Ramm [21], where the study focuses on the compromise between multiple load cases. Moreover, the study shows how different form-finding approaches can lead to the same design solution if the initial constraints are the same. This is the case of pre-stressed cable structures where the optimization can be conducted both with so-called force density method and dynamic relaxation. Since the principles of form-finding can be applied both to cables and shells, it seems logic that the same rules are valid also for a combination of them. This is the case of grid shell. According to the study “Form-Finding of a Grid Shell in Composite Materials” by C. Douthe et al (2008) [22], grid shells can be defined as “that kind of structures with the shape and the strength of a double-curvature shell, but made of a grid instead of a solid surface” [22]. For grid shell the optimization process is usually based on dynamic relaxation, where the equilibrium of the structures depends on damped vibrations. However, even though the form-finding processes discussed in the aforementioned studies optimize the shape according to certain criteria, the effects of such optimizations on the buckling behavior are rarely taken into

consideration. The study “Shape and Size Optimization of Concrete Shell” by A. Tomas et al (2010) [23] focuses on the optimization of a hyperbolic paraboloid (hypar) concrete shell and its impact on the overall instability of the structure.

Figure 2.8. Hypar shell structure at the entrance of the Universal Oceanographic Park(Valencia,Spain) [23]

The optimization in this study involved the thickness and the geometry as variables of the problem. According to the author, the final form-finding process led to a reduction of the maximum deformation, as well as an improvement of the mechanical and buckling behavior. In the examples studied, the buckling loads were found to be approximately double of the initial values [23]. Another interesting study, “Buckling Behavior of Symmetric Arches” by S. Qaqish (1977) [24] analyzed the buckling behavior of hemispherical, parabolic and catenarian arches under different types of loading and boundary conditions. In this work a parametric study on the geometries was conducted to find the ratio between the height and the span that maximizes the buckling load. According to the author, circular arches can resist the highest total loads at buckling, followed by the catenarian and then the parabolic arches, when the height-to-span ratio is equal to 0.3 for all of them [24].

2.2 New trends for shells

2.2.1 New construction methods: Pneumatic air-form

The construction process of monolithic domes has always been characterized by a high cost relating to the production of formworks and false-works. This is because in the last century, differently from the price of the construction materials, the labor cost has increased exponentially. As a result, in the last 30 years the realization of shells has significantly reduced. However, newly presented construction techniques based on pneumatic air-forms have the potential to revamp shell constructions. These new construction methods are intended for concrete shells of various shapes and thus could be also employed for shells composed of new materials. An application based on pneumatic air-form was developed at the institute for Structural Engineering at Vienna University of Technology. The main idea behind this construction technique is to cut a flat hardened concrete plate in segments like an orange and to transform it in a double-curvature surface thanks to the use of an air-supported formwork and post-tensioned cables [25]. The use of pneumatic air-form combined with shotcrete was also investigated. According to this method the construction process begins with the placement of a ring beam footing and the pouring of a circular steel-reinforced concrete slab floor [26]. After that, in many cases the following step is the realization of a stem wall to confer to the dome a better looking. Then, an air-form is attached to the ground and inflated thanks to the use of giant fans, creating the future final shape of the dome. Once the air-form is inflated, the next step involves the employment of treated wood in the interior of the dome to attach properly windows and doors. After that, approximately three inches of polyurethane foam is sprayed on the rest of the air-form and a grid of steel reinforcing rebar is embedded in

the foam thanks to the use of special hooks [25]. Finally, a layer of shotcrete with variable thickness is sprayed into the interior surface of the polyurethane foam, embedding the steel reinforcement.

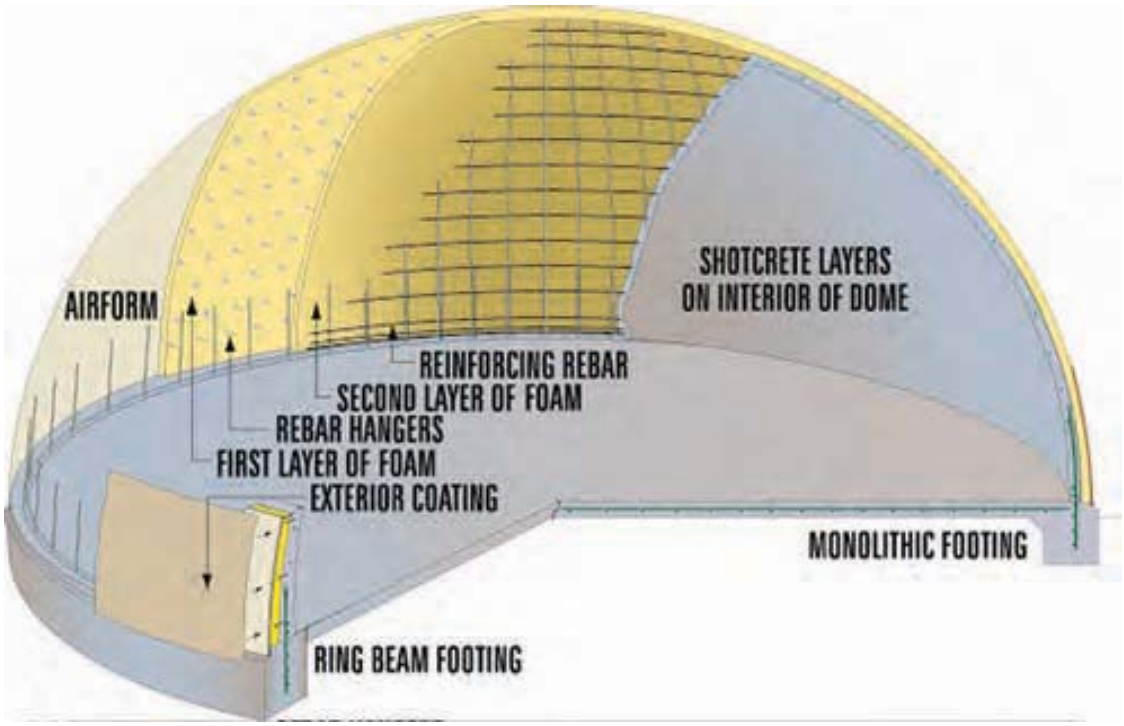

Figure 2.9. Employed materials for the monolithic dome construction [27].

Besides achieving an excellent mechanical behavior, the resulting monolithic domes offer also great level of insulation mainly due to the foam that allows the structure to maintain a constant the indoor temperature. In fact, according to C. Lanham, monolithic domes can save up to the 50% of the cost for heating and cooling respect to conventional buildings of the same size. Moreover, the construction technique previously described provides a fast, labor- and material-saving building method in comparison to construction method with formwork and false-work [25].

2.2.2 New materials: Mycelium

Shells structures are traditionally made of concrete. However, the development of new biodegradable materials could provide an alternative solution for future shell structures. Mycological fungi are natural composites materials which offer a series of benefits respect to the traditional construction material, such as carbon capture and storage, low cost of production, low usage of natural resources and low environmental impact. The sustainability nature of mycological fungi is thus opening new horizons in a large variety of applications, especially in those where the use of composite materials has become too expensive in terms of raw material and production process. The vegetative part of fungi is named mycelium and is characterized by a fast and safe growing process. It also serves as the matrix for a new generation of natural composites, which can potentially replace traditional polymeric materials for applications such as insulation, packing and sandwich panels [28]. In addition, mycelium material is particularly lightweight and has shown relatively good mechanical performances, especially in compression. For this specific reason, it has been decided to investigate the use of mycelium in civil structures, especially in those types of constructions that work essentially in compression, such as domes. A recent study demonstrated that its strength decreases with the increase of the moisture content [28]. Therefore, coatings might become essential in guaranteeing long term consistency and performance. From a biological point of view, mycelium resembles to a carbon-based network of trusses. It is composed by hyphae, which grows from the inoculation of a mycelium fungal strain spore into a cellular material [29]. Another peculiarity of mycelium material is its fast growth rate that potentially never stops if sufficient nutrients are available. One of the oldest and largest mycelium growth is

situated in Oregon, it is more than 2000 years old and it covers an area of more than 2400 acres. The mycelium hypae network exerts the important functions of growing and seeking new feed-stock, of recognizing and transporting nutrients, and of transmitting chemical signaling mechanism which regulate several other functions. The growth and nutrient harvesting are achieved by the secretion of digestive enzymes, dismantling macro-molecules into components than absorbed using a diffusion gradient or by transport mechanisms [28]. The skeletal structural of the mycological fungi instead, is achieved thanks to chitin composed of polysaccharides which confers stiffness to the cellular structure.

Material properties

The mechanical behavior of natural composite materials is difficult to describe because of their heterogeneous and anisotropic properties. This is true especially for mycological fungi, due to the fact that there are different species and different ways to produce it. However, previous studies demonstrated that the mechanical behavior of mycelium can be predicted by looking at the behavior of open-cell foams. A cell is defined as “Open-cell” when it does not have cell walls, but only beams forming cell edges [28], allowing liquids and gasses to pass easily through it. Depending to the composition, foams are characterized by different stress-strain curve showing usually a different behavior in tension and compression. The curves associated to the compressive or tensile states vary according to the nature of foam, which can be elastomeric, elastic-plastic or brittle. Typical stress-strain curves of foams are shown in Fig. 2.10

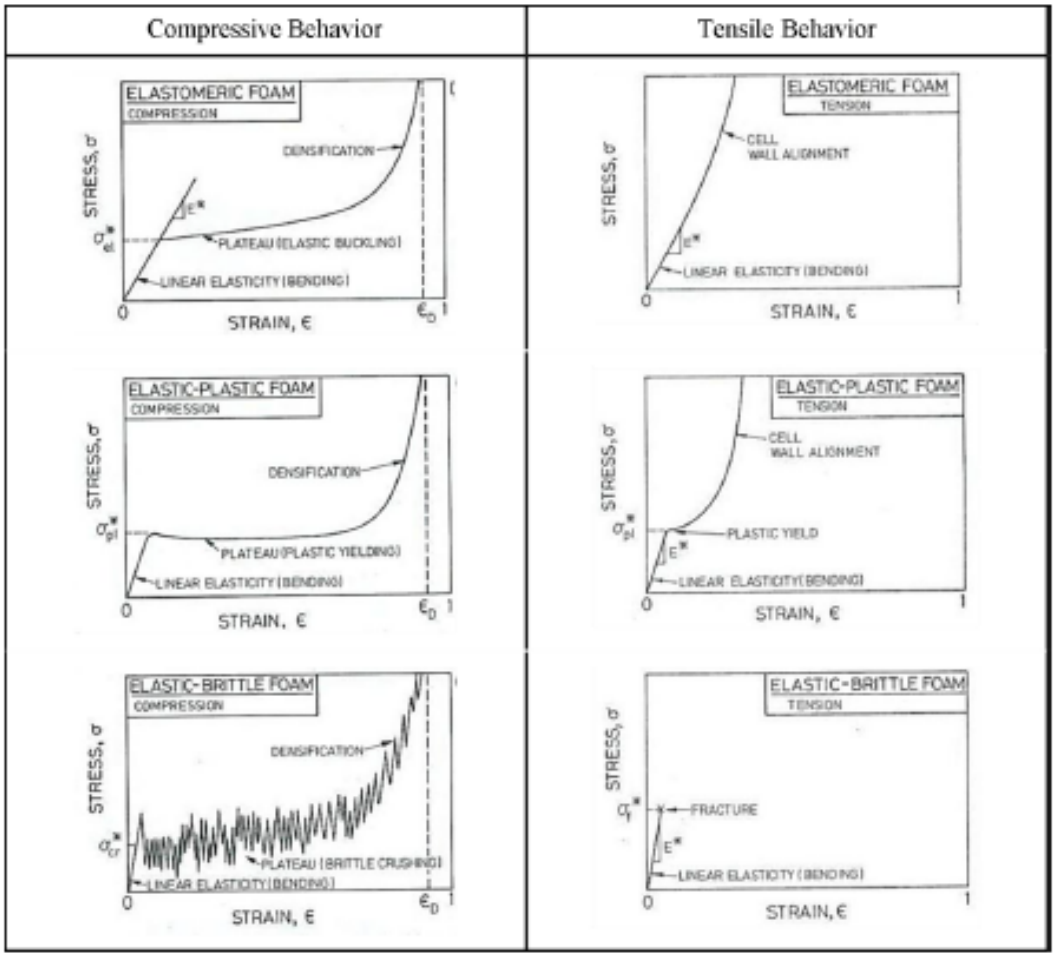

Figure 2.10. Typical stress-strain behavior in foams [28]

In each compressive curve, it is possible to distinguish the following three zones: linear elastic, plateau and densification. The first one represents the elastic bending of the cell edges and stretching of cell walls (if present). The second one occurs as the cells begin to collapse, via elastic buckling (for elastomers), plastic yielding (for elastic-plastic materials) or crushing (for brittle materials). The third one occurs when the cells are completely collapsed, the solid material is compressed and the stiffness increases to fracture during the densification region [28]. Each tensile curve starts with a linear-elastic region, but after the behavior varies depending on the nature of the foam. It is important to underline that some foams demonstrate brittle behavior in tension, but elastic-plastic

behavior in compression [30]. In order to be as much conservative as possible, in this study the mycelium material considered is assumed linear and brittle with the material properties presented in Table 2.1. Since for mycological fungi the Poisson ratio is difficult to define, an average value equal to 0.25 is also assumed.

Table 2.1. Material properties of mycelium. The values have been chosen according to [28] [31].

MATERIAL PROPERTIES OF MYCELIUM				
Density (kg/m^3)	**Tensile Strength (kPa)**	**Elastic Modulus (kPa)**	**Compressive Strength (kPa)**	**Poisson Ratio**
130	17	690	55	0.25

Table 2.1 also reveals that the mechanical properties of mycological fungi are lower compared with traditional dome construction materials, such as concrete and brick, which are discussed in the following chapters.

Production Process

Mycelium fungi usually grows under controlled conditions without light, water or petrochemicals. After an adequate level of growth, it is possible to stop the process by holding the material at a higher temperature. The heat treatment usually requires a temperature of 220 °C for 120 minutes [28]. In order to reduce the moisture content from 60-65% to10-20%, a convective heating based on solar dryers or renewable energy sources can be applied during the post-processing phase. The principal steps of the production process are summarized in the Fig. 2.11:

Figure 2.11. Principal steps of the production process of mycelium material [28].

According to the container shape employed, mycelium elements can be produced in different shapes, such as simple rectangular block molds. A hard chitin skin is automatically formed when mycelium comes into contact with non-porous, inorganic materials preserving the moisture and the nutrient content [28].

Applications

Mycological fungi play a fundamental role in our ecosystem. They are actually able to recycle carbon and minerals and they are involved in the nitrogen-fixing cycle. They also have an extend range of applications including human consumptions (when they are edible), environmental and biological control, capture and safe removal of heavy metal contaminants and even medical uses against cancer [28]. Since mycelium is biodegradable, it represents also a great sustainable option that can substitute synthetic materials or even structural material. In fact, mycelium is currently commercialized for packaging materials, insulation, structural insulating panels and acoustical tiles [31]. In architecture, one of the first prototypes using mycelium based building blocks was realized in Germany (Fig.2.12):

Figure 2.12. Mycotectural Alpha by Professor PG Ross exhibited

at Kunsthalle Dusseldorf as part of the Eat Art Exhibit 2009 [28].

The first large scale application of mycelium was “Hi-Fi” (Fig.2.13), a circular tower made of organic bricks situated in Moma’s PS1 courtyard. The structure was designed for the Young Architects Program of Moma by architect David Benjamin, who collaborated with the company Ecovative, responsible for the production of the materials.

Figure 2.13. Illustration of Hi-Fi [32]

Since nowadays civil engineering is oriented towards fast, cheap and sustainable construction and production processes, mycological fungi represents a great material for future applications. However, further investigations on its material properties need to be performed.

Chapter 3: Structural Analysis

3.1 Thin shells theory

3.1.1 General Introduction

Shell structures are curved surface structures characterized by a particular geometry, in which one dimension, the thickness, is significantly smaller compared to the other two. In civil engineering and architecture, shells have been used to cover large span areas without the use of columns. The study developed in the following chapters is concentrated on shells of revolution and in particular on hemispherical domes. Such shells are obtained by rotating a planar curve around an axis, called meridian axis, situated in the meridian plane. Their geometry is completely defined by the thickness and the shape of the middle surface. As a definition, a shell can be considered thin when the ratio between its radius and its thickness $\frac{R}{t}$ is in the range between 20 and 1000. Another key-concept is the radius of curvature which gives a quantitative measurement of the curvature of the shell in the two principal directions. It is possible to derive analytical solutions which are valid only in specific configuration defined by the radius of curvature.

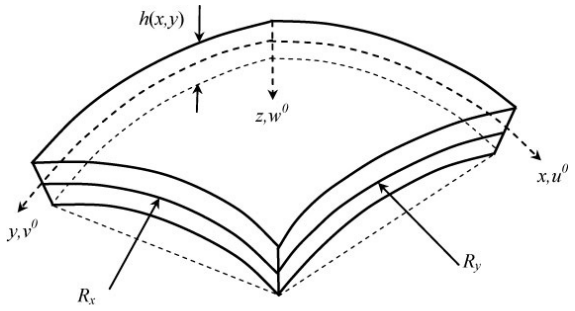

Figure 3.1. Radius of curvature and geometry of shells [3]

The study of thin shell behavior typically requires the understanding of two separate theories: the membrane theory and the bending theory. The first one describes the actions of the membrane forces, while the second one focuses on the effects of edge disturbances.

In few cases, an approximate solution in terms of stress and strain can be reached by solely using the membrane theory.

3.1.2 Definition of shells by the Gaussian Curvature

The Gaussian curvature allows the definition of shells in a more general way and it can be defined as: $$K = \frac{1}{r_x r_y},$$

where r_y and r_x represents the principal radii of curvature [3]. According to sign of the Gaussian curvature, it is possible to extrapolate useful information about the geometry and the load-carrying capacity of shells. Figure 3.2 illustrates the influence of the curvature on the geometry of three types of curved surface, respectively “saddle surface”, a cylinder and a sphere.

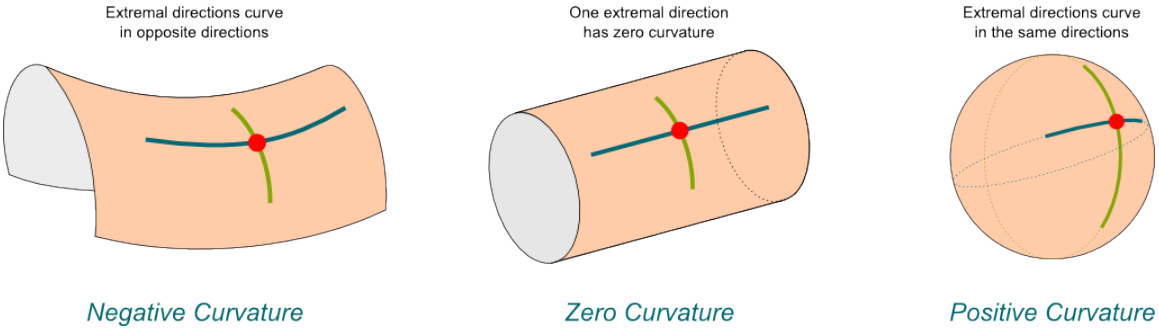

Figure 3.2. Shells and their Gaussian Curvature [33]

This study has been concentrated on synclastic surfaces, such as domes, characterized by a positive curvature. For this type of shells, the edge disturbances tend to damp rapidly. Therefore the membrane theory is sufficient to describe their global behavior.

3.1.3 Simplified Assumptions

A simplified shell analysis can be performed by considering more elementary forms such as arches, rings cantilevers and beams. In fact, a thin shell concrete structure can be

thought as a combination of such elements if it is possible to justify this equivalence. To make this possible, it becomes necessary to refer to the Kirchhoff-Love assumptions:

- **Geometrical linearity:** The strain and displacement are assumed to be small. Equilibrium is valid only for the undeformed configuration.
- **Physical linearity:** The material is elastic isotropic and homogeneous satisfying Hooks law.
- **Thin shell:** It can be defined by its middle surfaces, as halfway between the inner and the outer edges of the shell. Plane cross sections remain plane and vectors normal to the middle surface remain normal after deformations.

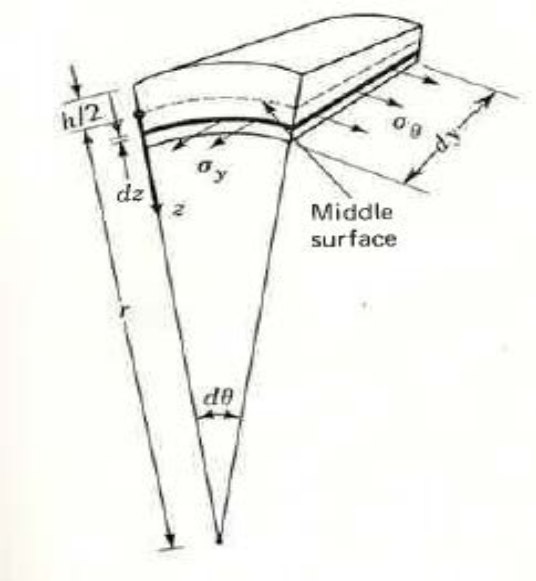

Figure 3.3. Definitions of thin shells [3]

Furthermore, for domes loaded symmetrically with respect to their axes the amount of stress resultants (forces per unit length of middle surface) are simplified by symmetry in the following: $N_\theta \, dy = \int_{-h/2}^{h/2} \sigma_\theta \, dz$, where:

N_θ is the force per unit length of middle surface

h is the thickness of the surface element

σ_θ is the internal force in the θ direction

And stress couples (bending moment per unit length of middle surface):

M_y r dθ = r dθ $\int_{-h/2}^{h/2} \sigma_y$ z (1 - $\frac{z}{r}$) dz , where:

M_y is bending moment per unit length of middle surface

r is the radius of curvature

σ_y is the internal force in the y direction

z is the arm of the internal force σ_y

3.2 Analytical method: Membrane theory

3.2.1 Assumptions

The Membrane theory is sufficient to describe the behavior of thin shell structures, such as domes. The theory is based on the concept that arbitrary loads can be carried solely by membrane forces. This becomes true when the following assumptions are added to the ones mentioned in the previous section:

- Bending and shear stiffness are very small, therefore they can be neglected
- The shell's surface is C_2 continuous
- Rapid or abrupt changes in shell thickness are excluded
- Concentrated loads cannot be treated
- Edge forces are tangential to the surface, also for simply supported conditions.

3.2.2 Membrane forces

The following development of the membrane forces has been taken from Billington's "Thin Shell Concrete Structures", which is considered one of the main references for modern day dome analysis.

According to Billington [3], shell analysis is usually divided in 4 parts:

1) Primary system based on the membrane theory
2) Errors at the boundaries due to membrane stress resultants
3) Corrections due to unite edge affects at the boundaries
4) Compatibility which is achieved by computing the size of the edge effects necessary to eliminate errors.

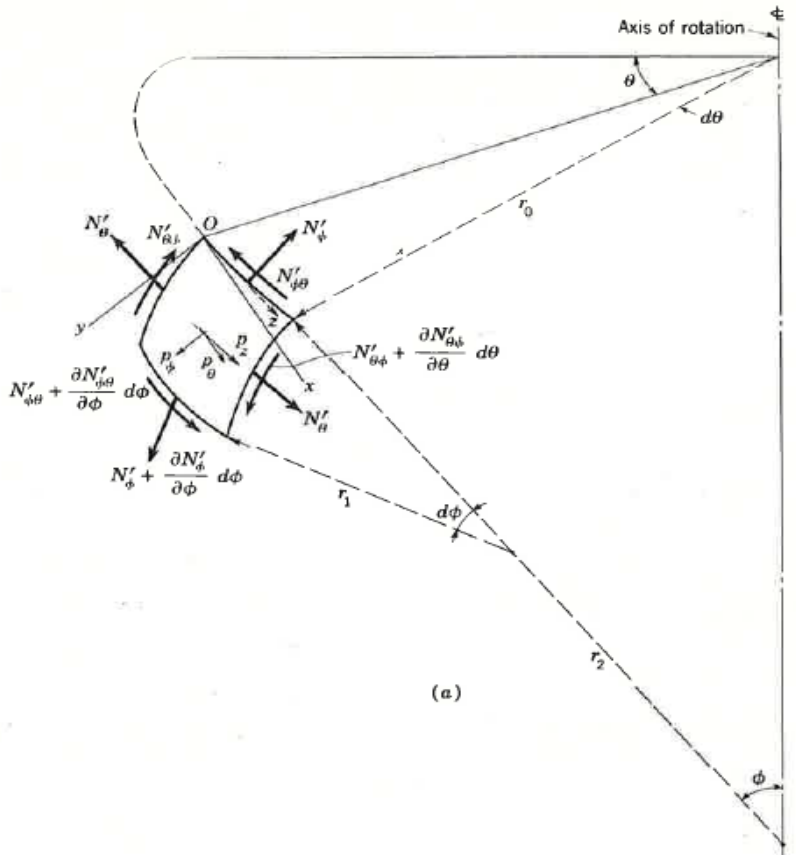

Figure 3.4. Definitions of the differential element in polar coordinates from Billington [3]

The equations that govern the stress resultants of shell systems, which are symmetrical about their axis of revolution, can be expressed in polar coordinates as follow (1):

$$\frac{dN'_{\theta}}{d\theta} r_1 + N'_{\theta\Phi} \frac{dr_0}{d\Phi} + \frac{d(N'_{\Phi\theta} r_0)}{d\Phi} + p_{\theta} r_0 r_1 = 0 \qquad \text{[Eq. 3.1]}$$

$$\frac{d(N'_{\theta} r_0)}{d\theta} - N'_{\theta} \frac{dr_0}{d\Phi} + \frac{dN'_{\theta\Phi}}{d\Phi} r_1 + p_{\Phi} r_0 r_1 = 0 \qquad \text{[Eq. 3.2]}$$

$$\frac{N'_{\theta}}{r_2} + \frac{N'_{\Phi}}{r_1} + p_z = 0 \qquad \text{[Eq. 3.3]}$$

Where:

N'_{ϕ} is the meridional stress resultants

N'_{θ} is the hoop stress resultants

$N'_{\theta\Phi}$ is the shear stress resultants

r_0 is the radius

r_1 is the principal radius of meridional curvature

r_2 is the principal radius of ration

p_{θ} is the circumferential component of the load

p_{Φ} is the meridional component of the load

p_z is the component of the load in the z direction

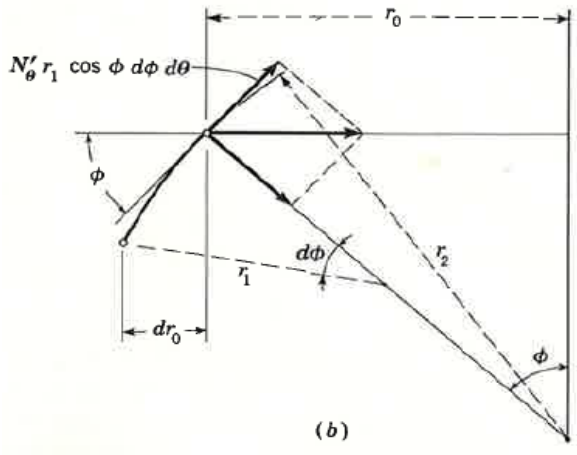

Figure 3.5. Definitions of the stress resultants in polar coordinates from Billington [3]

The loading is symmetrical with respect to the axis. Therefore, all terms involving dθ can be simplified. Additionally the terms in dϕ can be written as total differentials dϕ as nothing varies with θ. The circumferential component of load, p_θ , is null, and the shear stress resultants disappear along the meridians and parallel circles. The equations governing the stress resultants reduce to:

$$\frac{d(N'_\Phi r_0)}{d\Phi} - N'_\theta \frac{dr_0}{d\Phi} + p_\Phi r_0 r_1 = 0 \qquad \text{[Eq. 3.4]}$$

$$\frac{N'_\theta}{r_2} + \frac{N'_\Phi}{r_1} + p_z = 0 \qquad \text{[Eq. 3.5]}$$

For small values of the angle ϕ ,it is valid the following geometrical approximation:

$$\cos\Phi \sim \frac{dr_0}{r_1 d\Phi} \rightarrow \frac{dr_0}{d\Phi} = \cos\Phi \, r_1$$

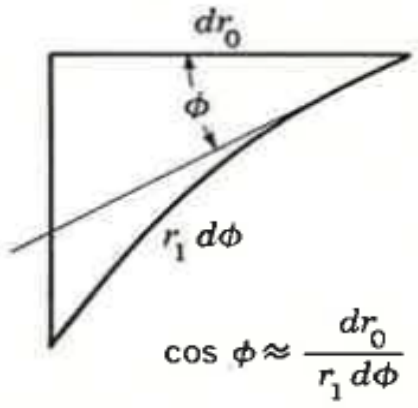

Figure 3.6. Geometrical approximation for small values of Φ [3]

which can be substituted into Eq. 3.4 to give: $\frac{d(N'_\Phi r_0)}{d\Phi} - N'_\theta \cos\Phi \, r_1 + p_\Phi r_0 r_1 = 0$

Eq. 3.5 can be solved for: $N'_\theta = -\frac{r_0}{\sin\Phi}\left(\frac{N'_\Phi}{r_1} + p_z\right)$ (*a*)

And when (*a*) is introduced into Eq. 3.4 and each term is multiplied by sinΦ, it gives

$$\sin\Phi \frac{d(N'_\Phi r_0)}{d\Phi} + \sin\Phi \frac{r_0}{\sin\Phi}\left(\frac{N'_\Phi}{r_1} + p_z\right) \cos\Phi \, r_1 + \sin\Phi \, p_\Phi r_0 r_1 = 0$$

which, when multiplied by 2π and integrated with respect to Φ, it yields

$$\int_0^{\Phi} \sin\Phi \, \frac{d(N'_{\Phi} \, r_0)}{d\Phi} \, d\Phi + \int_0^{\Phi} N'_{\Phi} r_0 \cos\Phi \, d\Phi = -\frac{1}{2\pi} \int_0^{\Phi} (\sin\Phi \, p_{\Phi} + \cos\Phi \, p_z) \, 2 \pi \, r_0 \, r_1 \, d\Phi$$

Integrating now by parts the first integral the previous expression can be simplified as:

$$N'_{\Phi} = -\frac{1}{2 \pi \, r_0 \sin\Phi} \int_0^{\Phi} (\sin\Phi \, p_{\Phi} + \cos\Phi \, p_z) \, (2 \pi \, r_0) \, r_1 \, d\Phi \qquad \text{[Eq. 3.6]}$$

The expression ($\sin\Phi \, p_{\Phi} + \cos\Phi \, p_z$) represents the vertical component of the load. $2\pi \, r_0$ instead allows to sum such vertical load over a complete parallel circle and $\int_0^{\Phi} r_1 d\Phi$ integrates the vertical load along a meridian. As a consequence the integral of Eq. 3.6 represents the total vertical load (R in Fig. 3.7) above the parallel circle defined by Φ.

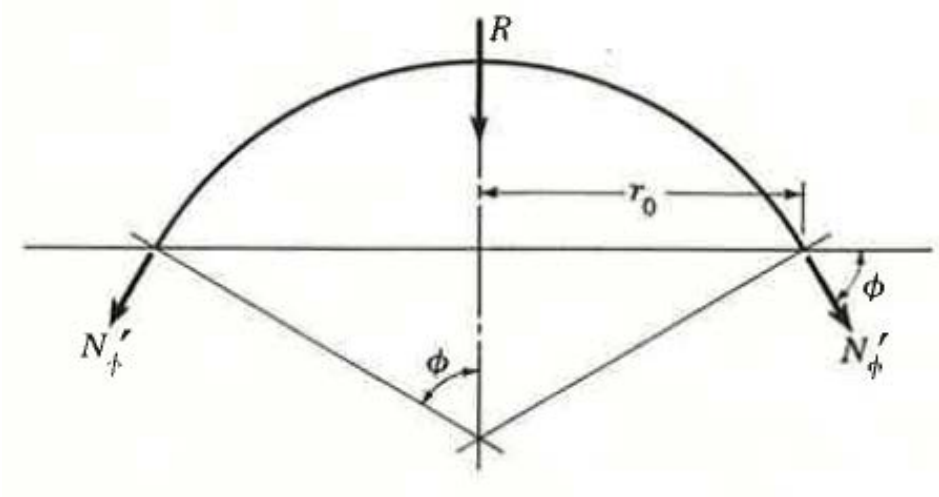

Figure 3.7. Dome equilibrium from Billington [3]

Therefore Eq. 3.6 can be rewritten as:

$$N'_{\Phi} = -\frac{R}{2 \pi \, r_0 \sin\Phi} \qquad \text{[Eq. 3.7]}$$

And substituting in (a) :

$$N'_{\theta} = \frac{R}{2 \pi \, r_1 \sin^2\Phi} - p_z \, \frac{r_0}{\sin\Phi} \qquad \text{[Eq. 3.8]}$$

Eq. 3.7 and 3.8 assume different expressions according to the specific loading condition.

3.2.3 Membrane displacements

In order to determine the membrane strains ε_ϕ and ε_θ, it has been decided to consider the following figure:

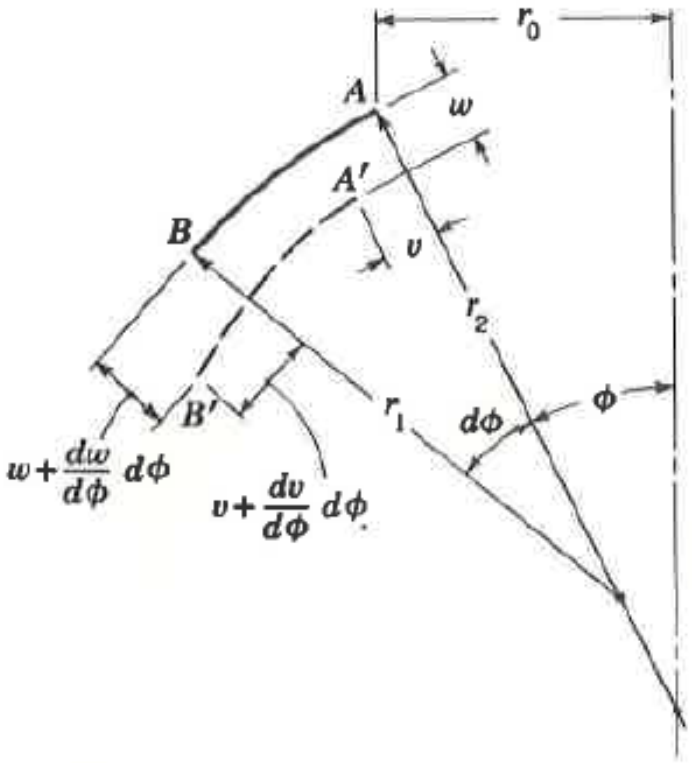

Figure 3.8. Displacements in domes from Billington [3]

The element AB and A'B' represent respectively the undeformed and the deformed configuration of the infinitesimal domes element of length $r_1 d\Phi$. The two parameters *v* and *w* instead, describe the meridional displacement and the radial displacements. The general expression of the strains can be written as follow:

$$\varepsilon = \frac{A'B' - AB}{AB} \qquad \text{[Eq. 3.9]}$$

According now to fig 3.8 the length of the deformed configuration A'B' can be expressed as: $A'B' = (r_1 - w)\, d\Phi - v + (v + dv) = (r_1 - w)\, d\Phi + dv$

therefore substituting now in Eq. 3.9 it has been possible to compute the strain in the tangent to the meridian direction:

$$\varepsilon_\phi = \frac{(r_1 - w)d\Phi + dv - r_1 d\Phi}{r_1 d\Phi} = \frac{1}{r_1}\frac{dv}{d\Phi} - \frac{w}{r_1} \qquad \text{[Eq 3.10]}$$

with similar considerations it has been computed also the strain in the hoop direction:

$$\varepsilon_\theta = \frac{r_0' \, d\theta - r_0 d\theta}{r_0 d\theta} = \frac{v}{r_0}\cos\Phi - \frac{w}{r_2} \qquad \text{[Eq 3.11]}$$

with $r'_0 = r_0 - w \sin\Phi + v \cos\Phi$

Combining now Eq. 3.10 and 3.11 and solving for v :

$$\frac{dv}{d\Phi} - \cot\Phi = r_1 \varepsilon_\phi - r_2 \varepsilon_\theta \qquad \text{[Eq 3.12]}$$

Considering now the Hooke's law it is possible to relate the strains to the membrane forces as follow:

$$\varepsilon_\phi = \frac{1}{E\,h}\left(N'_\Phi - v\, N'_\theta \right) \qquad \text{[Eq 3.13]}$$

$$\varepsilon_\theta = \frac{1}{E\,h}\left(N'_\theta - v\ N'_\Phi\right) \qquad \text{[Eq 3.14]}$$

Substituting now Eq. 3.13 and 3.14 in Eq.3.12

$$\frac{dv}{d\Phi} - v\cot\Phi = \frac{1}{E\,h}\left[N'_\Phi (r_1 + v\, r_2) - N'_\theta (r_2 + v\, r_1)\right] \qquad \text{[Eq 3.15]}$$

Eq. 3.15 can be solved by integration where:

$$f(\Phi) = \frac{dv}{d\Phi} - v\cot\Phi$$

Therefore:

$$f(\Phi) = \frac{1}{E\,h}\left[N'_\Phi (r_1 + v\, r_2) - N'_\theta (r_2 + v\, r_1)\right]$$

At this point, the general solution is:

$$v = \sin\Phi \left(\int \frac{f(\Phi)}{\sin\Phi} d\Phi + C\right) \qquad \text{[Eq 3.16]}$$

where C is the constant determined by the boundary conditions

Substituting now v in Eq. 3.11 it has been possible to determine also w:

$$w = v\cot\Phi - r_2\,\varepsilon_\theta = v\cot\Phi - \frac{r_2}{E\,h}\left(N'_\theta - \nu\ N'_\Phi\right) \qquad \text{[Eq 3.17]}$$

Eq. 3.16 and 3.17 represent the membrane deformations for general thin shells.

The meridian rotation Δ_ϕ can be obtained from Fig. 3.8 as

$$\Delta_\phi = \frac{v}{r_1} + \frac{dw}{r_1\,d\Phi} \qquad \text{[Eq 3.18]}$$

The horizontal movement Δ_H instead, can be directly derived from Eq. 3.14:

$$\Delta_H = r_0\,\varepsilon_\theta = \frac{1}{E\,h}\left(N'_\theta - \nu\ N'_\Phi\right) r_0 = \frac{r_2\,\sin\Phi}{E\,h}\left(N'_\theta - \nu\ N'_\Phi\right) \qquad \text{[Eq 3.19]}$$

Which can be thought also as: $\frac{\Delta_H}{\sin\Phi} = \frac{r_2}{E\,h}\left(N'_\theta - \nu\ N'_\Phi\right)$ [Eq 3.20]

In order to analyze the effects of the edge disturbances in shells, it is not necessary to evaluate v and w, but only the meridian rotation Δ_ϕ and the horizontal movement Δ_H at the edges. Since v is equal to 0 at the edge, Eq. 3.18 becomes:

$$\Delta_\phi = \frac{dw}{r_1\,d\Phi} = \frac{\cot\Phi}{r_1}\ \frac{dv}{d\Phi} - \frac{d}{r_1\,d\Phi}\left[\frac{r_2}{E\,h}\left(N'_\theta - \nu\ N'_\Phi\right)\right] \qquad \text{[Eq 3.21]}$$

From Eq. 3.15, with $v = 0$,

$$\frac{dv}{d\Phi} = \frac{1}{E\,h}\left[N'_\Phi\left(r_1 + \nu\,r_2\right) - N'_\theta\left(r_2 + \nu\,r_1\right)\right] \qquad \text{[Eq 3.22]}$$

Substituting now Eq. 3.22 and 3.20 in Eq. 3.21, we get

$$\Delta_\phi = \frac{\cot\Phi}{r_1 E\,h}\ \left[N'_\Phi\left(r_1 + \nu\,r_2\right) - N'_\theta\left(r_2 + \nu\,r_1\right)\right] - \frac{d}{r_1\,d\Phi}\left[\frac{\Delta_H}{\sin\Phi}\right] \qquad \text{[Eq 3.23]}$$

3.2.4 Failure Criterion

Since the constitutive shell materials in this study are assumed brittle, the adopted failure criterion is Coulomb-Mohr which is based on the Mohr's circle. According to this criterion, the failure of the material occurs when in any point of a structure stresses

exceed the envelope generated by the two Mohr's circles for uniaxial compression strength and uniaxial tensile strength.

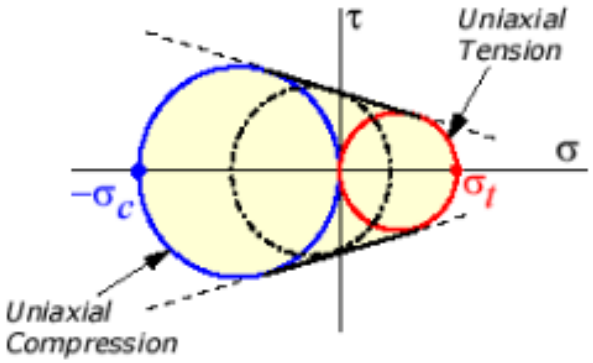

Figure 3.9. Circles of Mohr [34]

As Fig. 3.9 illustrates, the right circle represents the uniaxial tension at the limiting tension stress σ_t, whereas the left circle represents the uniaxial compression at the limiting compression stress σ_t. The one in the middle instead represents the maximum allowable stress for an intermediate stress state. Each possible intermediate state is summarized in Table 3.1.

Table 3.1. Criterion requirement for intermediate states [34]

Case	Principal Stresses		Criterion requirements
1	Both in tension	$\sigma_1 > 0, \sigma_2 > 0$	$\sigma_1 < \sigma_t, \sigma_2 < \sigma_t$
2	Both in compression	$\sigma_1 < 0, \sigma_2 < 0$	$\sigma_1 > -\sigma_c, \sigma_2 > -\sigma_c$
3	σ_1 in tension, σ_2 in compression	$\sigma_1 > 0, \sigma_2 < 0$	$\frac{\sigma_1}{\sigma_t} + \frac{\sigma_2}{-\sigma_c} < 1$
4	σ_1 in compression, σ_2 in tension	$\sigma_1 < 0, \sigma_2 > 0$	$\frac{\sigma_1}{-\sigma_c} + \frac{\sigma_2}{\sigma_t} < 1$

3.2.5 Spherical domes

Uniform load over the dome surface (self-weight)

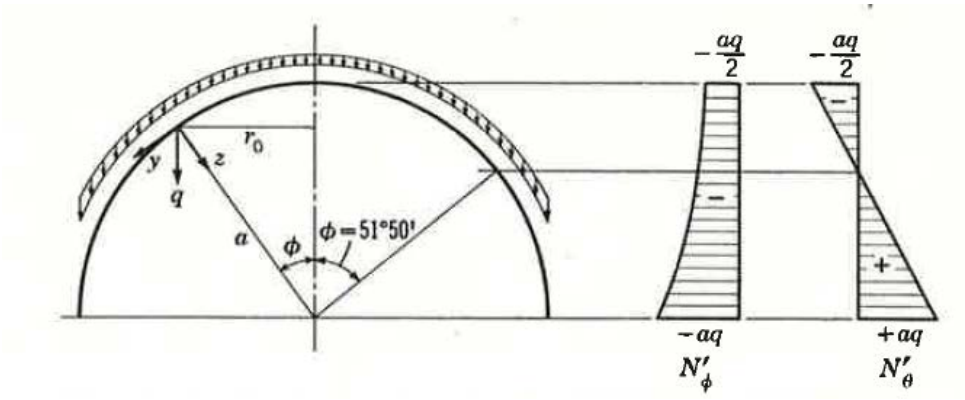

Figure 3.10. Hemispherical dome under uniform load over the dome surface from Billington [3]

A hemispherical dome of uniform thickness subjected to its own weight is described by:

$r_1 = r_2 = a$ $\qquad p_\phi = q \sin\Phi$ $\qquad p_z = q \cos\Phi$

$R = 2 \pi a^2 q \int_0^\Phi \sin\Phi \, d\Phi = 2 \pi a^2 q (1 - \cos\Phi)$

where q is the dead weight of the shell. In this case, Eq. 3.7 and 3.8 become:

$$N'_\Phi = - aq \frac{1}{1 + \cos\Phi} \qquad \text{[Eq 3.24]}$$

$$N'_\theta = aq \left(\frac{1}{1 + \cos\Phi} - \cos\Phi \right) \qquad \text{[Eq 3.25]}$$

The meriodional stresses increase from the crown to the edge and are in pure compression. Hoop stresses decreases from a maximum value of compression at the crown to zero where $\cos\Phi = \frac{1}{1 + \cos\Phi}$, which corresponds to approximately 51°50'; Hoop stresses then become tension reaching their maximum value at the edge. Substituting now Eq.3.24 and 3.25 in Eq. 3.21 and 3.23, Δ_ϕ and Δ_H assume the following expressions :

$$\Delta_H = \frac{q a^2}{E h} \left(\frac{1 + \nu}{1 + \cos\Phi} - \cos\Phi \right) \sin\Phi \qquad \text{[Eq 3.26]}$$

$$\Delta_\phi = - \frac{a q}{E h} (2 + \nu) \sin\Phi \qquad \text{[Eq 3.27]}$$

Uniform load over a horizontal projection of the dome surface

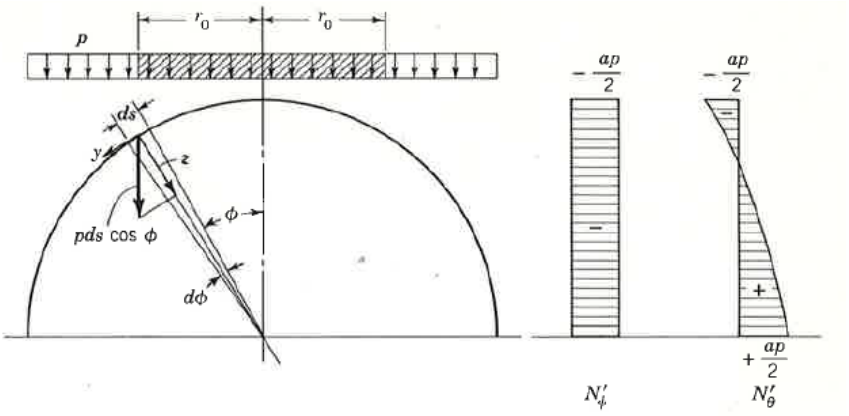

Figure 3.11. Hemispherical dome under uniform load over

an horizontal projection of the dome surface [3]

When the hemispherical dome is subjected to a uniform load over the horizontal projection of the dome surface, the load is given by:

$p_z = p \cos^2\Phi$ $\quad p_\Phi = p \sin\Phi \cos\Phi$ $\quad p_\theta = 0$

$R = 2 \pi r_0^2 = p a^2 \pi \sin^2 \Phi$

In this case, Eq. 3.7 and 3.8 become:

$$N'_\Phi = -\frac{a p}{2} \qquad \text{[Eq 3.28]}$$

$$N'_\theta = -\frac{a p}{2} \cos(2\Phi) \qquad \text{[Eq 3.29]}$$

Therefore N'_Φ is a constant compression, whereas N'_θ varies from compression at the crown to tension at the edge. Zero hoop value occurs where $\cos2\Phi = 0$ or $\Phi = 45°$. Substituting now Eq.3.28 and 3.29 in Eq. 3.21 and 3.23, Δ_ϕ and Δ_H assume the following expressions for this load case:

$$\Delta_H = \frac{a^2 p}{2 E h} [-\cos(2\Phi) + \nu] \sin\Phi \qquad \text{[Eq 3.30]}$$

$$\Delta_\phi = \frac{a q}{2 E h} (3 + \nu) \sin(2\Phi) \qquad \text{[Eq 3.31]}$$

Uniform external pressure over the dome surface

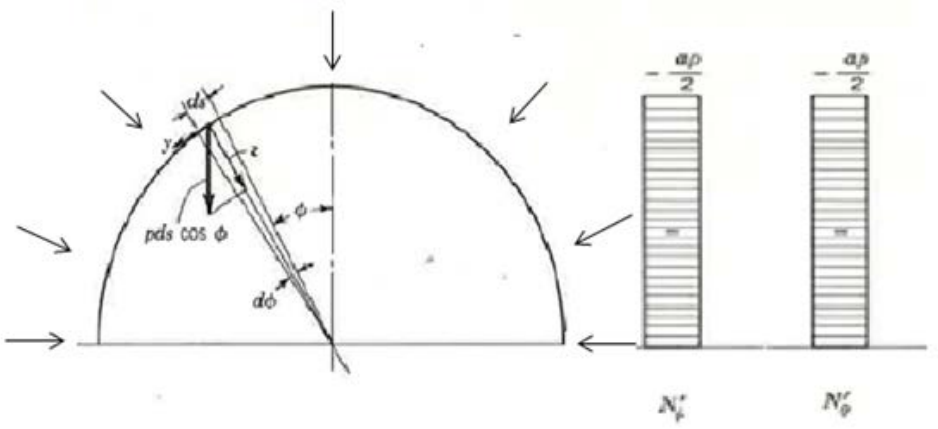

Figure 3.12. Hemispherical dome under uniform external pressure

When the hemispherical dome is subjected to uniform pressure p over the dome surface, the load can be described only by its vertical component to the surface of the dome:

$p_z = p$ $\qquad p_\Phi = 0$ $\qquad p_\theta = 0$

$$R = \frac{\pi\, a^2\, p}{2}\ (2 \sin^2 \Phi)_0^\Phi$$

In this case, Eq. 3.7 and 3.8 become:

$$N'_\Phi = -\frac{\pi\, a^2\, p \sin^2\Phi}{2\, a \sin^2\Phi} = -\frac{a\, p}{2} \qquad \text{[Eq 3.32]}$$

$$N'_\theta = -\,a\,(p - \frac{a\, p}{2a}) = -\frac{a\, p}{2} \qquad \text{[Eq 3.33]}$$

Substituting now Eq.3.28 and 3.29 in Eq. 3.21 and 3.23, Δ_ϕ and Δ_H assume the following expressions for this load case:

$$\Delta_H = \frac{a^2 p}{2\, E\, h}\,(-1 + \nu)\,\sin\Phi \qquad \text{[Eq 3.30]}$$

$$\Delta_\phi = 0 \qquad \text{[Eq 3.31]}$$

3.2.6 Elliptical domes

The general expression of an elliptical arch is given by:

$$\frac{x^2}{a^2} + \frac{y^2}{b^2} = 1 \qquad \text{[Eq 3.32]}$$

where a and b represent respectively the major and minor axis, instead x corresponds to r_0, the radius of the parallel circle; so

$$x = r_0 = a\sqrt{1 - \frac{y^2}{b^2}} = \frac{a}{b}\sqrt{b^2 - y^2} \qquad \text{[Eq 3.33]}$$

$$\frac{dy}{dx} = \frac{1}{dx/dy} = -\tan\Phi = -\frac{b}{ay}\sqrt{b^2 - y^2} \qquad \text{[Eq 3.34]}$$

For an elliptical geometry $\sin\Phi$ and $\cos\Phi$ can be expressed as:

$$\sin\Phi = \frac{dy}{ds} = \frac{dy}{\sqrt{dy^2 + dx^2}} = \frac{dx/dy}{\sqrt{(dy/dx)^2 + 1}} = \frac{-\tan\phi}{\sqrt{\tan\phi^2 + 1}} = \frac{-b\sqrt{b^2 - y^2}}{\sqrt{b^4 + y^2(a^2 - b^2)}} \qquad \text{[Eq 3.35]}$$

$$\cos\Phi = \frac{1}{\sqrt{\tan\phi^2 + 1}} = \frac{a\,y}{\sqrt{b^4 + y^2(a^2 - b^2)}} \qquad \text{[Eq 3.36]}$$

The two principal radii of curvature are thus given by the expressions:

$$r_1 = \frac{[b^4 + y^2(a^2 - b^2)]^{3/2}}{a\,b^4} \qquad \text{[Eq 3.37]}$$

$$r_2 = \frac{a}{b^2}\sqrt{b^4 + y^2(a^2 - b^2)} \qquad \text{[Eq 3.38]}$$

The coordinates at the crown of the dome are: y = b and $r_1 = r_2 = \frac{a}{b^2}$,

while the coordinates at the base of the dome are: y = 0, $r_1 = \frac{b^2}{a}$, $r_2 = a$.

Uniform load over the dome surface

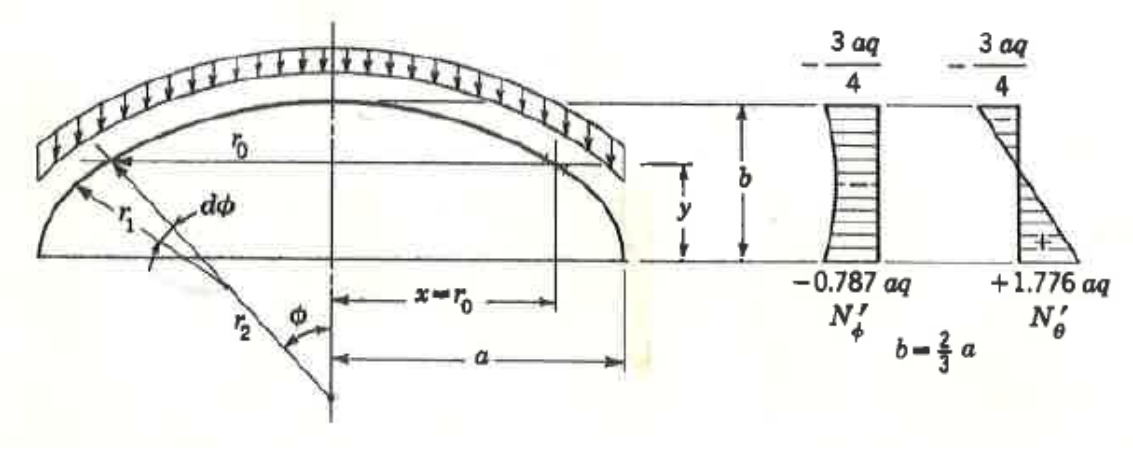

Figure 3.13. Distribution of the two membrane stress resultants over the ellipsoid [3]

When a spherical dome of uniform thickness is subjected to its own weight,

$p_z = q \cos\Phi$ $p_\phi = q \sin\Phi$ $p_\theta = 0$

$$R = 2\pi q \int_y^b x\, ds \qquad \text{[Eq 3.39]}$$

According to Eq. 3.33:

$$x = r_0 = a\sqrt{1 - \frac{y^2}{b^2}} = \frac{a}{b}\sqrt{b^2 - y^2}$$

and considering: $ds = dy\sqrt{1 + (\frac{dx}{dy})^2}$

Inverting Eq. 3.28: $\frac{dx}{dy} = -\frac{a\,y}{b\sqrt{b^2 - y^2}}$

and substituting it in the previous one:

$$ds = dy\sqrt{1 + \frac{a^2 b^2}{b^2(b^2 - y^2)}} \qquad \text{[Eq 3.40]}$$

Substituting now Eq. 3.27 and 3.34 in Eq. 3.33:

$$R = 2\pi q \int_y^b \left[\frac{a}{b}\sqrt{b^2 - y^2}\sqrt{1 + \frac{b^2(b^2 - y^2) + a^2 y^2}{b^2(b^2 - y^2)}}\, dy\right]$$

$$R = 2\pi q \frac{a}{b^2}\int_y^b \sqrt{b^4 + y^2(a^2 - b^2)}\, dy$$

$$R = 2\pi a^2 q \left[\frac{1}{2} - \frac{y}{2ab^2}\sqrt{b^4 + y^2(a^2 - b^2)} \right.$$

$$\left. + \frac{b^2}{2a\sqrt{a^2-b^2}} \log \frac{b\,(a + \sqrt{b^2-y^2})}{y\sqrt{a^2-b^2} + \sqrt{b^4 + y^2(a^2-b^2)}} \right] \qquad \text{[Eq 3.41]}$$

The quantity in the bracket varies according to the ratios y/b and b/a and it has been listed in Table 3.1 as a quantity C (1). Therefore Eq.3.41 can be rewritten as :

$$R = 2\pi a^2 q C \qquad \text{[Eq 3.42]}$$

In this case the membrane forces become:

$$N'_{\Phi} = -\frac{R}{2\pi r_0 \sin\Phi} = -\frac{2\pi a^2 q C}{2\pi r_2 \sin^2\Phi} = -\frac{a^2 q C b^2}{a \sin^2\phi\sqrt{b^4 + y^2(a^2-b^2)}}$$

Substituting now Eq. 3.29 in the previous one:

$$N'_{\Phi} = -\frac{a^2 q C b^2 [b^4 + y^2(a^2-b^2)]}{b^2(b^2-y^2)\, a\sqrt{b^4 + y^2(a^2-b^2)}} = -\frac{a^2 q}{b} \frac{C}{(b^2-y^2)/b^2} \frac{\sqrt{b^4 + y^2(a^2-b^2)}}{ab}$$

Calling now: $Q = \frac{\sqrt{b^4 + y^2(a^2-b^2)}}{ab}$

Since the parameter Q varies according to the ratio y/b and b/a , therefore it is listed in Table 3.1 as well. In conclusion, Eq. 3.7 and 3.8 can be rewritten in this case as:

$$N'_{\Phi} = -\frac{a^2 q}{b} \frac{C\,Q}{1 - (y^2/b^2)} \qquad \text{[Eq 3.43]}$$

$$N'_{\theta} = -r_2 \left(p_z + \frac{N'\Phi}{r_1} \right) = -r_2\, q \cos\Phi - \frac{N'\Phi}{r_1} r_2 \qquad \text{[Eq. 3.44]}$$

Table 3-1 COEFFICIENTS FOR ELLIPTICAL DOMES

$g = y/b$	Values of C*									Values of Q†									$g = y/b$
	b/a									b/a									
	0.2	0.3	0.4	0.5	0.6	0.7	0.8	0.9	1.0	0.2	0.3	0.4	0.5	0.6	0.7	0.8	0.9	1.0	
0.0	0.547	0.588	0.636	0.690	0.747	0.807	0.870	0.934	1.000	0.200	0.300	0.400	0.500	0.600	0.700	0.800	0.900	1.000	0.0
0.1	0.526	0.558	0.596	0.640	0.687	0.737	0.789	0.844	0.900	0.227	0.315	0.410	0.507	0.605	0.704	0.802	0.901	1.000	0.1
0.2	0.501	0.525	0.554	0.588	0.626	0.666	0.709	0.754	0.800	0.280	0.356	0.440	0.529	0.621	0.714	0.809	0.904	1.000	0.2
0.3	0.469	0.486	0.508	0.534	0.563	0.594	0.627	0.663	0.700	0.356	0.415	0.485	0.563	0.646	0.732	0.820	0.909	1.000	0.3
0.4	0.430	0.441	0.456	0.475	0.496	0.520	0.545	0.572	0.600	0.440	0.485	0.543	0.608	0.680	0.756	0.835	0.917	1.000	0.4
0.5	0.381	0.389	0.399	0.412	0.427	0.443	0.461	0.480	0.500	0.529	0.563	0.608	0.661	0.721	0.786	0.854	0.926	1.000	0.5
0.6	0.323	0.328	0.335	0.343	0.352	0.362	0.374	0.387	0.400	0.621	0.646	0.680	0.721	0.768	0.821	0.877	0.937	1.000	0.6
0.7	0.257	0.260	0.263	0.267	0.272	0.278	0.285	0.292	0.300	0.714	0.732	0.756	0.786	0.821	0.860	0.904	0.950	1.000	0.7
0.8	0.181	0.182	0.183	0.185	0.188	0.190	0.193	0.196	0.200	0.809	0.820	0.835	0.854	0.877	0.903	0.933	0.965	1.000	0.8
0.9	0.095	0.095	0.096	0.096	0.097	0.098	0.098	0.099	0.100	0.904	0.910	0.917	0.926	0.937	0.950	0.965	0.982	1.000	0.9
1.0	0.000	0.000	0.000	0.000	0.000	0.000	0.000	0.000	0.000	1.000	1.000	1.000	1.000	1.000	1.000	1.000	1.000	1.000	1.0

*$C = \frac{1}{2} + \frac{1-k^2}{2k}\log(1+k) - \frac{g}{2}\sqrt{1-k^2(1-g^2)} - \frac{1-k^2}{2k}\log\left[gk + \sqrt{1-k^2(1-g^2)}\right]$, in which $k^2 = 1 - \frac{b^2}{a^2}$.

†$Q = \sqrt{1-k^2(1-g^2)}$.

Table 3.2. Coefficients for elliptical domes from Billington [3]

3.3 Numerical method: Finite Element Method with Abaqus

3.3.1 Introduction to Finite Element Analysis

The finite element method can be defined as a numerical method for finding approximate solutions to boundary value problems for partial differential equations [35]. The main concept behind this method is to subdivide a large problem into smaller, simpler parts (called finite elements) and to interconnect them through the points (called nodes) or/and the edges or/and the surfaces that they have in common. This process is commonly named “Discretization”. Through this process, it is possible to formulate an equation for each finite element and after to combine to obtain a solution of the domain. The finite element method has become very popular especially when, due to the complexity of the problem, an analytical solution is difficult to achieve. In fact, numerical methods provide approximate solutions of the unknowns (called degrees of freedom) with a reasonable loss of accuracy. Structural analysis, fluid dynamic, distribution of electromagnetic potential, heat transfer represent some examples of problems where the finite element method has been successfully applied. In structural analysis which involves structures subjected to applied loads, displacements and stresses are usually the unknowns of the problem. For nonstructural analysis, the unknown values may be fluid pressures, electromagnetic potential or temperature, etc.

3.3.2 Steps of the Finite Element Method

According to Logan’s “A first Course in the Finite Element Method” [35], the main steps of the finite element method can be synthetized as follow:

- **Step 1**: *Discretize and select the element types*. Step 1 involves the subdivision of the body in a set of finite elements interconnected by nodes and the selection of the element type that best models the real physical behavior of the body. The dimensions of such elements have to be wisely decided so that they reach an adequate accuracy of the solution and on the other hand to reduce computational time and effort. For relative constant problems, large elements can be used. However, when the properties of the body change rapidly, the use of smaller elements becomes necessary. Also the choice of the type of elements has an influence on the accuracy of the result, therefore it has to be established according to the geometry of the body and the type of loading conditions. The most common type of elements are shown in the figures below:

Figure 3.14. Simple line element typically used to represent a bar or a beam element [35]

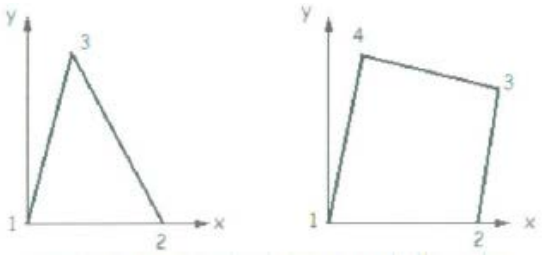

Figure 3.15. Simple 2-dimensional elements used to represent plan stress/strain [35]

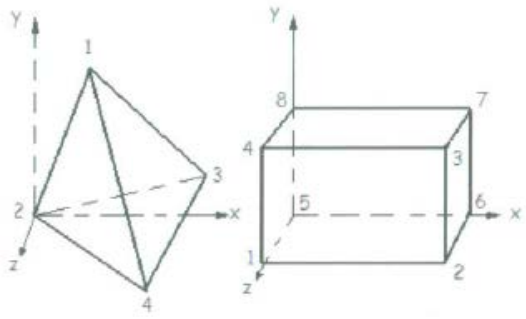

Figure 3.16. Simple 3-dimensional elements used to represent 3-dimensional stress [35]

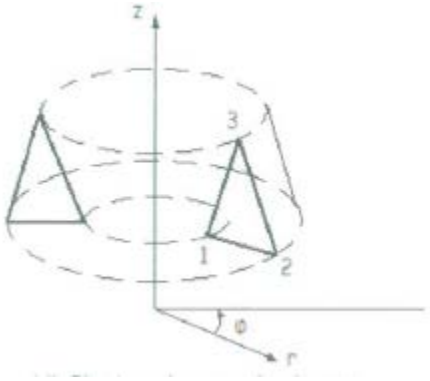

Figure 3.17. Simple axisymmetric element [35]

- **Step 2**: *Select a displacement function.* Step 2 involves the choice of a displacement function which is defined within the element using the nodal values of the element. In general, the finite element process works really well with linear, quadratic and cubic polynomials, because of the simplicity of their formulation. However, also other functions can also be employed, such as trigonometric series. Once the displacement function has been selected, it can be used repeatedly for each element. Through this process, any continuous function of interest can be approximated by a series of piecewise-continuous functions defined within each finite domain or finite element.

- **Step 3**: *Define the Strain/Displacement and Stress/Strain relationship***.** Step 3 involves the definition of Strain/Displacement and Stress/Strain relationships to derive the equations for each finite element. In the simplest case of one-dimensional deformation, the strain ε_x in the x direction, related to the displacement u, is defined as: $\varepsilon_x = \frac{du}{dx}$ for small strains. Furthrmore, the strain must be related to the stress through a constitutive law. The most common and simplest constitutive law is the Hooke's law, which in one dimensional case is expressed as: $\sigma_x = E\ \varepsilon_x$ where E represents the modulus of elasticity and σ_x the stress in the x direction.

- **Step 4**: *Derive the element stiffness matrix and equations.* Step 4 involves the use of the direct equilibrium/stiffness method or the work/energy method or the weighted residuals method.

Direct equilibrium or stiffness method

This method is based on force equilibrium conditions for a single element. The stiffness matrix element equations that relate the nodal forces to the displacement are provided using force/deformation relationship [35].

Work or energy method

The work or energy method represents the best solution when it is necessary to develop the stiffness matrix and equations for two- and three-dimensional elements. The principle of virtual work, the principle of minimum potential energy and Castigliano's theorem are the most popular methods for this kind of purpose. The first one is applicable for any kind of materials, whereas the other two only to elastic materials.

Method of weighted residuals

When a function such as potential energy is not readily available, the method of weighted residuals becomes particularly useful. The most famous one is the Galerkin's method. This method provides the same results of the energy methods, wherever the energy methods are applicable. In addition, it can also be directly applied to any kind of differential equations by using them.

The purpose of any of the aforementioned methods is to provide the equations to describe the behavior of each element. These equations can be conveniently written in a compact form as: $\{ f \} = [k] \{ d \}$

where $\{ f \}$ is the vector of nodal element forces, $[k]$ is the element stiffness matrix and $\{ d \}$ is the vector of the degrees of freedom or generalized displacements.

- **Step 5** : *Assemble the equations to obtain the global or total equations and introduce boundary conditions.* Step 5 focuses on the assembly of the individual element nodal equilibrium equations into the global nodal equilibrium equations. In order to obtain the global equations it is also possible to use a more direct method, commonly named as "*direct stiffness method*". Such method implicitly assumes that the structure remains together (no tears occur anywhere within the structure). The assembled or global equation can be written in the matrix form: $\{ \mathbf{F} \} = [\mathbf{K}] \{ d \}$

  where $\{ \mathbf{F} \}$ is the vector of global nodal forces, $[\mathbf{K}]$ is the structure global or total stiffness matrix, and $\{ d \}$ is the vector of known and unknown degrees of freedom or generalized displacements. At this stage, it is also important to choose the

appropriate boundary conditions in order to avoid rigid body motion from the structure.

- **Step 6**: *Solve for the unknown degrees of freedom*. Step 6 involves the resolution of the unknown degrees of freedom through the set of the algebraic equations that can be written in the following matrix form as:

$$\begin{Bmatrix} F_1 \\ F_2 \\ \vdots \\ F_n \end{Bmatrix} = \begin{bmatrix} K_{11} & K_{12} & \dots & K_{1n} \\ K_{21} & K_{22} & \dots & K_{2n} \\ \vdots & & & \vdots \\ K_{n1} & K_{n2} & \dots & K_{nn} \end{bmatrix} \begin{Bmatrix} d_1 \\ d_2 \\ \vdots \\ d_n \end{Bmatrix}$$

where now *n* is the structure total number of unknown nodal degrees of freedom.

- **Step 7**: *Solve for element strains and stresses.* Step 7 involves the resolution of stress and strain quantities thanks to the relations and the constitutive laws pre-defined in step 3.
- **Step 8**: *Interpret the results*. Step 8 involves the interpretation of the results and requires critical thinking. The main goal is to determine the locations where the structure experiences large stresses or deformations because, in order to improve the designing process. Postprocessor computer software helps the understanding of the user by showing the results in various graphical forms.

3.3.3 Abaqus: Pre-processing, Analysis, Post-processing

The finite element software Abaqus has been chosen to compute the analysis of shells in this research. Abaqus has been released in 1978 and it is very suitable for finite element analysis and computer-aided engineering. A Student edition has been used for this study.

The modeling process of any finite element software can be usually divided in three main stapes: pre-processing, analysis and post-processing. A general description of these steps is shown here below.

- **Step 1:** *Pre-processing.* This step is responsible of the general construction of the model. Since the analyzed problems are always axisymmetrical, each shell has been created in Abaqus by rotating around the y-axis at x=0 half of the geometry of interest. This has been done in Section “Part” selecting the following: -
  - Modeling Space: 3D
  - Type: Deformable
  - Shape: Shell
  - Base feature type: Revolution

Afterwards, it is necessary to define the material properties. Since this research is focused on linear elastic material, it has been sufficient to define the “Density”, the “Modulus of elasticity” and the “Poisson’s ratio” of the material in section “Property”. The selected “Category” and “Type” of section for each shell were decided to be “Solid” and “Homogeneous”, respectively. Then, in section “Assembly” it has been chosen “Independent (mesh on instance)” as an “Instance Type”. The two type of analysis involved in this paper are “Static, General” and “Linear perturbation, Buckle” and they can be set up in section “Step”. After the definition of the load and the boundary conditions, the creation of an appropriate mesh is required. The chosen “ Element shape” has been “Quad” for each shell. Although the student version is restricted to 1000 elements in total, staying under this threshold provided a satisfactory level of accuracy for the scope of this study. Finally, when all the inputs are determined, the next step is to

run the model. This requires the creation of a “Job” which can be done in section “Job Manager”.

- **Step 2**: *Analysis.* In this step the validity of the model is tested. A dat. file containing the global stiffness matrix and other important information are created when running the model. If some input parameters are missing, the software stops the analysis giving back an error as an output.
- **Step 3**: *Post-processing.* This step involves the evaluation and the discussion of the results. Abaqus shows them in several ways, ranging from illustrations, graphs to tables. Thanks to this step, it is also possible to compare the numerical solution obtained from the software with the analytical one.

3.4 Comparison

3.4.1 Assumptions

The aim of this section is to compare analytical and numerical solutions in order to confirm the validity of the models created with the finite element software. In this study, different geometries and different load cases have been considered, while a constant thickness along the dome surface is assumed. The results of the membrane theory are valid for simply supported conditions. Moreover, all dome configurations examined are simply supported in accordance with the membrane theory. However, in order to run the analysis in the finite element software, it is necessary to avoid rigid body motions. Therefore the finite structure needs to have at least one point of the boundary conditions restrained against translation in each direction generating edge disturbances which affects the symmetry of the stress distribution. Nevertheless, the edge disturbances tend to damp rapidly allowing at a sufficient distance from the pinned points the stress distribution to

reflect the correct one. The material employed in this comparison is based on mycelium with the properties already stated in Table 2.1.

3.4.2 Influence of the type of loading

This section involves a comparison between the analytical and the numerical solution for a hemispherical dome (angle of cut $\phi = 90°$) with a radius a = 5m and a thickness t = 0.1m subjected to the following load cases:

- Case 1: Uniform load over the dome surface: p = self-weight
- Case 2: Uniform load over a horizontal projection of the dome surface: p= 500 Pa
- Case 3: Uniform external pressure over the dome surface: p = 1000 Pa

Case 1: Uniform load over the Dome surface: p = self-weight

As it has been already shown, the analytical solution for a hemispherical dome subjected to its own weight can be computed according to Eq. 3.24 and 3.25:

$$N'_{\Phi} = -aq\frac{1}{1+\cos\Phi} \quad \text{[Eq 3.24]}$$

$$N'_{\theta} = aq\left(\frac{1}{1+\cos\Phi} - \cos\Phi\right) \quad \text{[Eq 3.25]}$$

The only missing parameter is q, which represents the pressure that the weight exerts per unit m^2 of dome surface and it can be computed with the following procedure:

Volume of the dome : $V = \frac{1}{2}(Vol_{sphere\_full} - Vol_{sphere\_empty})$

$V = \frac{1}{2}\left[\frac{4}{3}\pi a^3 - \frac{4}{3}\pi (a - t)^3\right] = \frac{1}{2}\cdot\left[\frac{4}{3}\pi 5^3 - \frac{4}{3}\pi (5 - 0.1)^3\right] = 15.4\ m^3$

Weight of the dome: $W = V\,\delta\,g = 15.4 \cdot 130 \cdot 9.81 = 19639.6\ N$

Where:

δ is the density of the material

g is the gravity acceleration

Surface of the hemisphere: $S = \frac{1}{2} S_{sphere} = \frac{1}{2} \cdot 4 \pi a^2 = 2 \cdot \pi \cdot 5^2 = 157.1 \text{ m}^2$

Pressure on dome surface: $q = \frac{W}{S} = -\frac{19639.6}{157.1} = 125 \text{ Pa}$

Since the maximum values of the stresses occur at the edge ($\phi = 90°$), according to Eq. 3.24 and 3.25:

Meridional force: $N'_{\Phi} = -aq \frac{1}{1+\cos\Phi} = -5 \cdot (125) \cdot \frac{1}{1+\cos(90°)} = -625 \text{ N/m}$

Hoop force: $N'_{\theta} = aq\left(\frac{1}{1+\cos\Phi} - \cos\Phi\right) = 5 \cdot (125) \cdot \left(\frac{1}{1+\cos(90°)} - \cos(90°)\right) = 625 \text{N/m}$

Dividing now by the thickness t of the dome , we obtained the following internal stress :

Meridional stress: $\sigma_{\Phi} = \frac{N'_{\Phi}}{t} = \frac{625}{0.1} = -6250 \text{ Pa}$

Hoop stress: $\sigma_{\theta} = \frac{N'_{\theta}}{t} = -\frac{625}{0.1} = 6250 \text{ Pa}$

Since the edge is subjected both to tension and compression, according to the Mohr's failure criterion: $\left|\frac{\sigma_{\Phi}}{\sigma_c}\right| + \left|\frac{\sigma_{\theta}}{\sigma_t}\right| < 1 \rightarrow \left|\frac{-6250}{-55000}\right| + \left|\frac{6250}{17000}\right| = 0.48 < 1$

Therefore, the hemispherical dome can be considered safe. The numerical results obtained with the Abaqus model are shown in Fig.3.18 and 3.19:

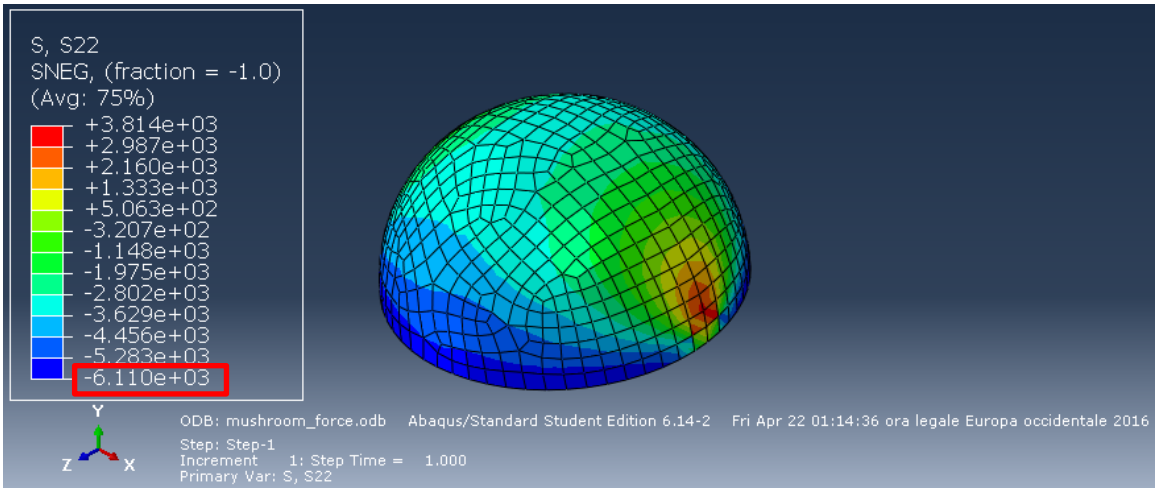

Figure 3.18. Illustration of the meridional stresses

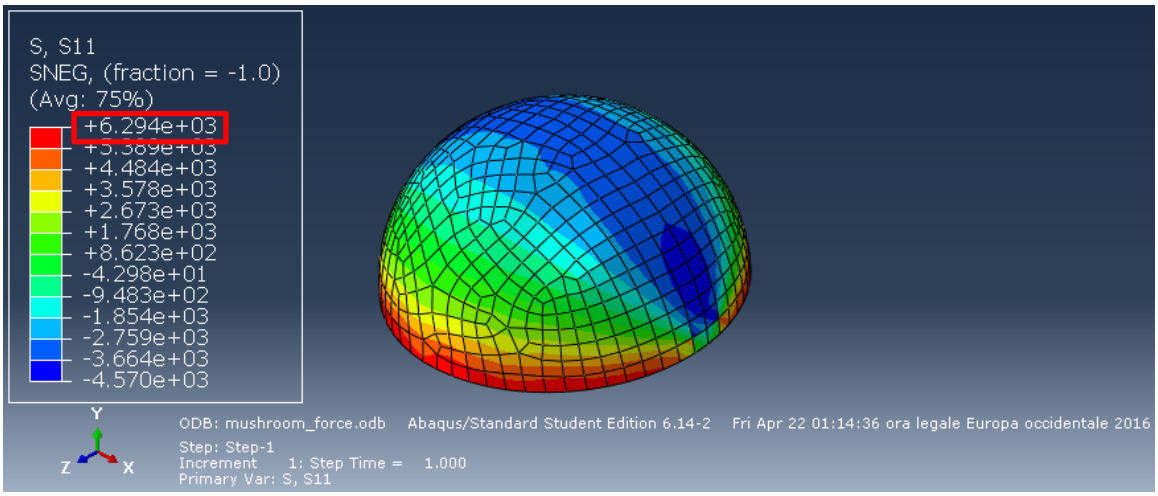

Figure 3.19. Illustration of the hoop stresses

As it can be seen in the Table 3.3 the numerical solution is close to the analytical solution, therefore the numerical model is considered valid. An even greater level of accuracy it can be reached by increasing the refinement of the mesh, which in our case was limited by the student version of the software.

Table 3.3. Stress generated by a uniform load over the dome surface (self-weight)

CASE 1	UNIFORM LOAD OVER THE DOME SURFACE		
	σ_Φ (Pa)	σ_θ (Pa)	**Mohr's Criterion**
Analytical Solution	-6250	6250	0.48
Numerical Solution	-6110	6294	0.47

Therefore it can be affirmed that, according to the linear analysis, the material strength is higher than the stresses sustained by the structure when it is subjected to its own weight. Although Fig. 3.18 and 3.19 show stress distributions that are not symmetric, if an arch at a sufficient distance from the pinned points is considered and the meridional and the hoop stresses are plotted separately, the obtained results are in accordance with the theory. The meridional and the hoop stress distribution are shown in Fig. 3.20 and 3.21 respectively.

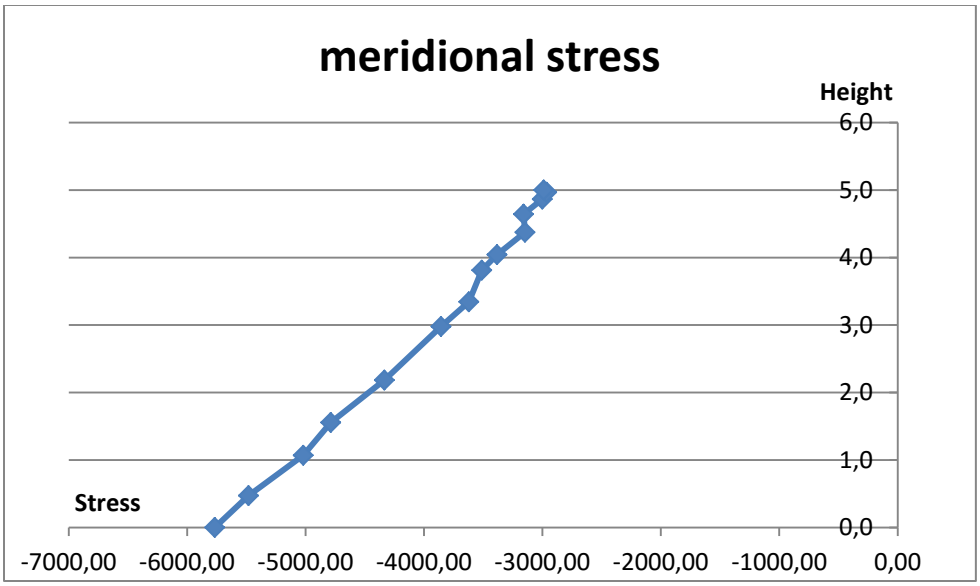

Figure 3.20. Meridional stress vs height plot

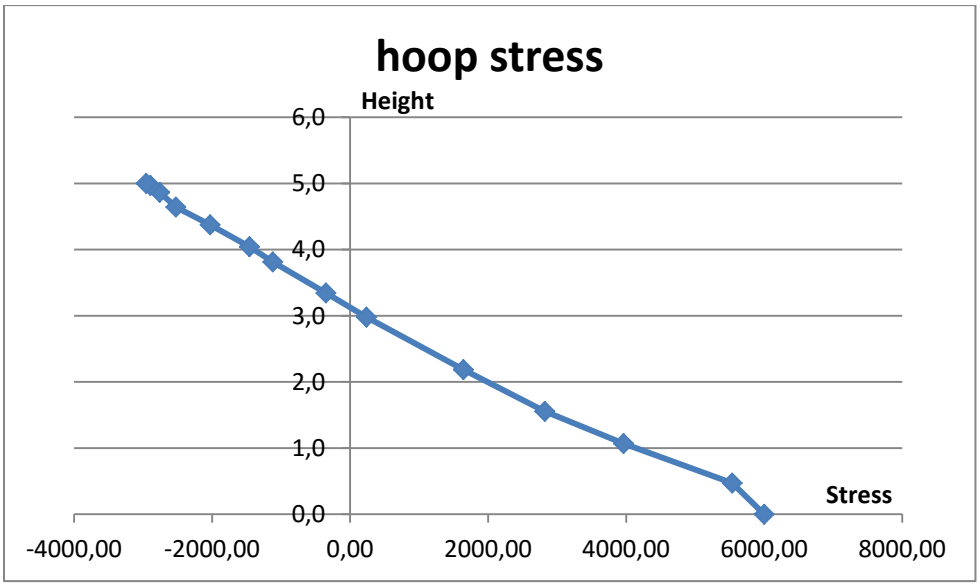

Figure 3.21. Hoop stress vs height plot

Case 2: Uniform load over a Horizontal Projection of the Dome Surface: p = 500 Pa

As it has been already shown, the analytical solution for an hemispherical dome subjected to a uniform load over a horizontal projection of the dome surface can be computed according to Eq. 3.28 and 3.29:

$$N'_{\Phi} = -\frac{a\,p}{2} \qquad \text{[Eq 3.28]}$$

$$N'_{\theta} = -\frac{a\,p}{2}\cos(2\Phi) \qquad \text{[Eq 3.29]}$$

Since the maximum values of the stresses occur at the edge ($\phi = 90°$):

Meridional force: $N'_{\Phi} = -\frac{a\,p}{2} = -\frac{5 \cdot (500)}{2} = -1250$ N/m

Hoop force: $N'_{\theta} = -\frac{a\,p}{2}\cos 2\Phi = -\frac{5 \cdot (500)}{2}\cos(2 \cdot 90°) = 1250$ N/m

Dividing now by the thickness t of the dome, we obtained the following internal stresses :

Meridional stress: $\sigma_{\Phi} = \frac{N'_{\Phi}}{t} = \frac{-1250}{0.1} = -12500$ Pa

Hoop stress: $\sigma_{\theta} = \frac{N'_{\theta}}{t} = \frac{1250}{0.1} = 12500$ Pa

Since the edge is subjected both to tension and compression, according to the Mohr's failure criterion: $\left|\frac{\sigma_{\Phi}}{\sigma_c}\right| + \left|\frac{\sigma_{\theta}}{\sigma_t}\right| < 1 \rightarrow \left|\frac{-12500}{-55000}\right| + \left|\frac{12500}{17000}\right| = 0.96 < 1$ Therefore the hemispherical dome can be considered safe by Mohr's critetrion. The numerical results obtained with the Abaqus model are shown in Fig. 3.20 and 3.21:

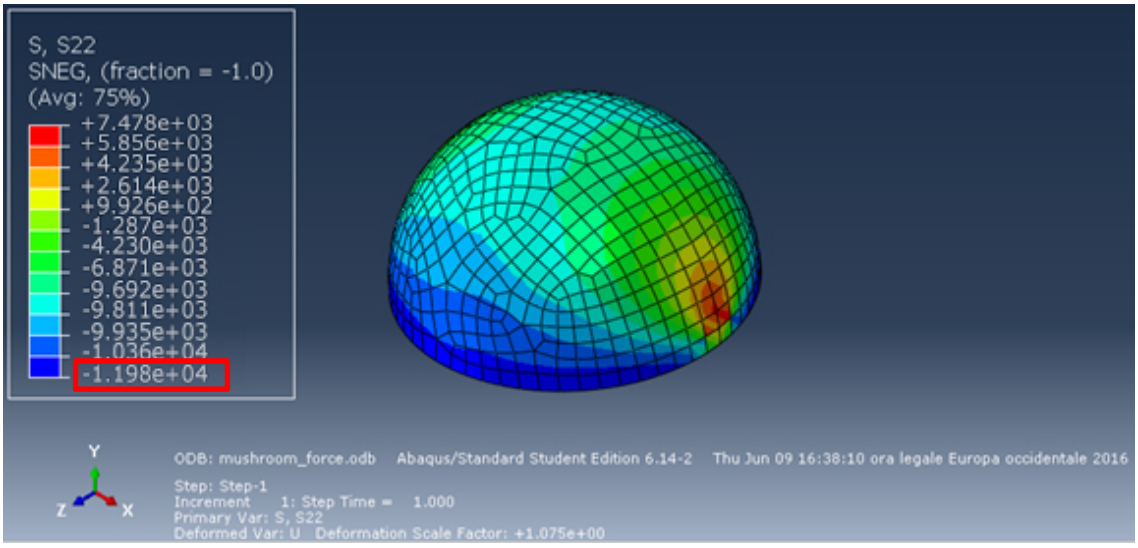

Figure 3.22. Illustration of the meridional stresses

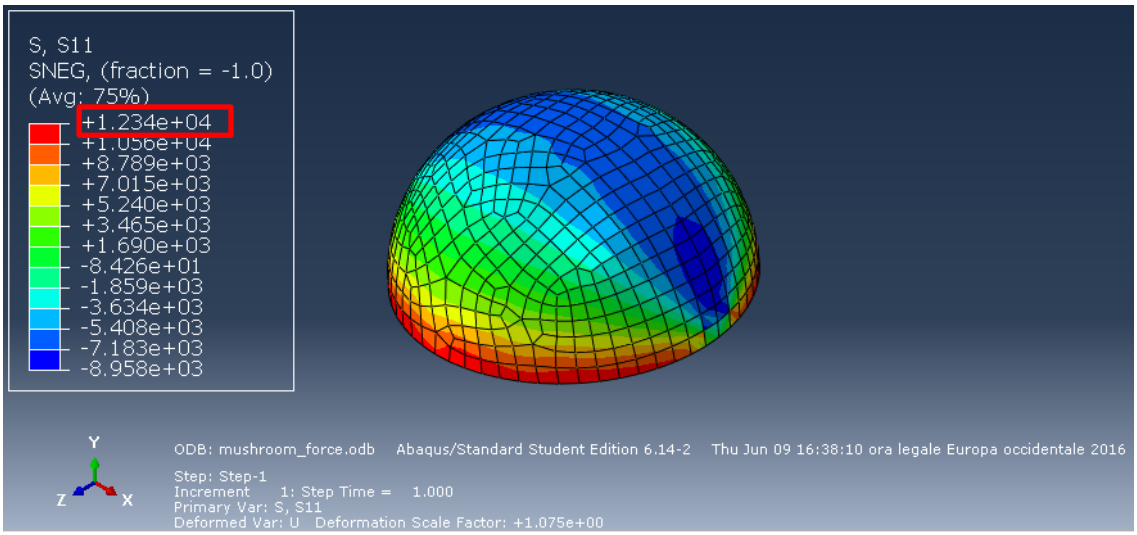

Figure 3.23. Illustration of the hoop stresses

As it can be seen in the Table 3.4, the numerical and analytical solutions are close, validating further the numerical model. The considerations about how to increase the accuracy are obviously valid also for this case.

Table 3.4: Stress generated by a uniform

load over a horizontal projection of the dome surface.

CASE 2	UNIFORM LOAD OVER AN HORIZONTAL PROJECTION OF THE DOME SURFACE		
	σ_Φ (Pa)	σ_θ (Pa)	**Mohr's Criterion**
Analytical Solution	-12500	12500	0.96
Numerical Solution	-11980	12340	0.94

Therefore it can be affirmed that, according to the linear analysis, the material strength is higher than the stresses sustained by the structure when it is subjected to a uniform load over the horizontal projection of the dome surface p = 500 Pa. Considering again an arch at a sufficient distance from the pinned points it is possible to plot the correct stress distributions (Fig.3.24).

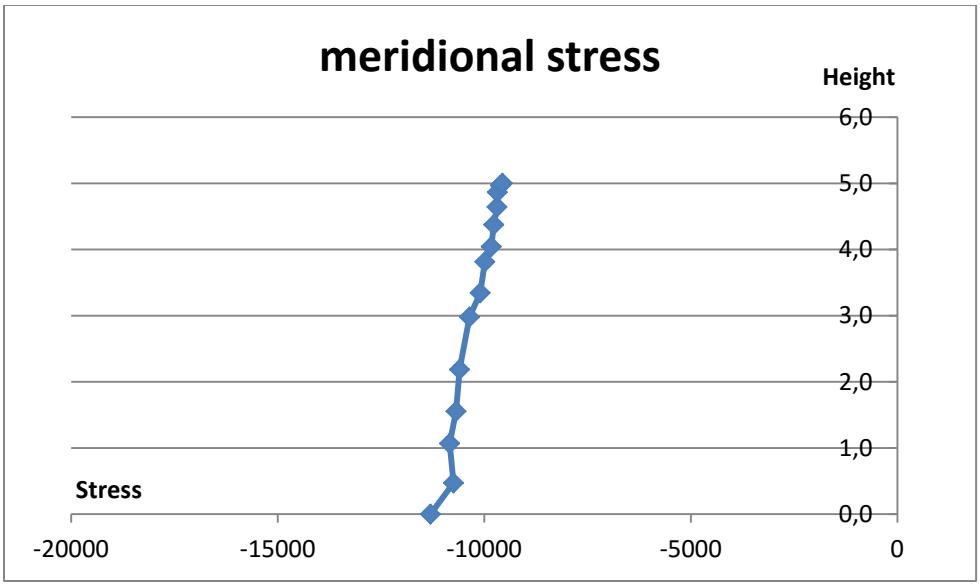

Figure 3.24. Meridional stress vs height plot

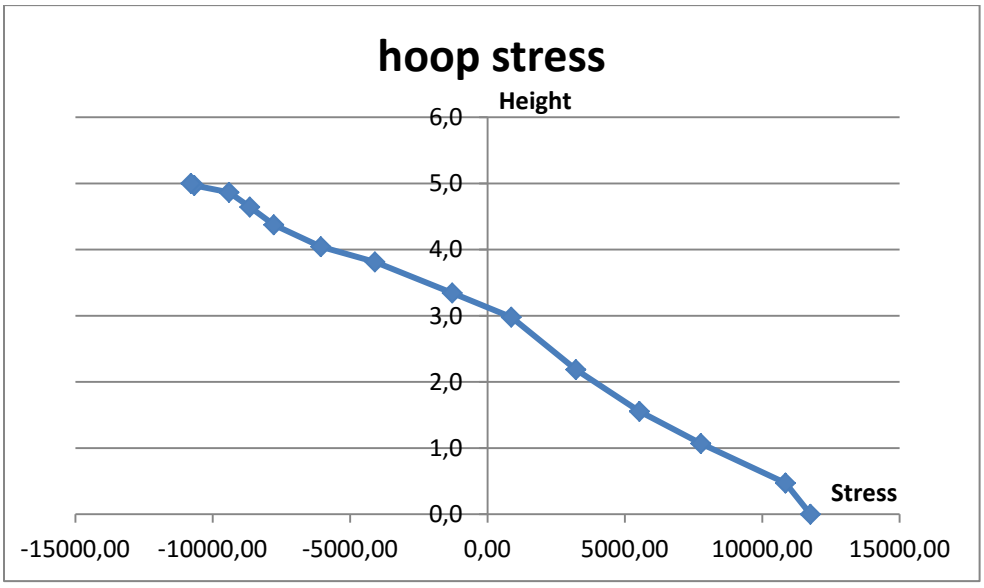

Figure 3.25. Hoop stress vs height plot

Case 3: Uniform external pressure over the dome surface: p = 1000 Pa

As it has been already shown, the analytical solution for a hemispherical dome subjected to a uniform external pressure can be computed according to Eq. 3.28 and 3.29:

$$N'_{\Phi} = -\frac{\pi a^2 p \sin^2\Phi}{2 a \sin^2\Phi} = -\frac{a p}{2} \qquad \text{[Eq 3.32]}$$

$$N'_{\theta} = -a\left(p - \frac{a p}{2a}\right) = -\frac{a p}{2} \qquad \text{[Eq 3.33]}$$

Meridional force: $N'_{\Phi} = -\frac{a p}{2} = -\frac{5 \cdot (1000)}{2} = -2500$ N/m

Hoop force: $N'_{\theta} = -\frac{a p}{2} = -\frac{5 \cdot (1000)}{2} = -2500$ N/m

Dividing now by the thickness t of the dome, we obtained the following internal stresses:

Meridional stress: $\sigma_{\Phi} = \frac{N'_{\Phi}}{t} = \frac{-2500}{0{,}1} = -25000$ Pa

Hoop stress: $\sigma_{\theta} = \frac{N'_{\theta}}{t} = \frac{-2500}{0{,}1} = -25000$ Pa

Since the edge is subjected only to compression, according to the Mohr's failure criterion: $\left|\frac{\sigma_{\Phi}}{\sigma_c}\right| + \left|\frac{\sigma_{\theta}}{\sigma_t}\right| < 1 \rightarrow \left|\frac{-25000}{-55000}\right| + \left|\frac{0}{17000}\right| = 0.45 < 1$

Therefore the hemispherical dome can be considered safe by Mohr's critetrion. In this case the distribution of the stresses is constant along the dome surface. However, due to a non-optimal level of refinement of the mesh, this result has been partially obtained with the Abaqus as it can be seen in Fig 3.22 and 3.23:

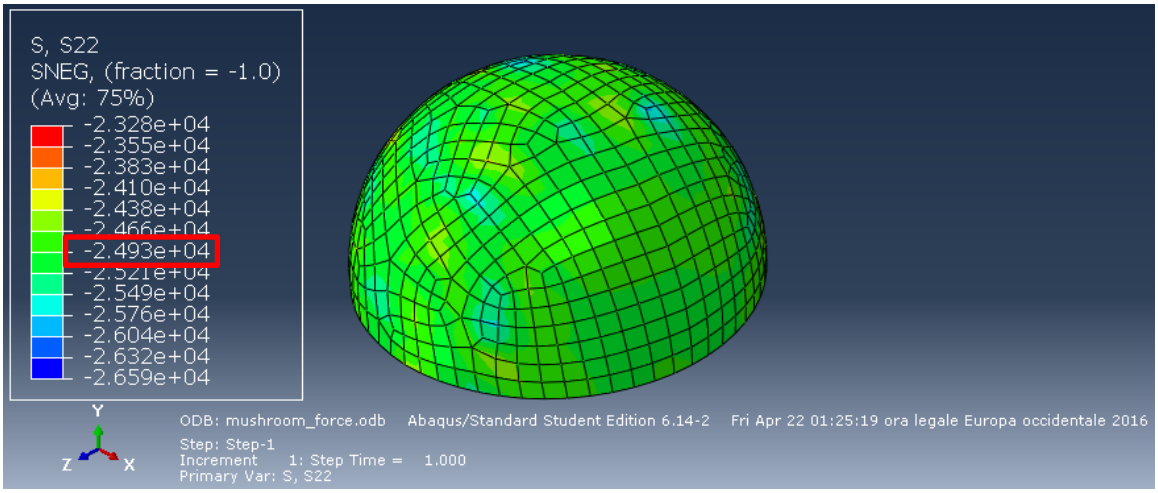

Figure 3.26. Illustration of the meridional stresses

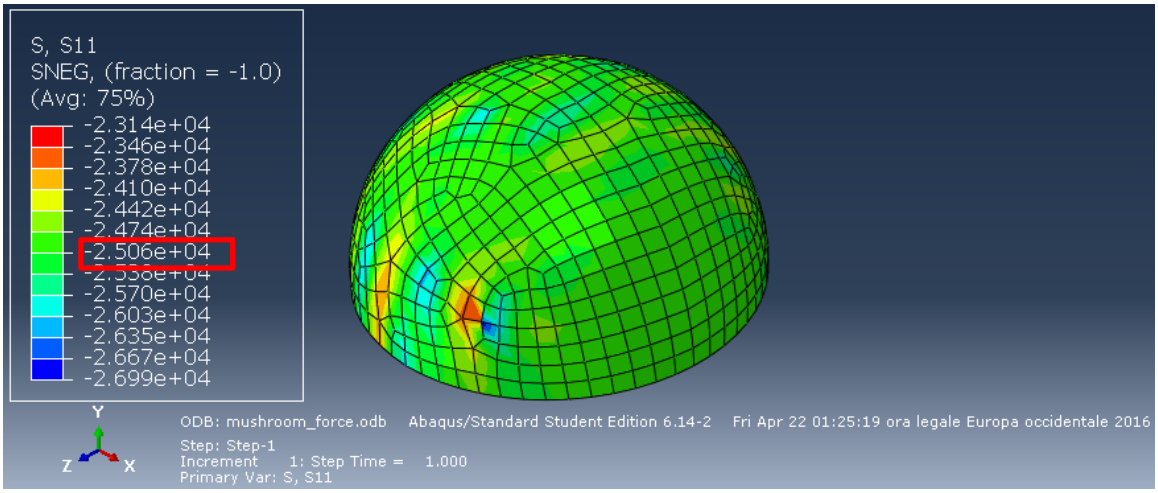

Figure 3.27. Illustration of the hoop stresses

As it can be seen in the Table 3.5, the numerical and analytical solutions are close, validating further the numerical model. The considerations about how to increase the accuracy are obviously valid also for this case.

Table 3.5. Stresses generated by a uniform external pressure over the dome surface.

CASE 3	UNIFORM EXTERNAL PRESSURE ALONG THE DOME SURFACE		
	σ_Φ (Pa)	σ_θ (Pa)	**Mohr's Criterion**
Analytical Solution	-25000	-25000	0.45
Numerical Solution	-24930	-25060	0.46

Therefore it can be affirmed that, according to the linear analysis, the material strength is higher than the stresses sustained by the structure when it is subjected to a uniform external pressure p = 1000 Pa. For each scenario it has been shown how the hemispherical dome can be considered safe according to the Mohr's criterion. However, this first analysis does not exclude the possibility of other type of failure, such as buckling, which will be discuss in the next chapter. Considering again an arch at a

sufficient distance from the pinned points it is possible to plot the correct stress distributions (Fig.3.28).

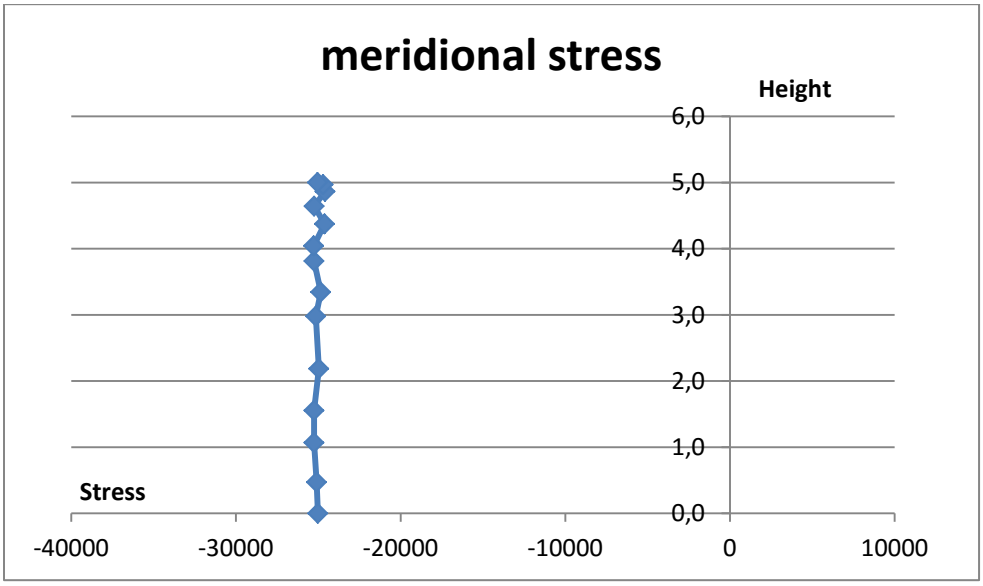

Figure 3.28. Meridional stress vs height plot

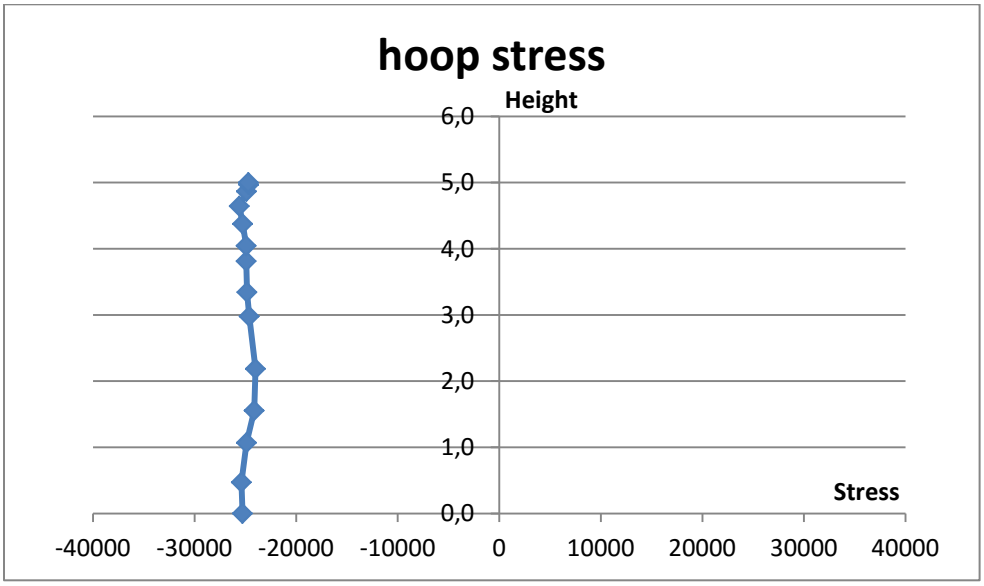

Figure 3.29. Meridional stress vs height plot

3.4.3 Influence of the geometrical parameters

The second type of comparison focuses the geometry of the domes, in order to verify that the analytical and the numerical solution provide similar results. Therefore, different

values of the angle of cut, different values of thickness and different of radius have been considered separately. Since the previous section revealed that the validity of the numerical models does not depend on the type of loading, only a uniform load over the dome surface was considered as acting load on the dome models. All the geometrical variations respect to the original configuration are shown in Table 3.6.

Table 3.6. Variation of the geometrical parameters of the domes

DIFFERENT VALUE OF THE ANGLE OF CUT							
Case	**φ (deg)**	**t (m)**	**a (m)**	**V (m^3)**	**W (N)**	**S (m^2)**	**q (Pa)**
A	**30**	0.1	5	1.5	1888.5	21.0	89.7
B	**45**	0.1	5	3.8	4810.4	46.0	104.6
C	**60**	0.1	5	7.1	9074.2	78.5	115.5
DIFFERENT VALUE OF THE THICKNESS							
Case	**φ (deg)**	**t (m)**	**a (m)**	**V (m^3)**	**W (N)**	**S (m^2)**	**q (Pa)**
D	90	**0.05**	5	7.8	9916.4	157.1	63,1
E	90	**0.2**	5	30.2	38483.5	157.1	245.0
F	90	**0.4**	5	57.9	73890.0	157.1	470.4
DIFFERENT VALUE OF THE RADIUS							
Case	**φ (deg)**	**t (m)**	**a (m)**	**V (m^3)**	**W (N)**	**S (m^2)**	**q (Pa)**
G	90	0.1	**2.5**	3.8	4810.4	39.3	122.5
H	90	0.1	**10**	62.2	79330.8	628.3	126.3
I	90	0.1	**15**	140.4	179092.0	1413.7	126.7

The comparison in terms of stresses between the analytical and the numerical solution is summarized in the Table 3.7.

Table 3.7. Comparison between the analytical and numerical solutions for different geometries

CASE A	UNIFORM LOAD OVER THE DOME SURFACE		
	σ_Φ (Pa)	**σ_θ** (Pa)	**Mohr's Criterion**
Analytical Solution	-2405	-1481	0.13
Numerical Solution	-2376	-1412	0.13
CASE B	UNIFORM LOAD OVER THE DOME SURFACE		

	σ_Φ (Pa)	σ_θ (Pa)	**Mohr's Criterion**
Analytical Solution	-3062	-634	0.09
Numerical Solution	-2990	-601	0.09
CASE C	UNIFORM LOAD OVER THE DOME SURFACE		
	σ_Φ (Pa)	σ_θ (Pa)	**Mohr's Criterion**
Analytical Solution	-3851	963	0.13
Numerical Solution	-3894	978	0.13

CASE D	UNIFORM LOAD OVER THE DOME SURFACE		
	σ_Φ (Pa)	σ_θ (Pa)	**Mohr's Criterion**
Analytical Solution	-6313	6313	0.49
Numerical Solution	-6374	6127	0.48
CASE E	UNIFORM LOAD OVER THE DOME SURFACE		
	σ_Φ (Pa)	σ_θ (Pa)	**Mohr's Criterion**
Analytical Solution	-6125	6125	0.47
Numerical Solution	-6160	6084	0.47
CASE F	UNIFORM LOAD OVER THE DOME SURFACE		
	σ_Φ (Pa)	σ_θ (Pa)	**Mohr's Criterion**
Analytical Solution	-5880	5880	0.45
Numerical Solution	-5991	6102	0.47

CASE G	UNIFORM LOAD OVER THE DOME SURFACE		
	σ_Φ (Pa)	σ_θ (Pa)	**Mohr's Criterion**
Analytical Solution	-3062	3062	0.24
Numerical Solution	-2955	2984	0.23
CASE H	UNIFORM LOAD OVER THE DOME SURFACE		
	σ_Φ (Pa)	σ_θ (Pa)	**Mohr's Criterion**
Analytical Solution	-12625	12625	0.97
Numerical Solution	-12750	12250	0.95
CASE I	UNIFORM LOAD OVER THE DOME SURFACE		
	σ_Φ (Pa)	σ_θ (Pa)	**Mohr's Criterion**
Analytical Solution	-19002	19002	1.46
Numerical Solution	-18890	18220	1.42

The comparison shows similar results between the analytical and the numerical solution, confirming further the validity of the finite element models. Looking at cases A, B and C, one can observe that the meridional stress increases according to the rise of the angle of cut, while the hoop stress decreases becoming in tension in case C, cause the angle of cut

(ϕ = 60°) is greater than 51°50'. Moreover, according to cases G, H and I, the principal stresses increase with the increase of the radius. Also this result makes sense, because increasing the radius implies that a bigger volume and consequently a larger weight of the structure is considered. Nonetheless, when the radius is bigger than 10 m, the Mohr's criterion is no longer satisfied as the tension in the hoop stresses becomes greater of the ultimate tensile strength. Therefore, for large scale structures the use of reinforcement becomes necessary. Similarly, a reduction of the stresses was expected by increasing the thickness. However, for the three values of the thickness considered in cases C, D and F, almost the same result in terms of stresses was obtained. In fact, the increase in the thickness seems to impact in the weight and the stress experienced by the structure in approximately the same ratio. Therefore, when a lightweight material with low stiffness such as mycelium is used for a dome, increasing the thickness does not necessarily provide a lower level of stresses. A greater level of stiffness should occur through other considerations such as changing the shape.

3.4.4 Influence of the material properties

The third comparison focuses on the performance of different construction materials, through the investigation of mycelium and concrete. As it is well-known the material properties of concrete are not standard vary according to its composition, class of resistance, production process, etc. The selected concrete of this study belongs C25/30 with average properties summarized in Table 3.8.

Table 3.8. Material properties of concrete [36]

MATERIAL PROPERTIES OF CONCRETE				
Density (kg/m^3)	**Tensile Strength (MPa)**	**Elastic Modulus (MPa)**	**Compressive Strength (MPa)**	**Poisson Ratio**
2500	1.55	31500	25	0.15

For comparison and consistency purposes, the same geometry of hemispherical dome (angle of cut $\phi = 90°$) with a radius r = 5m and a thickness t = 0.1 was considered. According to the membrane theory, the behavior of a dome subjected to a uniform load over a horizontal projection of the dome surface or to a uniform external pressure does not depend on the material properties. Therefore, concrete has been considered as a construction material only for the case of a dome subjected to its own weight. However, this first analysis does not exclude the possibility of other type of failure, such as buckling, which will be discuss in the next chapter.

Case L: Uniform load over the Dome surface: p = self-weight

Volume of the dome : $V = \frac{1}{2}(Vol_{sphere\_full} - Vol_{sphere\_empty})$

$V = \frac{1}{2}[\frac{4}{3}\pi a^3 - \frac{4}{3}\pi (a - t)^3] = \frac{1}{2}\cdot[\frac{4}{3}\pi 5^3 - \frac{4}{3}\pi (5 - 0.1)^3] = 15.4\ m^3$

Weight of the dome: $W = V\ \delta\ g = 15.4 \cdot 2500 \cdot 9.81 = 377685\ N$

Surface of the hemisphere: $S = \frac{1}{2} S_{sphere} = \frac{1}{2}\cdot 4\ \pi\ a^2 = 2 \cdot \pi \cdot 5^2 = 157.1\ m^2$

Pressure on dome surface: $q = -\frac{W}{S} = -\frac{377685}{157.1} = -2404.1\ Pa$

Since the maximum values of the stresses occur at the edge ($\phi = 90°$), according to Eq. 3.24 and 3.25:

Meridional force: $N'_{\Phi} = -aq\frac{1}{1+\cos\Phi} = -5 \cdot (-2404.1) \cdot \frac{1}{1+\cos(90°)} = 12020.5\ N/m$

Hoop force: $N'_{\theta} = aq(\frac{1}{1+\cos\Phi} - \cos\Phi) = 5 \cdot (-2404.1) \cdot (\frac{1}{1+\cos(90°)} - \cos(90°))$

$N'_{\theta} = -\ 12020.5 N/m$

Dividing now by the thickness t of the dome, the following stresses have been obtained:

Meridional stress: $\sigma_{\Phi} = \frac{N'_{\Phi}}{t} = \frac{12020.5}{0.1} = 120205\ Pa$

Hoop stress: $\sigma_\theta = \frac{N'_\theta}{t} = -\frac{12020.5}{0.1} = -120205$ Pa

Since the edge is subjected both to tension and compression, according to the Mohr's failure criterion: $\left|\frac{\sigma_\Phi}{\sigma_c}\right| + \left|\frac{\sigma_\theta}{\sigma_t}\right| < 1 \rightarrow \left|\frac{-120205}{-25000000}\right| + \left|\frac{120205}{1550000}\right| = 0.08 < 1$

Table 3.9. Stresses generated by a uniform load over the dome surface (self-weight)

CASE L	UNIFORM LOAD OVER THE DOME SURFACE		
	σ_Φ (Pa)	σ_θ (Pa)	**Mohr's criterion**
Analytical Solution	-120205	120205	0.08
Numerical Solution	-117500	120700	0.08

As it can be seen in Table 3.9, the analytical and the numerical solution are similar, therefore the numerical model is considered valid. Therefore it can be affirmed that, according to the linear analysis, the material strength is higher than the stresses sustained by the structure. Although the concrete dome experiences larger stresses compared to the mycelium dome, stresses always remain lower to the ultimate strength of the material as expressed by the Mohr s criterion. Here it is interesting to report that the specific strength of concrete defined as the ratio between the ultimate strength and the density of the material is close to five times larger compared with the specific strength of mycological fungi.

3.4.5 Influence of the boundary conditions

The results of the membrane theory, as well as the ones obtained with the finite element software, are based on the assumption that the structure is simply supported. In this section it has investigated the effect of boundary conditions. Since an analytical solution does not exist for other boundary conditions, the following results were obtained using the finite element software only. Therefore, fixed boundary conditions were considered

everywhere along the base of the dome and the same cases were analyzed. A comparison between the supported and the fixed conditions is shown in Table 3.10 for Case 1 2 3.

Table 3.10. Comparison between supported and fixed boundary conditions

CASE 1	UNIFORM LOAD OVER THE DOME SURFACE		
	σ_Φ (Pa)	σ_θ (Pa)	**Mohr's Criterion**
Fixed Condition	-8379	3312	0.35
Supported Condition	-6110	6294	0.47
CASE 2	UNIFORM LOAD OVER AN HORIZONTAL PROJECTION OF THE DOME SURFACE		
	σ_Φ (Pa)	σ_θ (Pa)	**Mohr's Criterion**
Fixed Condition	-16430	6492	0.68
Supported Condition	-11980	12340	0.94
CASE 3	UNIFORM EXTERNAL PRESSURE		
	σ_Φ (Pa)	σ_θ (Pa)	**Mohr's Criterion**
Fixed Condition	-43030	-27200	0.78
Supported Condition	-25060	-24930	0.46

Table 3.10 reveals the effect of fixed boundary conditions in the distribution of stresses. Looking at cases 1 and 2, the maximum value of compression and tension, which again belong to the meridional and hoop stresses respectively, do not occur at the edges of the dome, but in another region above it. Moreover, even though the maximum compression is higher for fixed supports, the maximum tension is much lower making the dome safer as expressed by Mohr's criterion. Conversely, in case 3, both meridional and hoop stresses are in pure compression and higher for the fixed conditions, making the domes less safe by Mohr's criterion.

3.5 Case study

3.5.1 Dome of the basilica of San Luca

As a first case study, the hemispherical dome of the basilica of San Luca has been analyzed. Even if the basilica was built in the XII century, the present dome is the result

of a project of restoration and extension designed by the architect Carlo Francesco Dotti in 1723. Few years later a lantern was built on the top of the dome. The dominant style of the dome is baroque and the used material is the “Italian” solid brick, which belongs to the architectural tradition of the city. A summary of the estimated material properties is given in Table 3.11:

Table 3.11. Material properties of “Italian” brick [37]

MATERIAL PROPERTIES OF THE “BOLOGNESE” BRICK				
Density (kg/m^3)	**Tensile Strength (MPa)**	**Elastic Modulus (MPa)**	**Compressive Strength (MPa)**	**Poisson Ratio**
1800	0.8	10000	7	0.25

The general dimensions of the dome and the lantern instead were obtained from the archives of the “Soprintendenza of Bologna”.

Figure 3.30. Picture of the basilica of San Luca [38]

The following two figures represent the planimetry and altimetry of the basilica, respectively.

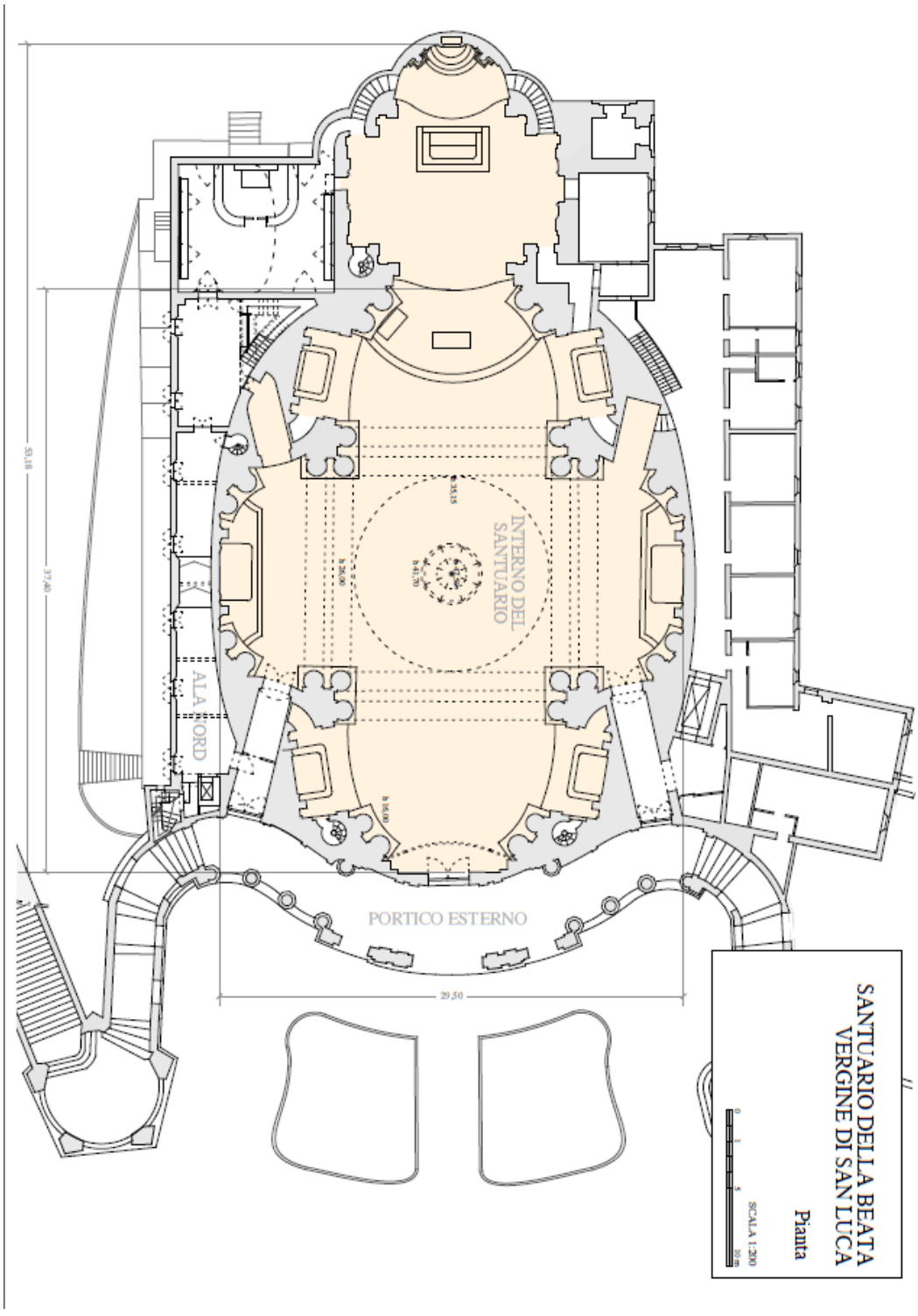

Figure 3.31. Planimetry of the basilica of Bologna [39]

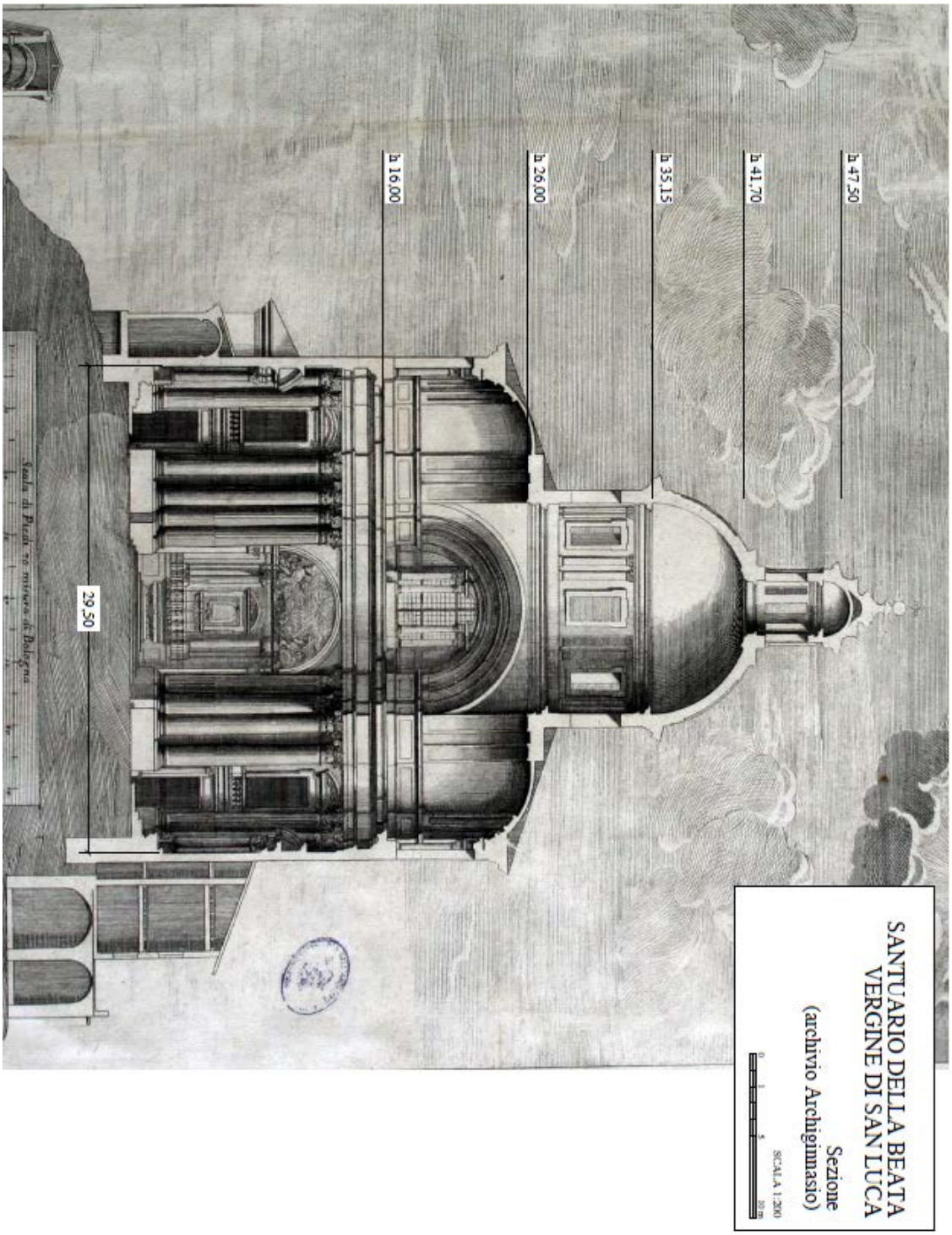

Figure 3.32. Altimetry of the basilica of Bologna [39]

The dimensions of the dome and the lantern are presented in Table 3.12 and 3.13.

Table 3.12. Geometrical dimensions of the dome of San Luca

DOME				
$R_{ext.}$ (m)	$R_{int.}$ (m)	$R_{av.}$ (m)	t (m)	$h_{av.}$ (m)
6.20	5.52	5.86	0.68	5.86

Table 3.13. Geometrical dimension of the lantern of San Luca

LANTERN				
$R_{ext.}$ (m)	$R_{int.}$ (m)	$R_{av.}$ (m)	t (m)	$h_{av.}$ (m)
1.92	1.54	1.73	0.38	5.80

Where R_{ext} and R_{int} are respectively the external and internal radius and h_{av} is the average height. Since the aim of this research is to study the behavior of domes, the interactions dome-walls and dome-lantern were neglected. Moreover, the analysis was conducted by considering the following assumptions:

- The dome is pinned all along its base
- The dome is an hemisphere with constant material properties and thickness
- The lantern is a cylinder with constant material properties and thickness
- The effect of the lantern on the dome is the same of a distributed load acting on a portion of the dome surface equal to the area of the base of the lantern.
- The forces acting on the dome are the self-weight and the distributed load coming from the lantern

The weight of the lantern was converted in a distributed load as presented below:

Area of the base of the lantern: $A = \pi (R_{ext}^2 - R_{int}^2) = \pi \cdot (1.92^2 - 1.54^2) = 4.13\ m^2$

Volume of the lantern: $V = A\ h = 4.13 \cdot 5.8 = 23.96\ m^3$

Weight of the lantern: $W = \delta\ V = 1800 \cdot 23.96 = 43127.64\ Kg$

Weight force of the lantern: $F = W\ g = 43127.64 \cdot 9.81 = 423082.15\ N$

Area of influence of the lantern: $A_{infl.} = \pi R_{av.}^2 = 9.40\ m^2$

Equivalent distributed load: $P = \frac{F}{A} = \frac{423082.15}{9.40} = 45008.73\ Pa$

The stress generated by this distributed load and the self-weight are shown here below:

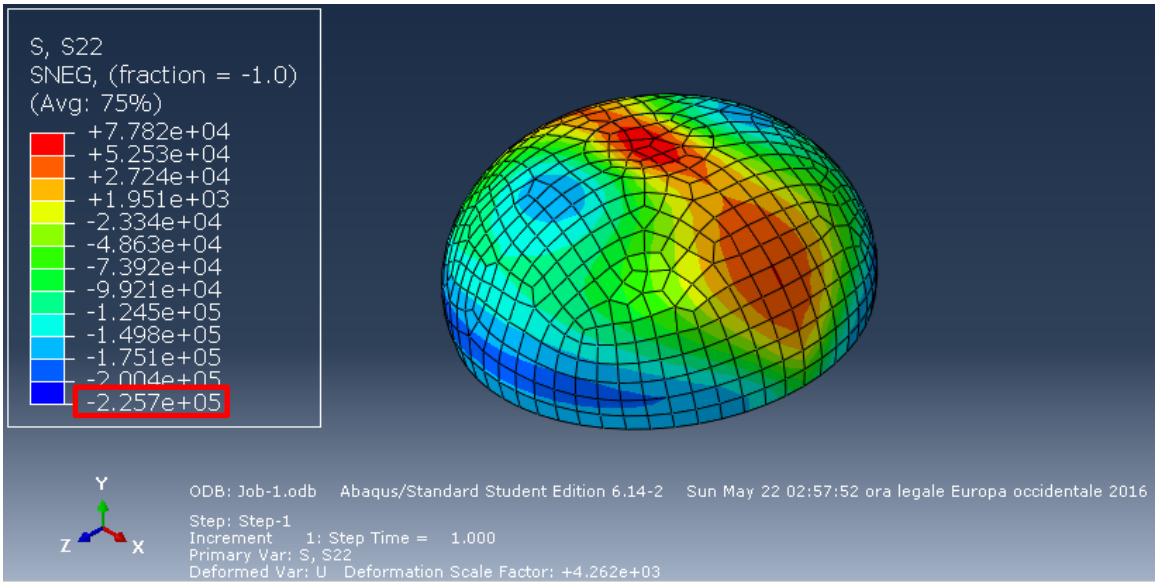

Figure 3.33. Illustration of the meridional stresses

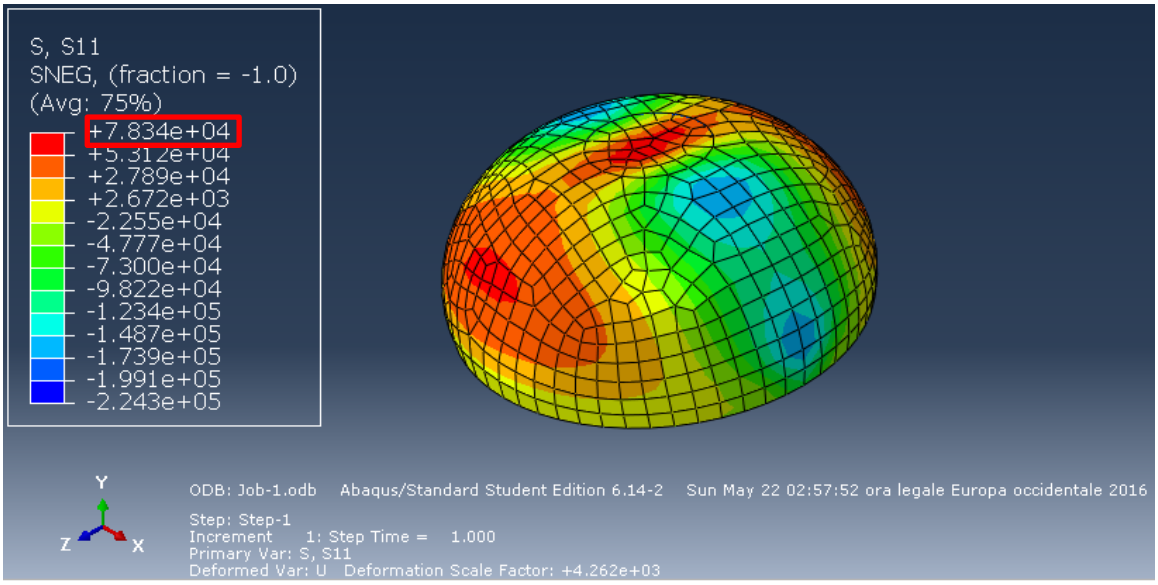

Fig. 3.34. Illustration of the hoop stresses

Since it is not easy to identify in which region of the dome the highest stresses occur, the maximum values of compression and tension identified were employed in Mohr's criterion, even if they do not occur in the part of the dome surface. According to Mohr's failure criterion:

$$\left|\frac{\sigma_\Phi}{\sigma_c}\right| + \left|\frac{\sigma_\theta}{\sigma_t}\right| < 1 \rightarrow \left|\frac{-225700}{-7000000}\right| + \left|\frac{78340}{800000}\right| = 0.13 < 1$$

Therefore it has been proved that the dome of San Luca is able su sustain its own weight and the lantern above it.

3.5.2 Dome of the sanctuary of Vicoforte

The dome of the sanctuary of Vicoforte is the largest masonry elliptical domes of the world. The construction of the sanctuary started in the 1596 thanks to the will of the duke Carlo Emanuele I Savoia. However, due to the settlements of the soil foundation, the construction phase was interrupted for several decades. It was only at the beginning of the XVIII century, when thanks to a new project by architect Francesco Gallo, that the realization of the dome restarted. The dome was finally realized in 1732. The predominant style of the sanctuary is baroque and the construction material is again the "Italian" solid brick. The material properties were already summarized in Table 3.8.

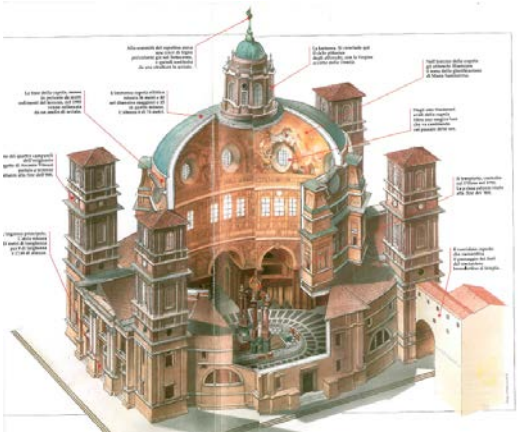

Figure 3.35. Illustration of the sanctuary of Vicoforte [40]

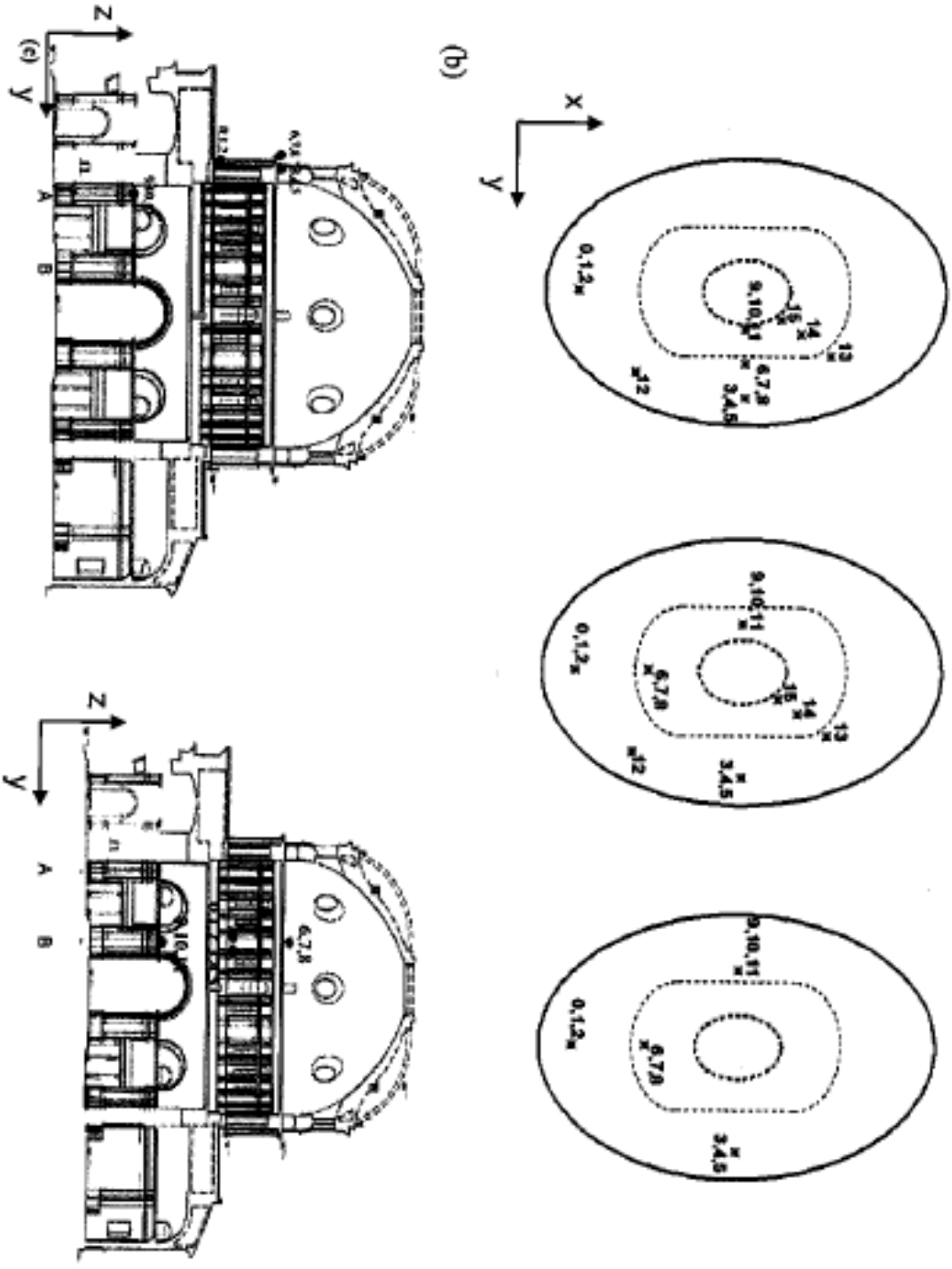

Figure 3.36. Planimetry of the the sanctuary of Vicoforte [40]

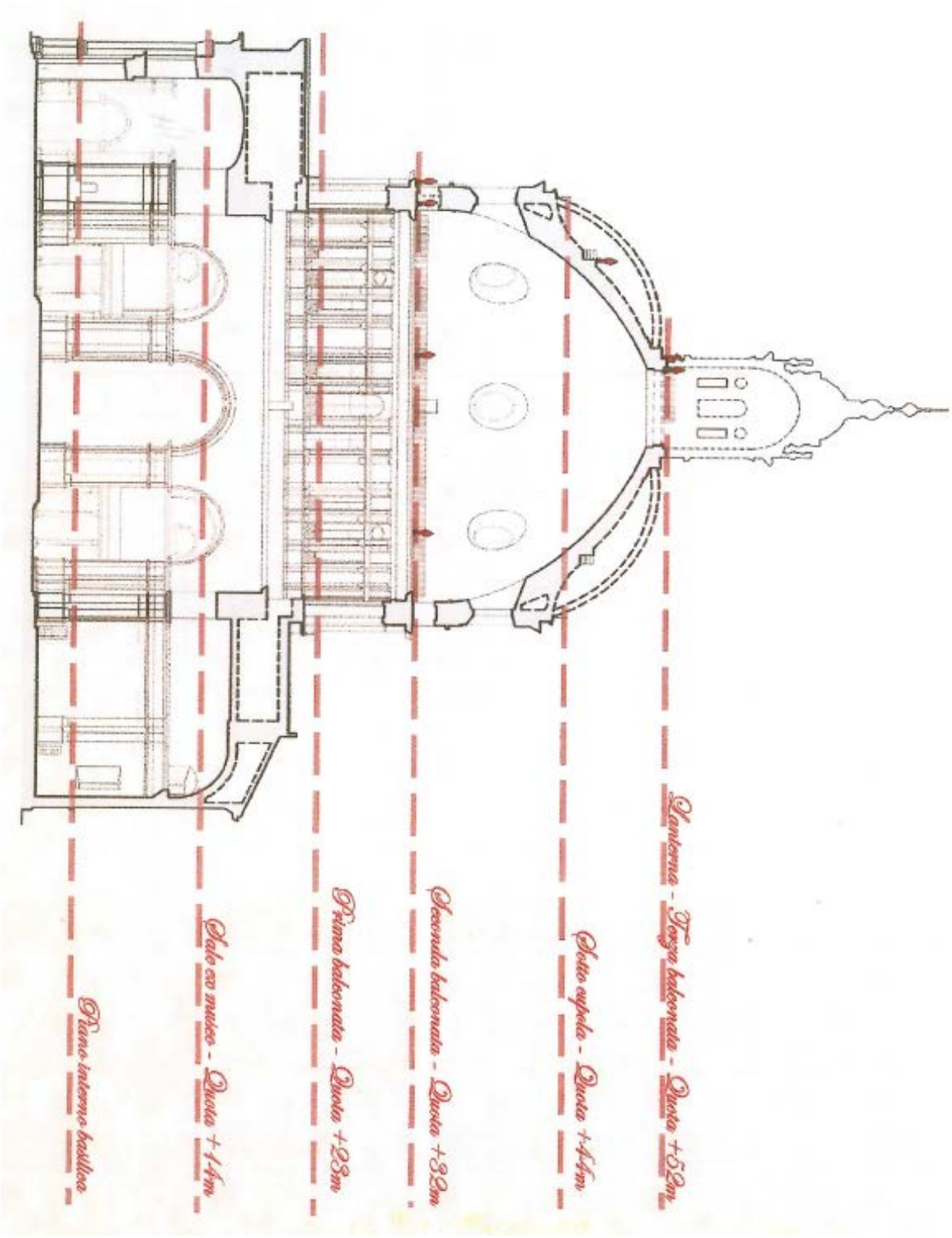

Figure 3.37. Altimetry of the sanctuary of Vicoforte [40]

Summing up the geometrical dimensions of the dome and the lantern:

Table 3.14. Geometrical dimensions of the dome of Vicoforte

DOME			
$a_{av.}$ (m)	$b_{av.}$ (m)	$c_{av.}$ (m)	t (m)
18.6	12.5	20	0.68

Table 3.15. Geometrical dimension of the lantern of Vicoforte

LANTERN				
$R_{ext.}$ (m)	$R_{int.}$ (m)	$R_{av.}$ (m)	t (m)	$h_{av.}$ (m)
2.8	2.4	2.6	0.4	8.4

Where a_{av} b_{av} and c_{av} are the three semi-axis of the ellipsoid. The analysis of the dome follows the same assumptions and procedure discussed for the case study of the dome of basilica di San Luca. The base of the dome was considered pinned and the lantern was converted in the following equivalent distributed load:

Equivalent distributed load: $P = \frac{F}{A} = \frac{969245.98}{21.24} = 45633.05$ Pa

The distributions of the stresses are shown in Fig. 3.31 and 3.32:

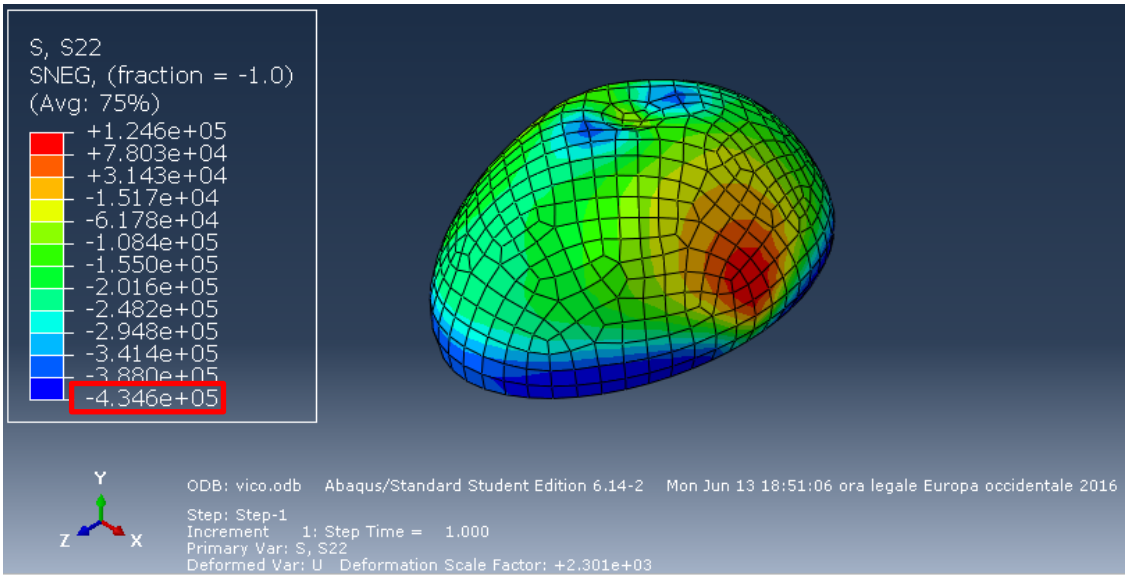

Figure 3.38. Illustration of the meridional stresses

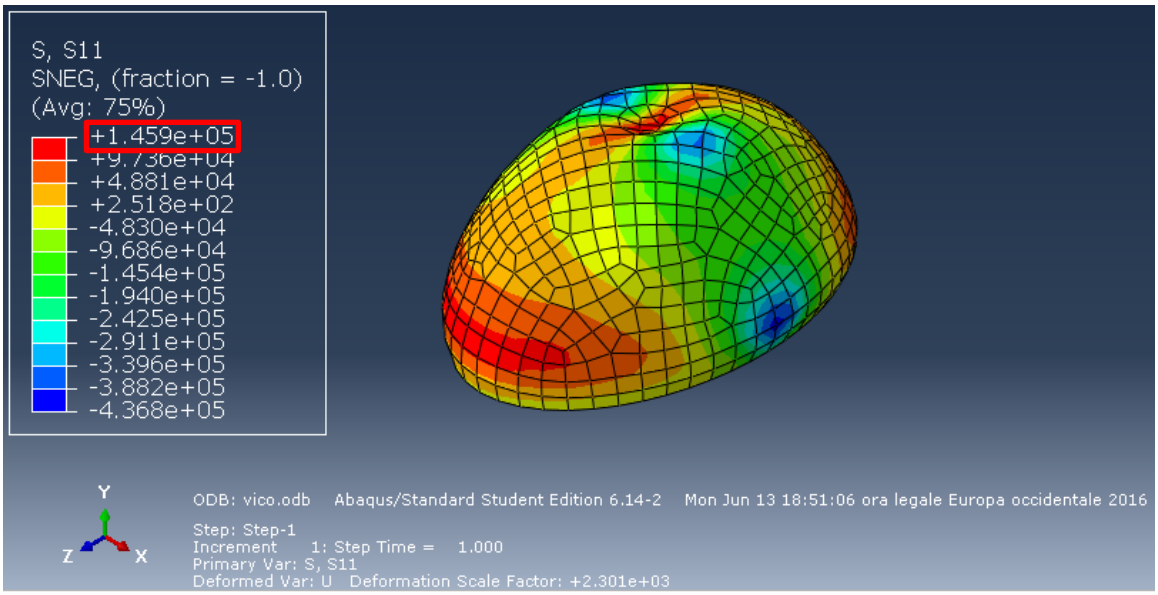

Figure 3.39. Illustration of the hoop stresses

The same considerations regarding the stress already discussed for the dome of San Luca are also valid in this case study. According, to the Mohr's failure criterion:

$$\left|\frac{\sigma_{\Phi}}{\sigma_c}\right| + \left|\frac{\sigma_{\theta}}{\sigma_t}\right| < 1 \rightarrow \left|\frac{-434600}{-7000000}\right| + \left|\frac{145900}{800000}\right| = 0.24 < 1$$

Therefore it has been proved that the dome of Vicoforte is able su sustain its own weight and the lantern above it.

Chapter 4: Buckling Analysis

4.1 Buckling theory

In engineering, buckling is defined as an instability which can result to a failure mode. Buckling is the consequence of a bifurcation in the analytical solution of the static equilibrium equations. Such bifurcation, with the increasing of the load, leads to two possible different states of equilibrium: state of pure compression or state with lateral deformation. Therefore, a failure due to buckling implies an abrupt side-way deflection of the structural element when it is subjected to high values of compression. However, this compression is always smaller than the ultimate compressive strength of the material. The main causes of this phenomenon are imperfections, which may involve the geometry, the material or the point of application of the load. From a modeling point of view, the effects of the imperfections can be taken into account by introducing in the structural model an “artificial” axial load eccentricity. Once the structural member buckles, it might still be able to carry the load, if the deformations are not catastrophic. However, in many cases, buckling leads to a completely loss of the carrying capacity of the structural member. Moreover for complex structures, such as shells, the design phase may include multiple bifurcation points which involve multiple buckling modes. In these conditions the different buckling modes can interact each other influencing the overall behavior of the structure. This particular phenomenon of interaction can strongly reduce the general load-carrying capacity of the structure. The buckling strength of shells is usually determined by combining theoretical considerations with experimentally determined correlation factors [3].

However, the thin shell theory cannot explain alone the behavior of shells under buckling. In fact, for hemispherical domes the analytical solution exists only for spherical domes under external pressure. Therefore, for all other cases including different geometry or types of loading, the designer has to be aware that a reasonable level of safety can be reach only by conducting small-scale experiments and by considering previous experiences by other designers.

Buckling of spherical domes under uniform external pressure

The buckling of hemispherical domes under uniform external pressure is the only case that has been investigated analytically. The solution is thus valid only for spherical shells with the base restrained against translation, but still free to rotate. The equation for the bifurcation buckling of spherical domes under axisymmetrical radial pressure can be expressed as follow:

$$P_{cr} = \frac{2}{\sqrt{[3\,(1-\nu^2)]}}\,E\,\left(\frac{t}{a}\right)^2 \qquad \text{[Eq. 4.1]}$$

Where:

E is the elastic modulus

v is the Poisson ratio

t is the thickness

a is the radius of curvature

4.2 Comparisons

4.2.1 Assumptions

The aim of this section is to compare the analytical and the numerical solutions in order to confirm the validity of the buckling models created with the finite element software. Since an analytical solution is available only for the case of uniform external pressure on

a hemispherical dome, the solution for the other types of load and geometries was numerically explored. A constant thickness along the dome surface was considered in each situation. Moreover, since the existing analytical solution is valid for pinned support conditions, the same typology was selected in the finite element model. The material employed is mycelium-based (see Table 3.2). Finally the study focuses on the first buckling mode (which is the one that corresponds to the minimum amount of energy), obtained through the Abaqus option to compute the first eigenvalue.

4.2.2 Influence of the type of loading

The first comparison involves a hemispherical dome (angle of cut $\phi = 90°$) with a radius r = 5m and a thickness t = 0.1m. According to Eq. 3.34:

$$P_{cr} = \frac{2}{\sqrt{[3\,(1-\nu^2)]}}\,E\,(\frac{t}{R})^2 = = \frac{2}{\sqrt{[3\,(1-0.25^2)]}} \cdot 690000 \cdot (\frac{0.1}{5})^2 = 329.15\ Pa$$

The dome was also modeled numerically using the finite element software. Considering pinned support conditions and constant thickness, the numerical results obtained with the finite element model are shown in Fig 4.1.

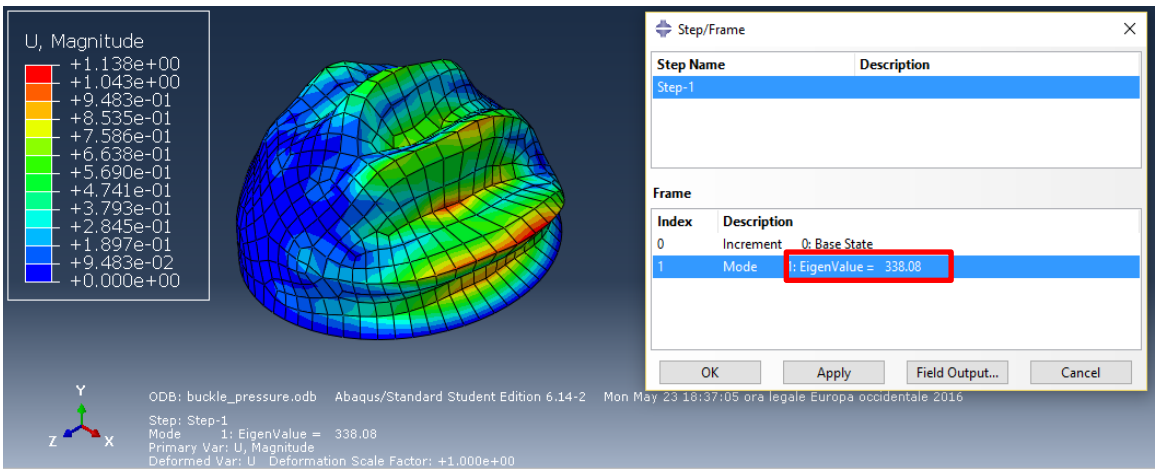

Figure 4.1. Illustration of the buckling of the hemispherical dome under uniform external pressure

The results are very similar (Analytical solution: P_{cr} = 329.15, Numerical solution: P_{cr} = 338.08), therefore the numerical model has to be considered valid. An even greater level of accuracy can be reached by increasing the refinement of the mesh, which in our case was limited by the student version. Since the value of the buckling load P_{cr} generated by the uniform external pressure is lower than the one used for the linear analysis (p = 1000 Pa), hemispherical dome is not able to sustain the prescribed uniform external pressure p = 1000 Pa employed in the linear analysis although the Mohr's criterion is satisfied.

4.2.3 Influence of the geometrical parameters

In this section, the geometry of the domes is explored for the buckling of the dome. Therefore, different values of the angle of cut, thickness and radius have been considered separately. Unfortunately analytical formulations of the buckling solution for configuration other than the hemisphere were not found in literature. Hence, a comparison between the analytical and the numerical model is given only for variations of the thickness and radius of the hemispherical dome. The different cases with respect to the original configuration are summarized in Table 4.1.

Table 4.1. Variation of the geometrical parameters of the domes

DIFFERENT VALUE OF THE ANGLE OF CUT			
Case	**φ (deg)**	**t (m)**	**a (m)**
A	**30**	0.1	5
B	**45**	0.1	5
C	**60**	0.1	5
DIFFERENT VALUE OF THE THICKNESS			
Case	**φ (deg)**	**t (m)**	**a (m)**
D	90	**0.05**	5
E	90	**0.2**	5
F	90	**0.4**	5

DIFFERENT VALUE OF THE RADIUS			
Case	**φ (deg)**	**t (m)**	**a (m)**
G	90	0.1	**2.5**
H	90	0.1	**10**
I	90	0.1	**15**

The analytical and numerical buckling loads for the aforementioned cases are reported in the Table 4.2.

Table 4.2. Buckling under uniform external pressure for different geometries

DIFFERENT VALUE OF THE ANGLE OF CUT	CRITICAL BUCKLING LOAD P_{cr} (Pa)	
	Analytical solution	**Numerical solution**
CASE A	N/A	332.80
CASE B	N/A	335.14
CASE C	N/A	337.62

DIFFERENT VALUE OF THE THICKNESS	CRITICAL BUCKLING LOAD P_{cr} (Pa)	
	Analytical solution	**Numerical solution**
CASE D	82.29	85.11
CASE E	1316.60	1337.7
CASE F	5266.39	5195.05

DIFFERENT VALUE OF THE RADIUS	CRITICAL BUCKLING LOAD P_{cr} (Pa)	
	Analytical solution	**Numerical solution**
CASE G	1316.60	1344.9
CASE H	82.29	85.11
CASE I	36.57	37.74

The result reveal that the value of the critical buckling load increases with the increase of the angle of cut and the thickness, while decreases with the increasing of the radius. The first trend can be explained by considering the fact that hemispheres are subjected both to tension and compression, while caps may be subjected just to compression depending on their angle of cut. The second and the third trend instead can be explained by considering

the fact that the buckling mode is controlled by the slenderness ratio $\frac{t}{R}$. However, the critical buckling loads P_{cr} generated by the uniform external pressure are in most cases lower than the value tested in the linear analysis (p = 1000 Pa). Therefore they represent an upper limit of the loads that the domes can actually sustain.

4.2.4 Expansion to another load case

In this section the buckling behavior was investigated for other types of loading, such as the uniform load over a horizontal projection of the dome surface. Since the literature does not cover this load case, the solution found using the numerical model solely. Therefore, further researches are necessary to prove the validity of the results. As a first investigation, the classical hemispherical dome (angle of cut ϕ = 90°) geometry with a radius r = 5 m and a thickness t = 0.1 m was analyzed. The results obtained with Abaqus are shown in Fig. 4.2:

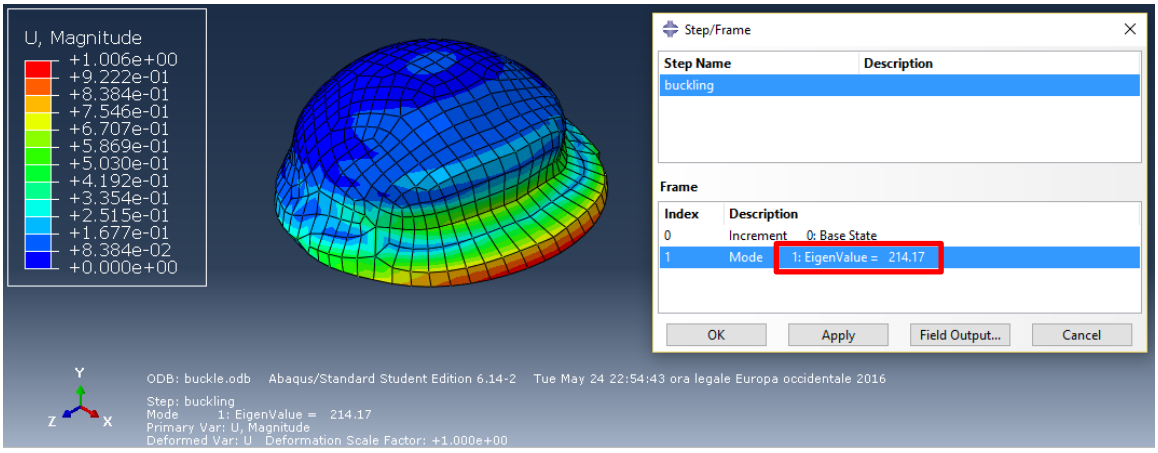

Figure 4.2. Illustration of the buckling of the hemispherical dome under uniform load over an horizontal projection of the dome surface

The critical buckling load F_{cr} corresponding to a uniform load over an horizontal projection over the dome surface for the standard hemispherical dome was found to be 214.17 Pa. The ratio between P_{cr} and F_{cr} is equal to 1.58. In order to see if there is a

correlation between P_{cr} and F_{cr}, it has been analyzed the same cases Table 4.1. The results obtained with Abaqus are summarized in Table 4.3.

Table 4.3. Buckling under uniform load over an horizontal projection of the dome surface

DIFFERENT VALUE OF THE ANGLE OF CUT	CRITICAL BUCKLING LOAD F_{cr} (Pa)
	Numerical solution
CASE A	332.40
CASE B	320.46
CASE C	294.48

DIFFERENT VALUE OF THE THICKNESS	CRITICAL BUCKLING LOAD F_{cr} (Pa)
	Numerical solution
CASE D	53.57
CASE E	862.13
CASE F	3471.4

DIFFERENT VALUE OF THE RADIUS	CRITICAL BUCKLING LOAD F_{cr} (Pa)
	Numerical solution
CASE G	884.53
CASE H	53.57
CASE I	23.9

To facilitate the comparison between the two critical buckling loads, it was decided to divide all the cases analyzed in two groups and to do the ratio between P_{cr} and F_{cr}:

- **Group 1**: Domes obtained by cutting an hemisphere: CASE A, CASE B, CASE C
- **Group 2**: Hemispherical domes with different values of the thickness or radius:

CASE D, CASE E, CASE F, CASE G, CASE H, CASE I

Table 4.4. Ratio P_{cr}/F_{cr} for domes obtained by cutting the hemisphere

Group 1	**P_{cr}** (Pa)	**F_{cr}** (Pa)	**Ratio**
CASE A	332.80	332.40	1.00
CASE B	335.14	320.46	1.05
CASE C	337.62	294.48	1.15

Table 4.4 reveals that increasing the angle of cut P_{cr} increases, while F_{cr}, therefore the ratio increases as a consequence. It is important to notice that for small values of the angle of cut the surface of the dome can be approximated with its horizontal projection, therefore the two types of loading are almost the same. This becomes clear if we compare the two types of loads for $\phi = 30°$ as it is shown in Fig 4.3 and 4.4:

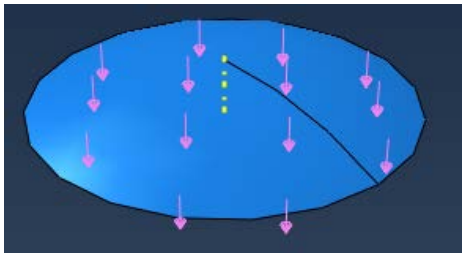

Figure 4.3. Sketch of the uniform vertical load

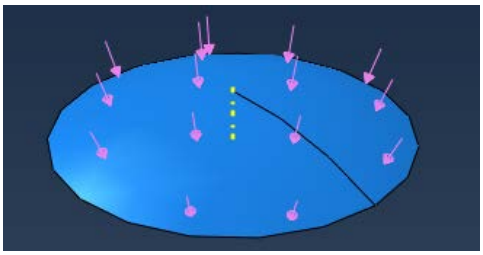

Figure 4.4. Sketch of the uniform external pressure

Table 4.5. Ratio P_{cr}/F_{cr} for hemispherical domes

Group 2	**P_{cr}** (Pa)	**F_{cr}** (Pa)	**Ratio**
CASE D	85.11	53.57	1.59
CASE E	1337.70	862.13	1.55
CASE F	5195.05	3471.40	1.50
CASE G	1344.90	884.53	1.52
CASE H	85.11	53.57	1.59
CASE I	37.74	23.90	1.58

Table 4.5 shows that when the geometry of the dome varies by increasing the thickness or the radius, the ratio between P_{cr} and F_{cr} remains almost constant. Since the range of values of the thickness and the radius that have been considered were limited

(0.05 m < t < 0.4 m, 2.5 m < r < 15 m), it has been decided to investigate greater values, in order to verify if such ratio remains constant. Therefore two additional cases were analyzed.

Table 4.6. Ratio P_{cr}/F_{cr} for to additional hemispherical domes

Case	φ (deg)	t (m)	a (m)	Pcr	Lcr	Ratio
L	90	1	5	32915	20996	1,57
M	90	0,1	50	3,29	2,24	1,47

The ratio between the two buckling loads is slightly different from before, but remains close to the 1.5 value. Therefore, it can be affirmed that the formulation of F_{cr} has the same degree of dependency of P_{cr} by the slenderness ratio and the material properties. However, the critical buckling loads F_{cr} generated by the uniform external pressure are in most cases lower than the value tested in the linear analysis (p = 500 Pa). Therefore they represent an upper limit of the loads that the domes can actually sustain.

4.2.5 Influence of the material properties

Focusing on the material employed, it has been decided to compare mycelium and concrete. The selected concrete of this study belongs C25/30 with average properties already summarized in Table 3.6. For comparison purposes, the same geometry of a hemispherical domes (angle of cut ϕ = 90°) with a radius r = 5m and a thickness t = 0.1is analyzed. According to Eq. 3.34:

$$P_{cr} = \frac{2}{\sqrt{[3\,(1-\nu^2)]}}\,E\,(\frac{t}{R})^2 = = \frac{2}{\sqrt{[3\,(1-0.15^2)]}} \cdot 31500{\cdot}10^6 \cdot\ (\frac{0.1}{5})^2 =\ 1.47{\cdot}10^7\ \text{Pa}$$

The numerical results are shown in Fig 4.5:

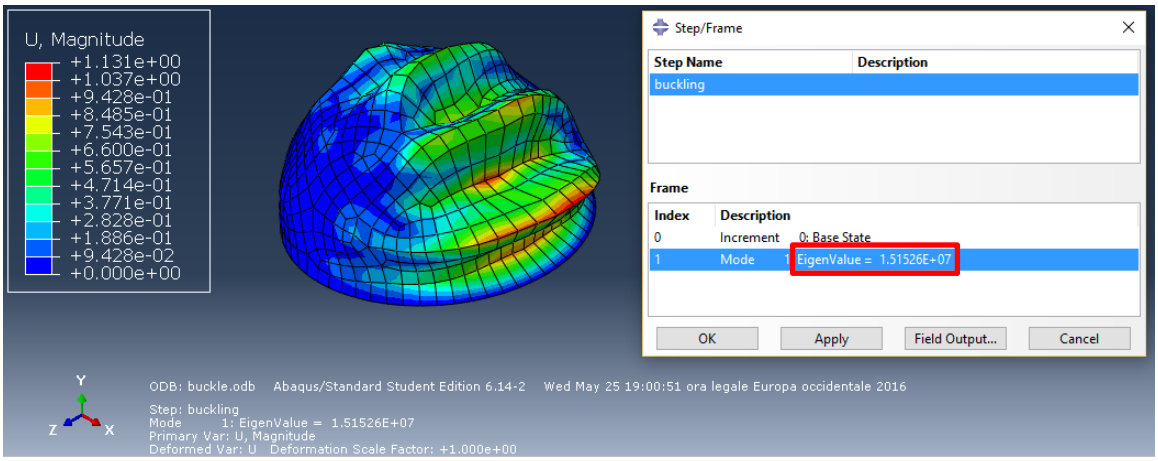

Figure 4.5. Illustration of the buckling P_{cr} of the hemispherical concrete dome

The analytical and the numerical solution are similar (Analytical solution: $P_{cr} = 1.47 \cdot 10^7$, Numerical solution: $P_{cr} = 1.51 \cdot 10^7$ Pa), therefore the numerical model is considered valid. Similar to previous analysis, an even greater level of accuracy it can be reached by increasing the refinement of the mesh, which in our case was limited by the student software version. In conclusion, the buckling load Pcr for the concrete hemispherical dome occurs for a higher value of the uniform external pressure compared to the mycelium dome.

4.2.6 Influence of the boundary conditions

The results of the buckling theory, as well as the ones obtained with the finite element software, are based on the assumption that the dome is pinned everywhere along its edge. We want now to investigate the effect of new boundary conditions, such as fixed supports. Since an analytical solution does not exist for other boundaries, the following results were obtained only by using the finite element software. For practical purposes, it has been analyzed only the hemispherical dome with the standard geometry under a uniform external pressure and under a uniform distributed load over a horizontal

projection of the dome surface. The comparison between the supported and the fixed conditions is shown in Table 4.6.

Table 4.7. Comparison for the critical buckling load P_{cr} and F_{cr} between pinned and fixed condition

CASE 1	CRITICAL BUCKLING LOAD P_{cr} (Pa)
	Numerical solution
Fixed condition	344.28
Pinned condition	338.08

CASE 2	CRITICAL BUCKLING LOAD F_{cr} (Pa)
	Numerical solution
Fixed condition	279.67
Pinned condition	214.17

As it can be seen, the values of the critical buckling loads P_{cr} and F_{cr} are higher for fixed conditions compared with the corresponding pinned configuration. This occurs because blocking rotations confers an overall greater stiffness and stability to the structure.

4.3 Case study

4.3.1 Dome with openings under uniform external pressure

The case study involves the buckling analysis of a hemispherical dome with openings under uniform external pressure and uniform distributed load over a horizontal projection of the dome surface. Opening are defined as voids in the matter of the surface of the considered elements. Depending on the function, openings can be divided in two main groups: doors and windows. Doors are usually rectangular, while windows can be either rectangular or circular. The buckling analysis was conducted on the hemispherical dome default geometry, with an angle of cut $\phi = 90°$, a radius r = 5m and a thickness t = 0.1. Regarding the openings, it has been considered a door of 1 x 2.5 m and 3 oculi of 0.4m of radius at a height of 2.1m place at 90°, 180° and 270° degrees from the door. The consideration of stiffeners around the openings was excluded from the analysis. As a

constraint, it has been decided to pin the dome along its edge. The material employed is concrete C25/30 with average properties already summarized in Table 3.6. The results obtained from the finite element analysis are shown in Fig 4.6 and 4.7

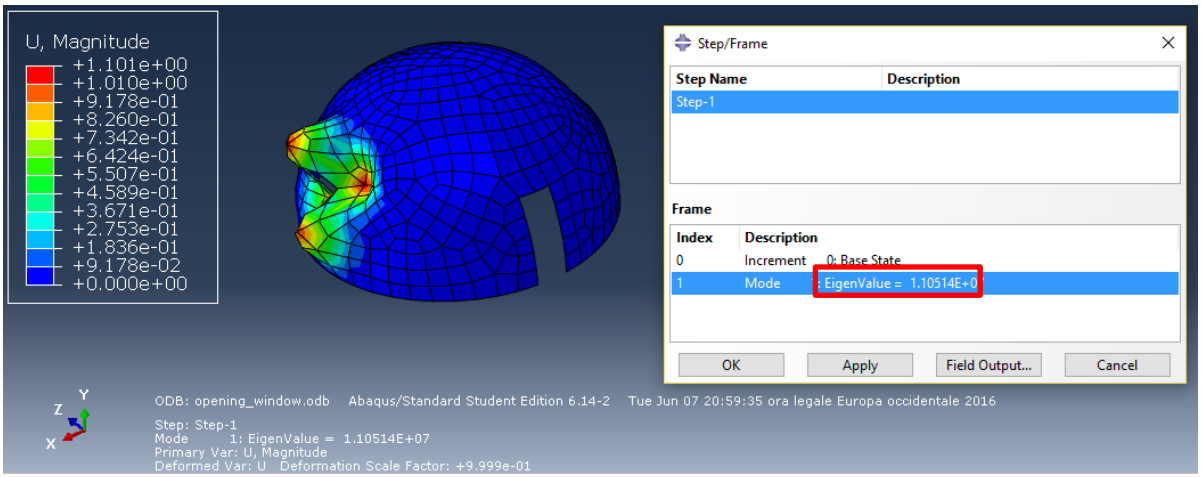

Figure 4.6. Illustration of the buckling P_{cr} of the hemispherical concrete dome with opening

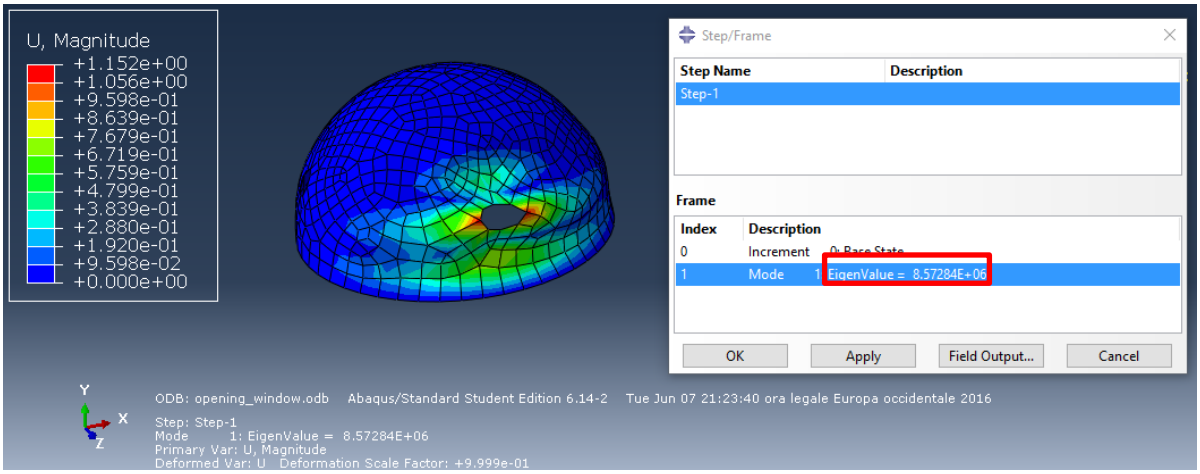

Figure 4.7 Illustration of the buckling F_{cr} of the hemispherical concrete dome with opening

The critical buckling P_{cr} and F_{cr} are respectively equal to $1.11 \cdot 10^7$ Pa and $8.57 \cdot 10^6$ Pa. These values are lower respect to the ones obtained for the same hemispherical dome without openings. In fact, introducing openings in a surface reduces the overall stability and stiffness of the structure. Moreover, according to the buckling deformation, it seems that the greater instability is concentrated on openings such as windows rather than doors.

Chapter 5: Form-Finding

5.1 Description of the principle and methods available

Shells represent one of the most efficient structural solutions in situations where a high level of structural performance is required, such as long spans and minimal material use. At the same time, shells possess a great aesthetic value mainly due to their light weight and graceful shape. In contrast with one dimensional curved structures, shells exploit the so-called “double arch effect”, which allows them to carry several different types of loads only by membrane actions. However, when they are not appropriately designed, the structural response can be compromised by their intrinsic weakness, such as a reduction in the buckling load in presence of small initial deformations or the occurrence of large inextensional deformations. Other structural issues can be caused by states of tension and bending. Therefore, shell design should involve shape as a key parameter, in order to reach a pure membrane stress state in compression and avoid structural issues such as buckling. The identification of appropriate shapes for shells is often called form-find. The general idea behind form-finding is to determine an equilibrium shape under a set of given conditions, such as the span, the type of boundaries, the selected material and/or the acting load. For conventional construction materials, such as concrete, the self-weight is usually the one that contributes more to the load that needs to be sustained, therefore the form finding process is often based on it. Numerical form find techniques such as particle-spring system, force density, and dynamic relaxation [17] have been successfully applied for shell structures and other form-found systems such as grid shells where the shape is set by the level of internal prestress and boundary supports [19]. The form-finding process adopted in this research is based on the principle of Hooke’s law and its

inversion. A catenary is a particular case of a funicular curve obtained when a rope or a chain hangs under its own weight [17]. When a cable is carrying only vertical loads, for definition it is subjected to pure tension. The horizontal component H and the vertical component V of such tension can be respectively expressed as:

$$H = T \cos \lambda = \text{constant} \qquad \text{[Eq.5.1]}$$

$$V = T \sin \lambda = H \tan \lambda = H \frac{dy}{dx} \qquad \text{[Eq.5.2]}$$

Where:

T is tension in the cable

λ is the slope between the cable and the horizontal

Now, if the self-weight w is constant along the arc length s, then:

$$w = \frac{dV}{ds} = \frac{dx}{ds}\frac{dV}{dx} = \cos \lambda \frac{dV}{dx} = \frac{1}{\sqrt{1+tan^2 \lambda}}\frac{dV}{dx} = \frac{1}{\sqrt{1+\left(\frac{dy}{dx^2}\right)^2}} H \frac{d^2y}{dx^2} \qquad \text{[Eq.5.3]}$$

Integrating the previous expression:

$$\frac{dy}{dx} = \sinh\left(\frac{x}{c}\right) \quad \text{with } c = \frac{w}{H}$$

After a second integration:

$$\frac{y}{c} = \cosh\left(\frac{x}{c}\right) - 1 \qquad \text{[Eq.5.4]}$$

Where the first constant of integration has been neglected and the second one is chosen so that the curve goes through the origin. The arc length s can be simply related to the x and y direction by the following relation:

$$s = \int_0^x 1 + \left(\frac{dy}{dx^2}\right)^2 dx = c \sinh\left(\frac{x}{c}\right) \qquad \text{[Eq.5.5]}$$

An illustration of the process to obtain a segmental arch and a catenary arch is shown in Fig. 5.1.

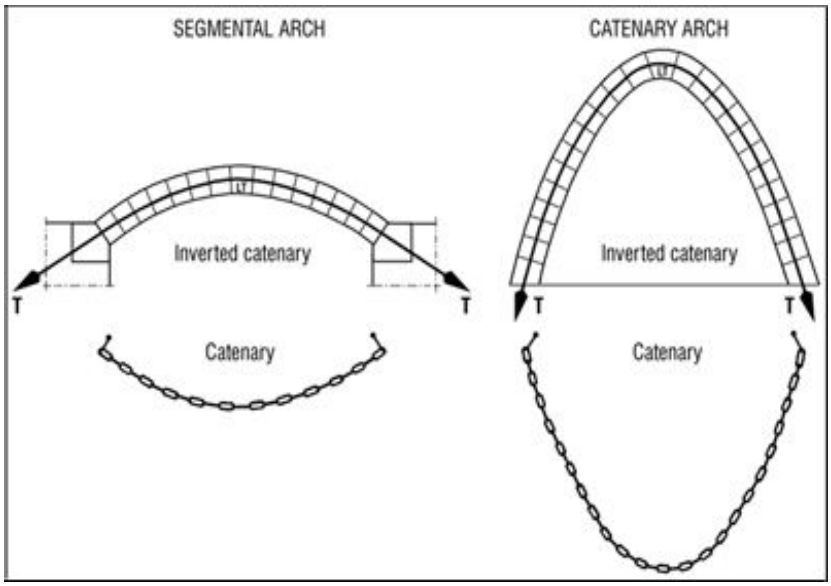

Figure 5.1. Illustration of how to obtain a segmental or a catenary arch [42]

Once the catenary has been obtained, inverting it upside-down, it passes from a state of pure tension to a state of pure compression. This principle of inverting the catenary was applied long time ago by the architect Govanni Poleni for San Peter in Rome. The equivalent 3D shape obtained by rotating the catenary around its axis is called “catenoid” and it will be analyzed further in this chapter.

5.2 Form-finding with Abaqus

The form-finding process has been conducted numerically with the finite element software, Abaqus. The principal aim of the process was to identify the geometry of a form-found shell comparable to the hemispherical dome and investigate which one has a better structural performance. The process started by drawing in Abaqus a circle with the same radius, thickness and material properties of the hemispherical dome of interest. Then, looking at the center of the circle, a gravity acceleration value which produces a vertical displacement at the center equal to the radius of the circle was applied. In terms of supports/constraint, the circle was considered pinned along its circumference.

According to the principle of the catenary, the obtained form-found shell is subjected to pure tension, that by rotating it 180° respect to the horizontal axis, transforms to pure compression. The form-found shell is then studied considering a linear static analysis and buckling analysis similar to those conducted in chapter 3 and 4. Considering the paradigm of the hemispherical mycelium-based dome with a radius a = 5m and a thickness t = 0.1m, the main steps that produced the corresponding form-found shape are shown here below in Fig. 5.2 - 5.4.

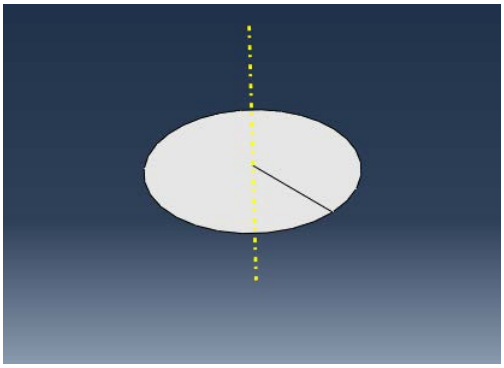

Figure 5.2. Illustration of the initial circle

The value of the acceleration of gravity that generated a vertical displacement of the center approximately equal to 5 m was found to be 0.58 $\frac{m}{s^2}$.

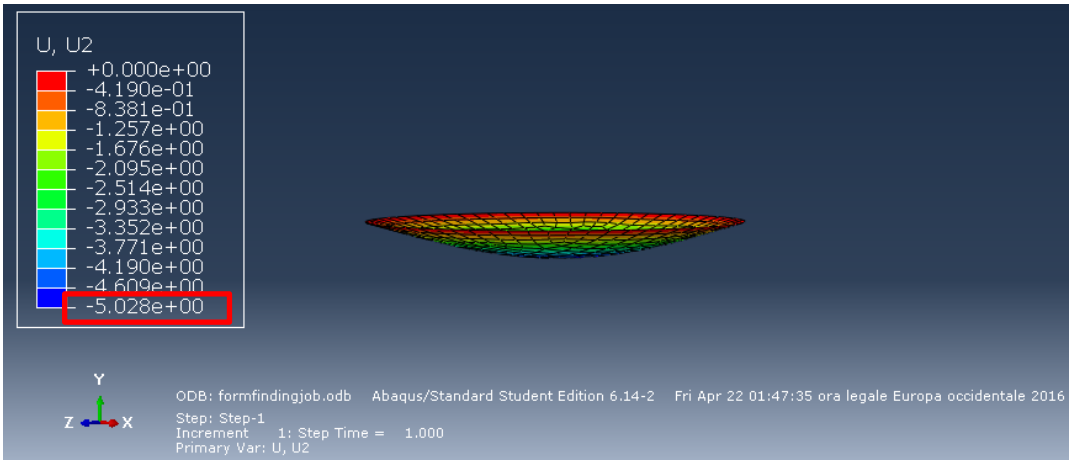

Figure 5.3. Illustration of the deformed circle subjected to a gravity acceleration of 0.58 $\frac{m}{s^2}$.

(The deformation is not in scale)

The structure is then rotated and its geometry is extracted and re-imported in Abaqus resulting in the following form-found shape, a catenoid:

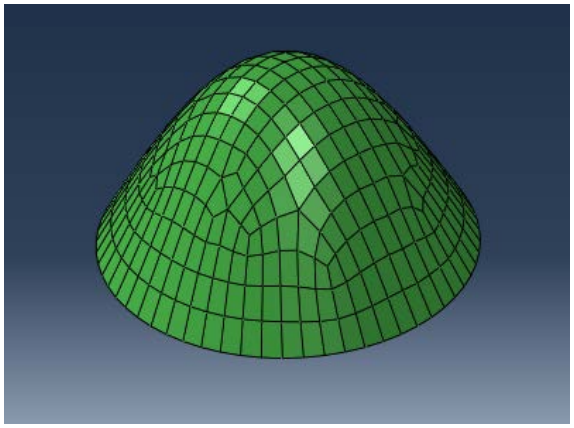

Figure 5.4. Illustration of the form-found shape

The influence of the type of loading, the geometry, the material properties and the boundary conditions is presented in the following sections. In order to isolate the single contributes, each case reflects the variation of a single parameter while keeping the others constant.

5.3 Assumptions

The aim of this chapter is to analyze numerically and compared the performance of the form-found shell with the corresponding hemisphere. Moreover the influence of using different geometries, types of loading and material properties is analyzed. Furthermore, similar to the linear analysis conducted in chapter 3, a constant thickness along the dome surface in each situation is assumed. Both for linear and buckling analysis pinned supported conditions are also considered. Moreover, only the first buckling mode (which is the one that corresponds to the minimum amount of energy), is of interest selecting the option to compute the first eigenvalue solely. The material employed is mycelium with the same properties as stated in Table 2.1.

5.4 Linear Analysis

5.4.1 Influence of the type of loading

This section focuses on the application of different types of loading. Since analytical formulations do not exist for any type of load, all the results were obtained numerically. Similarly to chapter 3, the following load cases have been considered:

- Case 1: Uniform load over the dome surface: p = self-weight
- Case 2: Uniform load over a horizontal projection of the dome surface: p= 500 Pa
- Case 3: Uniform external pressure over the dome surface: p = 1000 Pa

Case 1: Uniform load over the dome surface: p = self-weight

The linear analysis of the form-found shell was conducted similarly to chapter 3, obtaining the results shown in Fig. 5.5 and 5.6:

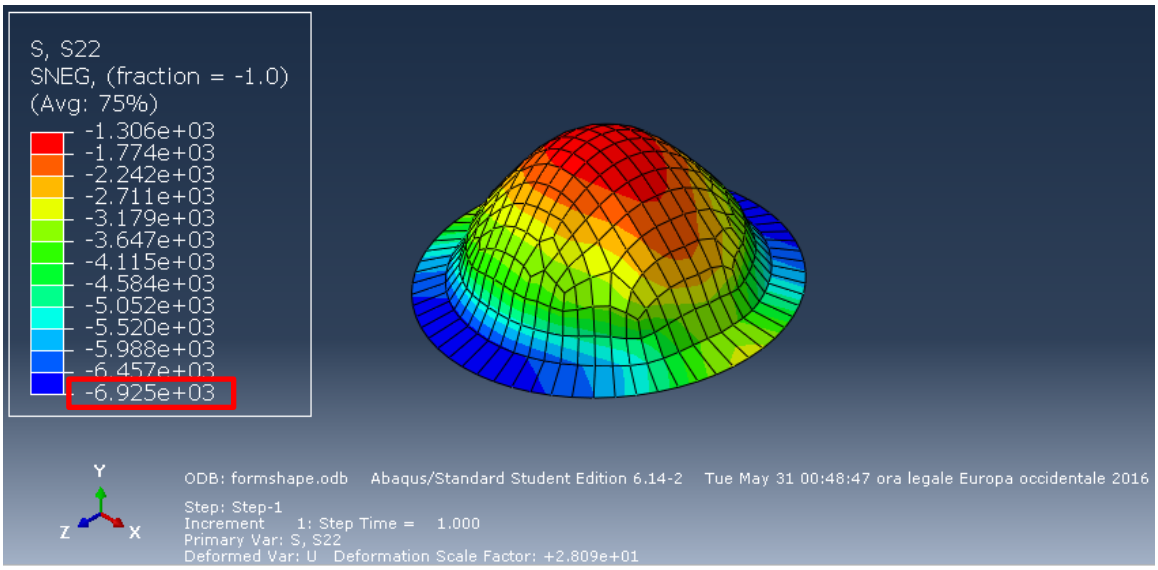

Figure 5.5. Illustration of the meridional stresses

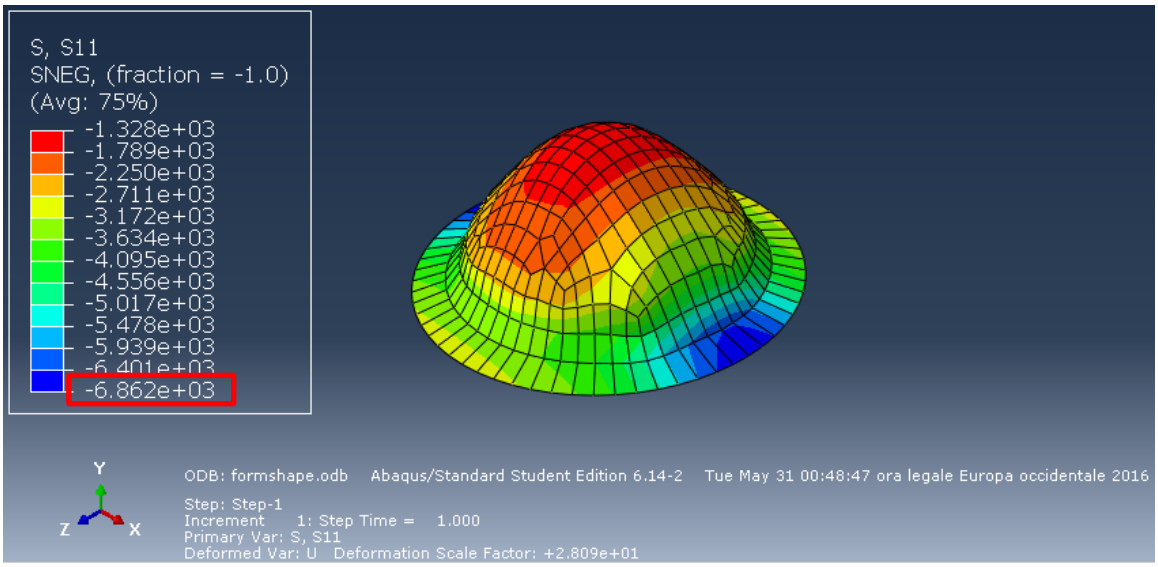

Figure 5.6. Illustration of the hoop stresses

Both meridional and hoop stresses on the form-found shell are in pure compression along the form-found surface, confirming the form-finding process. Considering Mohr's failure criterion: $\left|\frac{\sigma_\Phi}{\sigma_c}\right| + \left|\frac{\sigma_\theta}{\sigma_t}\right| < 1 \rightarrow \left|\frac{-6925}{-55000}\right| = 0.13 < 1$

Therefore it can be affirmed that, according to the linear analysis, the material strength is higher than the stresses sustained by the structure when it is subjected to its own weight.

A numerical comparison in terms of stresses between the form-found and hemispherical dome is shown in Table 5.1.

Table 5.1: Comparison between form-found and hemispherical dome in terms distribution of stress

CASE 1	UNIFORM LOAD OVER THE DOME SURFACE		
	σ_Φ (Pa)	σ_θ (Pa)	**Mohr's criterion**
Form-found dome	-6925	-6820	0.13
Hemispherical dome	-6110	6294	0.47

The form-found dome is subjected to a compression which is higher respect to the hemispherical dome.

However, it has to be considered safer by Mohr's failure criterion, because tension never occurs in the form-found surface.

Case 2: Uniform load over a Horizontal Projection of the Dome Surface: p = 500 Pa

The linear analysis of the form-found shell was conducted similarly to chapter 3, obtaining the results shown in Fig. 5.7 and 5.8:

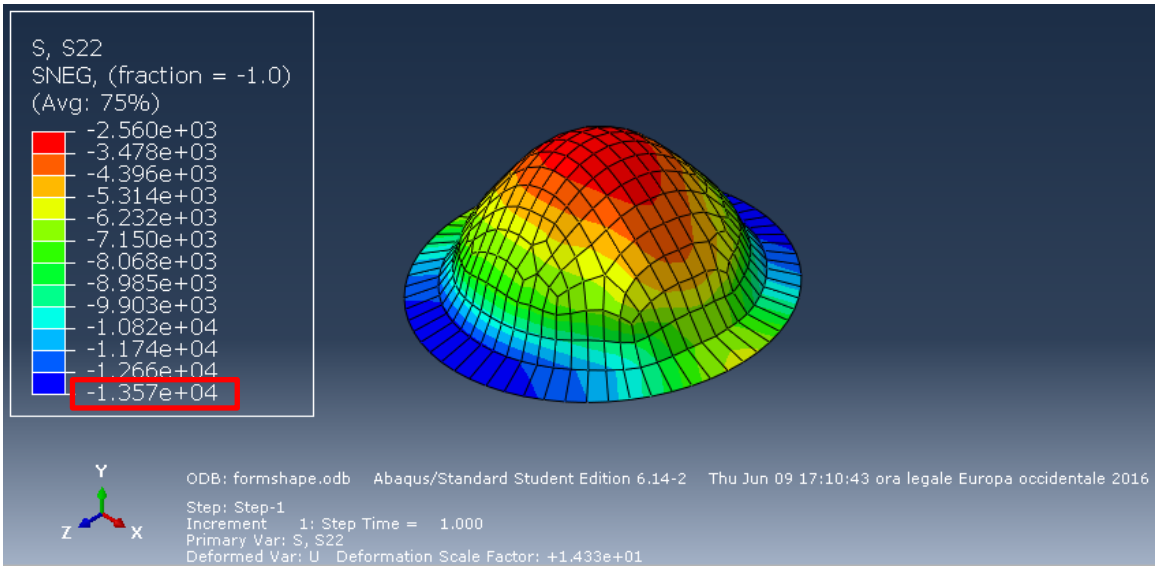

Figure 5.7. Illustration of the meridional stresses

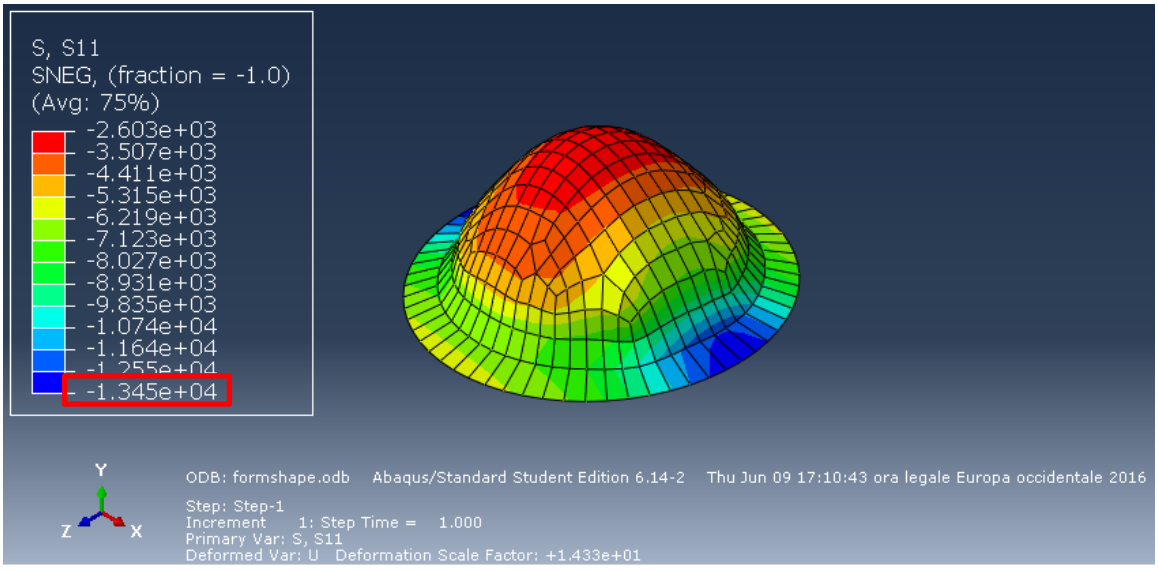

Figure 5.8. Illustration of the hoop stresses

Both meridional and hoop stresses are in pure compression along the form-found surface. In fact, the nature of the type of loading (Case 2) is similar to the previous one (Case 1). This becomes evident when comparing the distributions of stresses. Thus, having pure compression all along the form-found dome is valid result. Considering the Mohr's failure criterion:

$$\left|\frac{\sigma_{\Phi}}{\sigma_c}\right| + \left|\frac{\sigma_{\theta}}{\sigma_t}\right| < 1 \rightarrow \left|\frac{-13570}{-55000}\right| = 0.25 < 1$$

Therefore, the form-found dome is able to carry a uniform load over the horizontal projection of the dome surface p = 500 Pa. A numerical comparison in terms of stresses between the form-found and hemispherical dome is shown in Table 5.2.

Table 5.2. Comparison between form-found and hemispherical dome in terms distribution of stress

CASE 2	UNIFORM LOAD OVER AN HORIZONTAL PROJECTION OF THE DOME SURFACE		
	σ_{Φ} (Pa)	σ_{θ} (Pa)	**Mohr's criterion**
Form-found dome	-13570	-13450	0.25
Hemispherical dome	-11980	12340	0.94

The form-found dome is subjected to compression which is higher respect to the hemispherical dome. However, it has to be considered safer by Mohr's failure criterion, because tension never occurs in the form-found configuration.

Case 3: Uniform external pressure over the dome surface: p = 1000 Pa

The linear analysis of the form-found shell was conducted similarly to chapter 3, obtaining the results shown in Fig. 5.9 and 5.10:

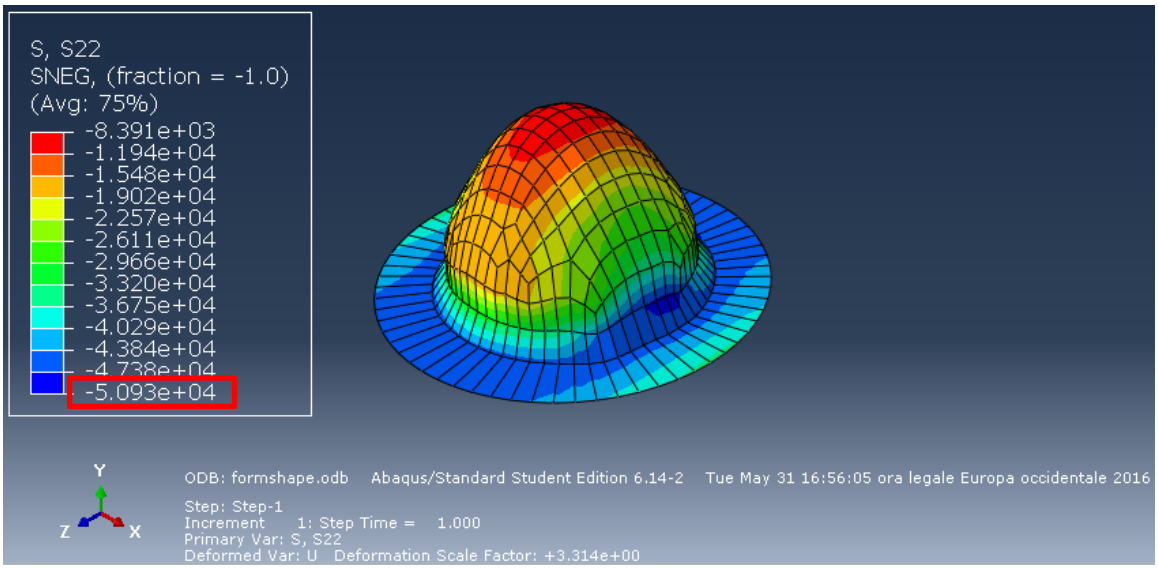

Figure 5.9. Illustration of the meridional stresses

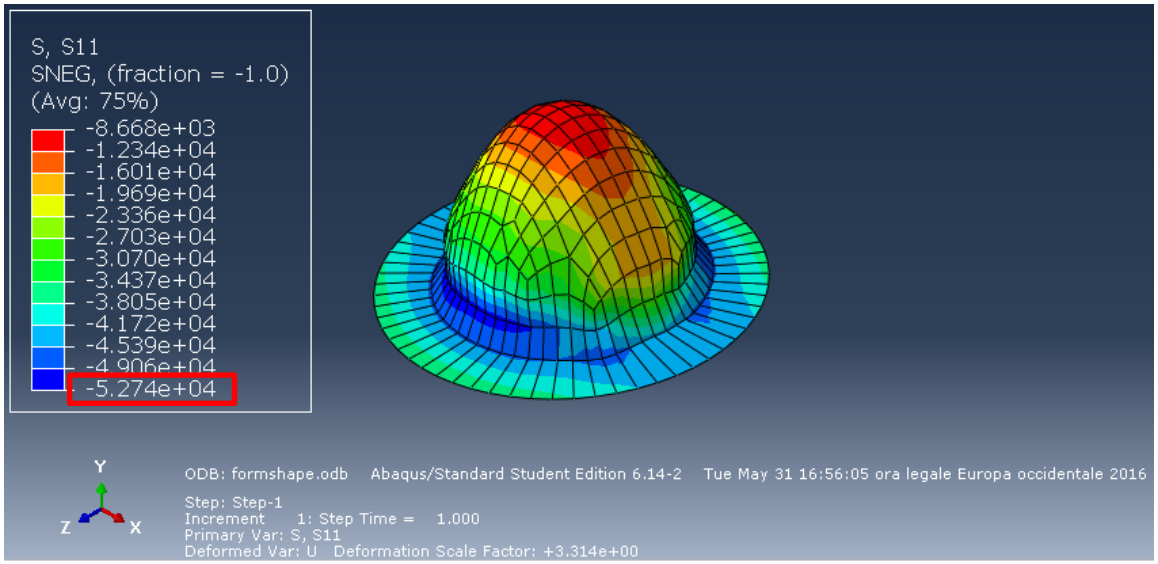

Figure 5.10. Illustration of the hoop stresses

Similar to the other cases, both meridional and hoop stresses are in pure compression along the form-found surface. This fact is quite obvious because the uniform external pressure is perpendicular in each point to the dome surface, therefore it induces a state of compression everywhere. The same situation was observed in chapter 3 for the hemispherical dome. Considering the Mohr's failure criterion:

$$\left|\frac{\sigma_{\Phi}}{\sigma_c}\right| + \left|\frac{\sigma_{\theta}}{\sigma_t}\right| < 1 \rightarrow \left|\frac{-52740}{\sigma_c}\right| < 1$$

Therefore it can be affirmed that, according to the linear analysis, the material strength is higher than the stresses sustained by the structure when it is subjected to a uniform load over a horizontal projection of the dome surface. A numerical comparison in terms of stresses between the form-found and hemispherical dome is shown in Table 5.3.

Table 5.3. Comparison between form-found and hemispherical dome in terms distribution of stress

CASE 3	UNIFORM EXTERNAL PRESSURE		
	σ_{Φ} (Pa)	σ_{θ} (Pa)	**Mohr's criterion**
Form-found dome	-50930	-52740	0.96
Hemispherical dome	-24930	-25060	0.46

The two principal stress states are pure compression and in particular they are greater for the form-found shell. Hence, the hemispherical dome can better sustain a uniform external pressure. In conclusion, considering this first set of comparisons, it can be affirmed that form-found dome has a more optimal shape to carry vertical loads, such as the uniform load over the dome surface and uniform distributed load over a horizontal projection of the dome surface. Contrary, the hemispherical dome minimizes the principal stresses under the uniform external pressure. However, these first linear analyses do not exclude the possibility of other type of failure, such as buckling.

5.4.2 Influence of the geometry

This section investigates the influence of varying the geometry in a form-found dome. Therefore, different values of the thickness, radius and height are considered. Differently to chapter 3, the variation of the angle of cut was neglected because in the context of form-finding it is not applicable. Since for the form-found dome a solution can solely be obtained numerically, only the uniform load over the dome surface is considered as loading for the following set of form-found dome models. All the geometrical variations respect to the original configuration are shown in Table 5.4.

Table 5.4. Variation of the geometrical parameters for the form-found dome

DIFFERENT VALUE OF THE THICKNESS			
Case	**t (m)**	**a (m)**	**h (m)**
A	**0,05**	5	5
B	**0,2**	5	5
C	**0,4**	5	5

DIFFERENT VALUE OF RADIUS AND HEIGHT			
Case	**t (m)**	**a (m)**	**h (m)**
D	0,1	**2,5**	**2,5**
E	0,1	**10**	**10**
F	0,1	**15**	**15**

The linear analysis of the form-found domes was conducted similarly to chapter 3, obtaining the results shown in Table 5.5.

Table 5.5. Results of linear analysis for different geometries of form-found domes

DIFFERENT VALUE OF THE THICKNESS	UNIFORM LOAD OVER THE DOME SURFACE		
	σ_Φ (Pa)	**σ_Φ** (Pa)	**Mohr's criterion**
CASE A	-6955	-6839	0.13
CASE B	-6822	-6786	0.12
CASE C	-6743	-6681	0.12

DIFFERENT VALUE OF THE RADIUS AND HEIGHT	UNIFORM LOAD OVER THE DOME SURFACE		
	σ_Φ (Pa)	**σ_Φ** (Pa)	**Mohr's criterion**
CASE D	-3409	-3391	0.06
CASE E	-14060	-14000	0.26
CASE F	-20760	-20300	0.38

According to the results, it can be affirmed that all the new geometries of the form-found dome can carry their self-weight. Moreover, the variations of the thickness and the radius in the form-found dome show similar with the hemispherical domes. Therefore, the

considerations made for the hemispherical dome remain valid also for the form-found dome.

5.4.3 Influence of the material properties

This section introduces material considerations involving the use of a different material, in particular concrete. The concrete employed belongs to C25/30 class with average properties already summarized in Table 3.6. Only the uniform load over the dome surface is considered as an acting load. The linear analysis of the form-found domes was conducted numerically as in chapter 3, obtaining the results shown in Table 5.5.

Table 5.6. Results of linear analysis for different geometries of form-found domes

CASE G	UNIFORM LOAD OVER THE DOME SURFACE		
	σ_Φ (Pa)	σ_θ (Pa)	**Mohr's Criterion**
concrete	- 135700	-137000	0.01
mycelium	-50930	-52740	0.96

As it was expected, both meridional and hoop stresses are in pure compression along the form-found surface and they are higher respect to the form-found dome made of mycelium. Considering the Mohr's failure criterion:

$$\left|\frac{\sigma_\Phi}{\sigma_c}\right| + \left|\frac{\sigma_\theta}{\sigma_t}\right| < 1 \rightarrow \left|\frac{135700}{25000000}\right| = 0.01 < 1$$

Therefore it can be affirmed that, according to the linear analysis, the material strength is higher than the stresses sustained by the structure. Although the concrete dome experiences larger stresses compared to the mycelium dome, stresses always remain lower to the ultimate strength of the material as expressed by the Mohr s criterion.

5.4.4 Influence of the boundary conditions

This section focuses on the consideration of a different boundary condition. For practical purposes, fixed boundary conditions were considered only for the default geometry of the form-found dome subjected to the three load cases. A comparison between the simply supported and the fixed conditions is shown in Table 5.7.

Table 5.7. Comparison between fixed and pinned supports for form-found domes in linear analysis

CASE 1	UNIFORM LOAD OVER THE DOME SURFACE		
	σ_Φ (Pa)	σ_θ (Pa)	**Mohr's Criterion**
Fixed condition	-5993	-5651	0.11
Pinned condition	-6925	-6862	0.13

CASE 2	UNIFORM LOAD OVER AN HORIZONTAL PROJECTION OF THE DOME SURFACE		
	σ_Φ (Pa)	σ_θ (Pa)	**Mohr's Criterion**
Fixed condition	-23500	-22160	0.43
Pinned condition	-27150	-26900	0.49

CASE 3	UNIFORM EXTERNAL PRESSURE		
	σ_Φ (Pa)	σ_θ (Pa)	**Mohr's Criterion**
Fixed condition	-54060	-54710	0.99
Pinned condition	-50930	-52740	0.96

According to Table 5.7, the distribution of the stresses changes when fixed supports are considered. However, the maximum stresses are lower in Cases 1 and 2 and higher in Case 3 compared with their corresponding pinned configurations.

5.5 Buckling analysis

5.5.1 Influence of the type of loading

This section investigates buckling under the different types of loading. Since analytical formulations do not exist for any type of loads, all the results were obtained numerically. Similar to chapter 4, the following load cases have been considered:

- Case 1: Uniform external pressure over the dome surface
- Case 2: Uniform load over a horizontal projection of the dome surface

The uniform load over the dome surface has been again excluded from this analysis.

Case 1: Uniform external pressure over the dome surface

The buckling analysis of the form-found dome was conducted numerically in the same methodology presented in chapter 4, obtaining the result shown in Fig. 5.11:

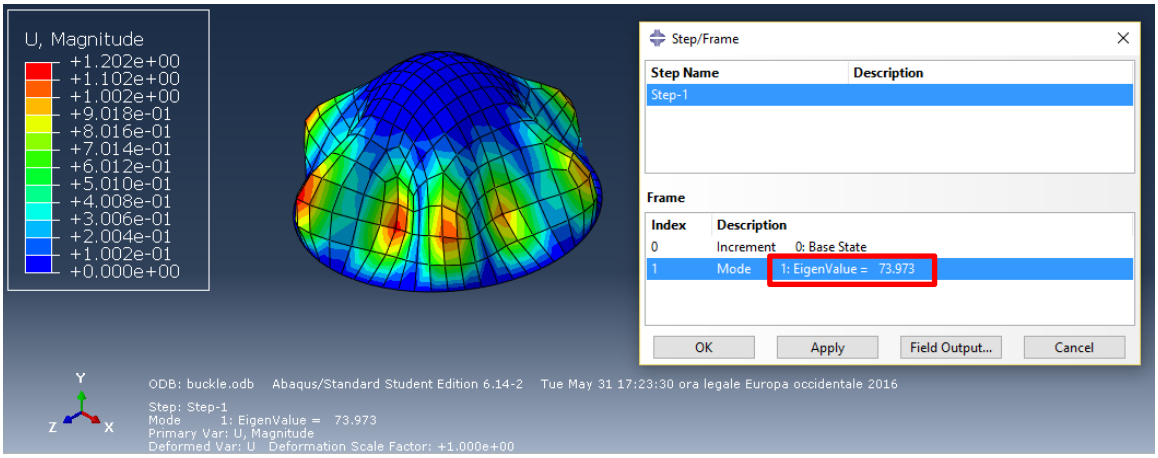

Figure 5.11. Illustration of the buckling load P_{cr} of form-found dome

Comparing the critical buckling load of the form-found dome with the corresponding load for the hemispherical dome (Table 5.8), it can be seen that the critical buckling load of the hemispherical dome occurs with a higher value.

Table 5.8. Comparison between form-found and hemispherical dome

CASE 1	CRITICAL BUCKLING LOAD P_{cr} (Pa)
	Numerical solution
Form-found dome	73.97
Hemispherical dome	338.08

Therefore, since also in the linear analysis the principal stresses experienced by hemispherical dome were lower respect to the form-found, it can be affirmed that the hemispherical dome can sustain better a uniform external pressure. In fact, a hemisphere

can be seen as the optimal form-found shape to carry this type of load. Moreover, since the value of the buckling load P_{cr} generated by the uniform external pressure is lower than the one used for the linear analysis (p = 1000 Pa), form-found dome is not able to sustain the prescribed uniform external pressure p = 1000 Pa employed in the linear analysis although the Mohr's criterion is satisfied.

Case 2: Uniform load over a Horizontal Projection of the Dome Surface

The buckling analysis of the form-found dome was conducted numerically in the same methodology presented in chapter 4, obtaining the result shown in Fig. 5.12:

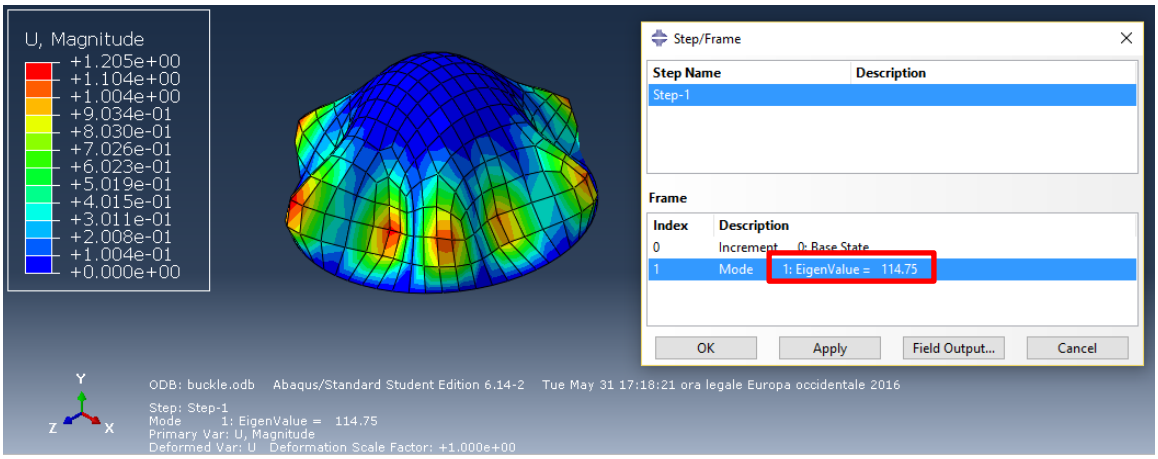

Figure 5.12. Illustration of the buckling load F_{cr} of form-found dome

Comparing the critical buckling load of the form-found dome with the corresponding load for the hemispherical dome (Table 5.9), it can be seen that the critical buckling load of the form-found dome occurs again with a lower value.

Table 5.9. Comparison between form-found and hemispherical dome

CASE 2	CRITICAL BUCKLING LOAD F_{cr} (Pa)
	Numerical solution
Form-found dome	114.75
Hemispherical dome	214.17

This result was unexpected because form-found showed lower stresses compared with the hemispherical dome subjected to the same type of load in linear analysis. However, a direct correlation between the linear and the buckling analysis does not exist. In fact, considering again the hemispherical dome under the uniform external pressure and comparing the analytical formulations of the stresses for linear and buckling analysis, the expressions for meridional, hoop and critical stresses are:

Linear analysis: $\sigma_\Phi = \frac{N'_\Phi}{t} = -\frac{a\,p}{2\,t}$ $\sigma_\theta = \frac{N'_\theta}{t} = -\frac{a\,p}{2\,t}$

Buckling analysis: $\sigma_{crit} = \frac{P_{cl}}{\frac{1}{2}S_{sphere}} = \frac{\frac{2}{\sqrt{[3\,(1-\nu^2)]}}E\,(\frac{t}{a})^2}{2\,\pi\,a^2}$

The formulations have a completely different grade and type of dependency on the geometrical parameters. In addition, the expressions of σ_Φ and σ_θ do not take into account the material properties of the dome. This example validates further that the linear and the buckling analysis are not directly related. Hence, when a form-found dome is subjected to a uniform load over a horizontal projection of the dome surface, it performs better in linear but worse in buckling analysis compared with a hemispherical dome. Since the value of the buckling load F_{cr} generated by the uniform load over an horizontal projection of the dome surface is lower than the one used for the linear analysis (p = 500 Pa), form-found dome is not able to sustain the prescribed uniform load over an horizontal projection of the dome surface p = 500 Pa employed in the linear analysis, although the Mohr's criterion is satisfied.

5.5.2 Influence of the geometry

This section investigates the influence of varying the geometry. Therefore, different values of the thickness, the radius and the height were considered individually. The variation of the angle of cut was once again neglected because in the context of form-finding it is not applicable. Instead, a parametrical study of the ratio between the radius and the height of the form-found dome is included. Uniform external pressure and uniform distributed load over a horizontal projection of the dome surface are also part of this analysis. In addition, for each case, it has been considered the ratio between the two correspondent critical buckling loads P_{cr} and F_{cr}, in order to see if a correlation between them exists also for the form-found dome. For the default geometry the ratio $\frac{Pcr}{Fcr}$ is equal to 0.64. All the geometrical variations respect to the original configuration are presented in the Table 5.10.

Table 5.10. Variation of the geometrical parameters for the form-found dome

DIFFERENT VALUE OF THE THICKNESS			
Case	**t (m)**	**a (m)**	**h (m)**
A	**0,05**	5	5
B	**0,2**	5	5
C	**0,4**	5	5
DIFFERENT VALUE OF RADIUS AND HEIGHT			
Case	**t (m)**	**a (m)**	**h (m)**
D	0,1	**2,5**	**2,5**
E	0,1	**10**	**10**
F	0,1	**15**	**15**

The linear analysis of the form-found domes was conducted numerically following the method described in chapter 4, obtaining the results summarized in Table 5.11.

Table 5.11. Ratio P_{cr}/F_{cr} for different geometries of form-found domes

Group 1	**P_{cr}** (Pa)	**F_{cr}** (Pa)	**Ratio**
CASE A	15.00	24.96	0.60
CASE B	374.09	543.91	0.69
CASE C	1976.30	2484.4	0.80

Group 2	**P_{cr}** (Pa)	**F_{cr}** (Pa)	**Ratio**
CASE D	374.80	543.98	0.69
CASE E	14.29	23.80	0.60
CASE F	5.98	10.30	0.58

The ratio between P_{cr} and F_{cr} increases with an increase of the thickness but decreases with the increase of the radius/height. Since the range of the thickness and the radius considered is limited (0.05m < t < 0.4m, 2.5 m < a/h < 15 m), additional values were also investigated to verify if the trends persist. Therefore, the following two cases were analyzed.

Table 5.12: Ratio P_{cr}/F_{cr} for two additional geometries of form-found domes

DIFFERENT GEOMETRIES						
Case	**t (m)**	**a (m)**	**h (m)**	**Pcr**	**Lcr**	**Ratio**
G	1	5	5	17837	17918	1,00
H	0,1	50	50	0,38	0,69	0,55

The ratio between P_{cr} and F_{cr} for the new geometries confirms the trends affirming that the correlation between P_{cr} and F_{cr} is not the same with the one found in chapter 4.

Moreover, the critical buckling loads P_{cr} and F_{cr} generated respectively by the uniform external pressure and the uniform load over an horizontal projection of the dome surface are in most cases lower than the values tested in the linear analysis (p = 1000 Pa and p =

500 Pa respectively). Therefore they represent an upper limit of the loads that the form-found domes can sustain.

5.5.3 Influence of the material properties

This section focuses on the influence of material properties with the use of a different material, in particular concrete. The concrete employed belongs to C25/30 class with average properties summarized in Table 3.6. Only the uniform external pressure has been considered as an acting load. The buckling analysis of the form-found domes has been conducted numerically similar to chapter 4, leading to the results shown in Fig. 5.15:

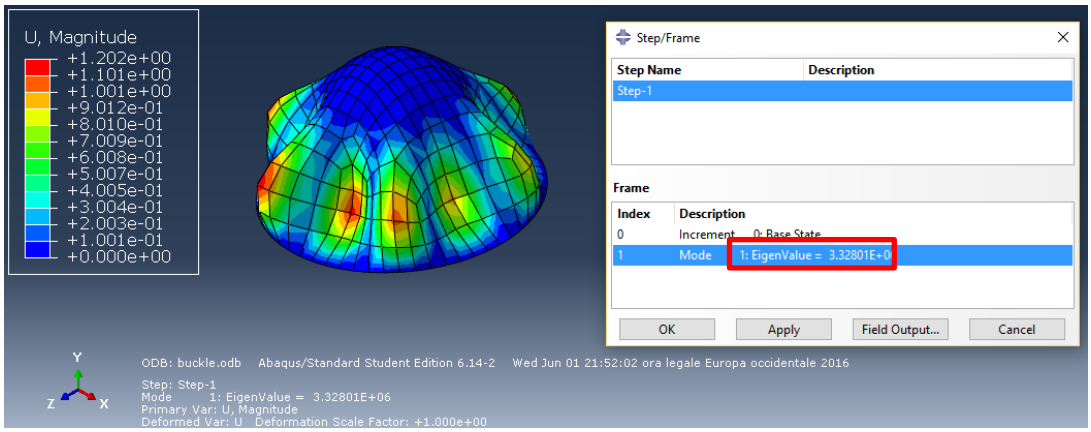

Figure 5.13. Illustration of the buckling load P_{cr} of concrete-based form-found dome

A comparison between the form-found dome made of concrete and the one made of mycelium is shown in Table 5.13.

Table 5.13. Comparison between concrete and mycelium in buckling analysis for form-found domes

CASE I	CRITICAL BUCKLING LOAD P_{cr} (Pa)
	Numerical solution
Concrete	$3.33 \cdot 10^6$
Mycelium	73.97

In conclusion, the buckling load P_{cr} for the concrete hemispherical dome occurs for a higher value of uniform external pressure compared to the mycelium dome.

5.5.4 Influence of the boundary conditions

This section involves the consideration of a different boundary condition. For practical purposes, fixed boundary conditions were considered only for the configuration of Case 1, where the type of loading is the uniform external pressure, the material employed is mycelium and the default geometry employed. A comparison between the pinned and the fixed supports is shown in Table 5.14.

Table 5.14. Comparison between fixed and pinned supports for form-found domes in linear analysis

CASE 1	CRITICAL BUCKLING LOAD P_{cr} (Pa)
	Numerical solution
Fixed condition	83.73
Pinned condition	73.97

CASE 2	CRITICAL BUCKLING LOAD F_{cr} (Pa)
	Numerical solution
Fixed condition	137.97
Pinned condition	114.75

The values of the critical buckling loads P_{cr} and F_{cr} are higher for fixed conditions compared with the corresponding pinned configuration. This occurs because blocking rotations confers an overall greater stiffness and stability to the structure.

5.5.5 Trend of the critical buckling load varying the height

In this section, the existence of an optimal ratio between the height and the span of the form-found dome when it is subjected to a uniform external pressure or a uniform load over a horizontal projection of the dome surface is investigated. For practical purposes only the following values of height/span ratio were considered (Table 5.15):

Table 5.15. Different values of the height/span ratio and the associate buckling load P_{cr} and F_{cr}

CASE	a (m)	h (m)	Ratio = h/2a	P_{cr} (Pa)	F_{cr} (Pa)
A	5	2.5	0.25	69.05	81.86
B	5	5	0.50	73.97	114.75
C	5	7.5	0.75	61.50	118.91
D	5	10	1.00	50.96	116.63
E	5	15	1.50	37.41	104.40

Figure 5.16 shows the optimal ratio between the height and the span exists in both cases and it depends on the type of load:

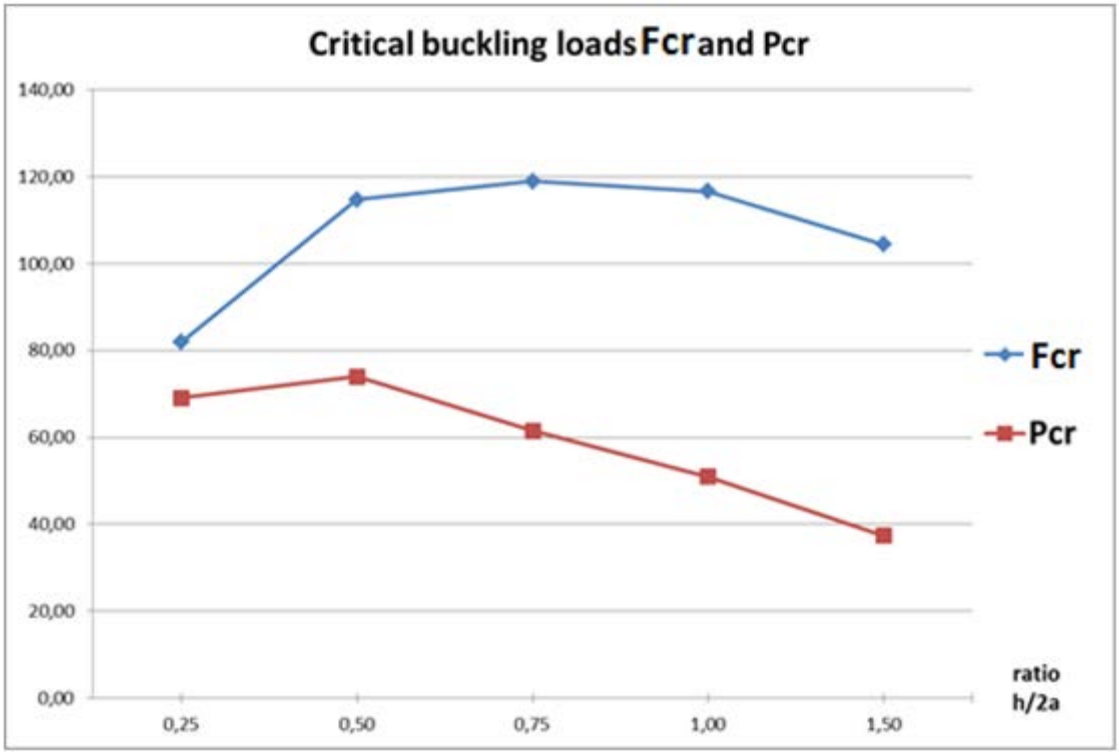

Figure 5.14. Trends of the buckling load P_{cr} and F_{cr} varying the height/span ratio

For P_{cr} the optimal ratio is 0.5, or rather the height is equal to the radius. For this value of the height/span ratio the form-found dome is geometrically similar to the hemispherical dome (radius equal to height), which is the optimal shape to resist a uniform external pressure. Therefore, the more the form-found dome is geometrically different from a

hemisphere, the more the critical buckling load P_{cr} decreases. For F_{cr} instead, the maximum buckling load occurs for a ratio of 0.75. Looking at the problem in two dimensions, a previous study conducted by Qaqish S. [24] on catenarian arches subjected to a uniform load along the arch axis revealed that the optimal ratio between the height and the span is equal to 0.3. Although buckling under a uniform load over the dome surface is out of the scope of this research, a parametric study of the height/span ratio for this load case is also conducted to investigate the correlation between the 2D and the 3D case. Calling Wcr the critical buckling load under a uniform load over the dome surface, the trend for different values of the height/span ratio is shown in Figure 5.17:

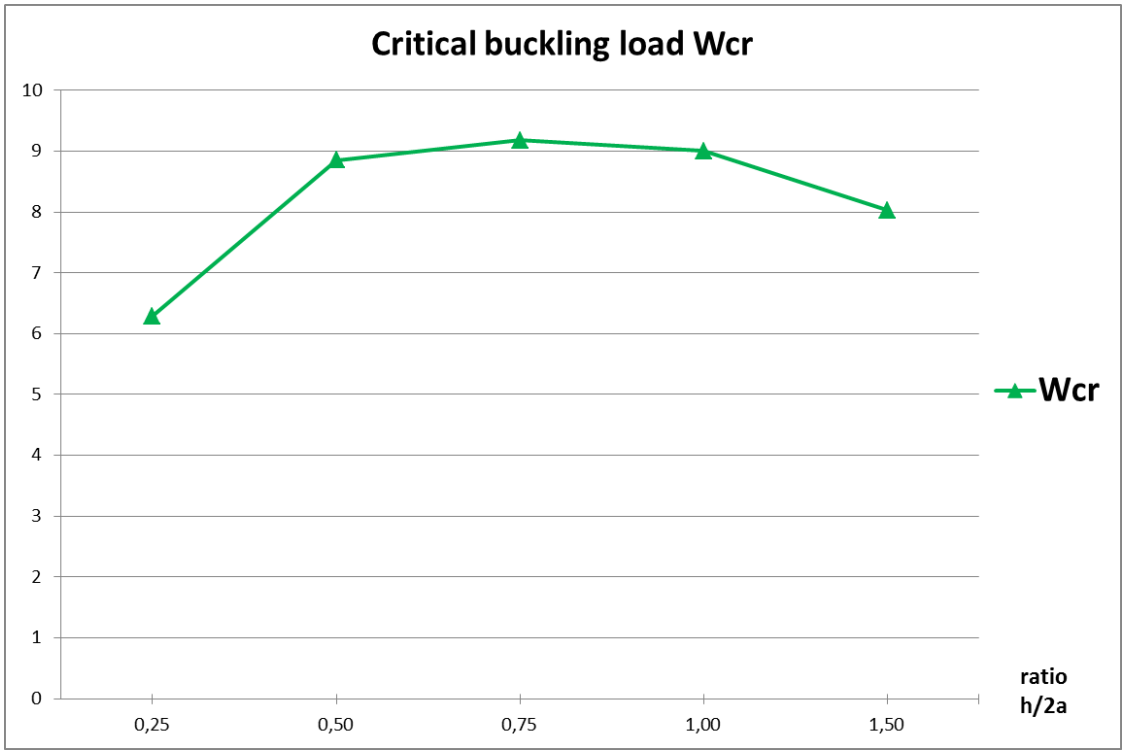

Figure 5.15. Trends of the buckling load Wcr varying the height/span ratio

The maximum buckling load W_{cr} occurs again for a height/span ratio equal to 0.75, the same value obtained for the buckling load F_{cr} under a uniform load over a horizontal projection of the dome surface. To further investigate the link between the 2D and the 3D

form-found structures, it was decided to perform similar buckling analysis on catenary arches subjected to these two load cases. This was done for two reasons: from one side to confirm the validity of the study mentioned before and on the other side to see if the height/span ratio that maximizes F_{cr} is again the same also for W_{cr}. Similarly to the previous analysis, a standard span equal to 10 m for each catenarian arch was considered, whereas the height of the dome varied. The results of the buckling analysis are shown in Fig. 5.18:

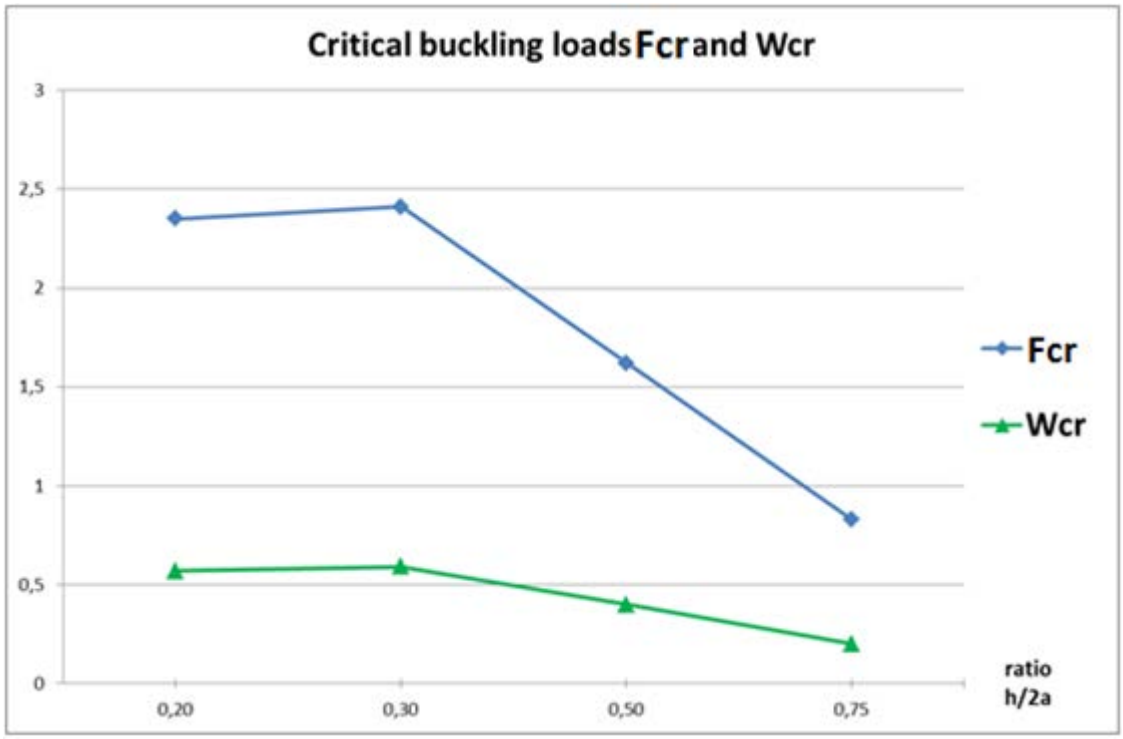

Figure 5.16. Trends of the buckling loads F_{cr} and W_{cr} varying the height/span ratio for catenary arches

Figure 5.16 shows that the optimal height/span ratio is again the same for the two load case (F_{cr} and W_{cr}) and it is equal to 0.3. Thus, this result confirms the validity of the previous study as well as the correlation in the trends between the two load cases.

Therefore, according with the numerical results of this study, the optimal height/span ratio passes from 0.3 for the planar case to 0.75 for the tridimensional one.

5.6 Case Study

5.6.1 Igloo

This case study focuses on the linear and the buckling analysis of an Igloo. Igloos are a type of shelter built of compacted snow. Their shapes vary from a hemisphere to a catenoid/paraboloid. Catenoid and paraboloid are two 3D surfaces respectively obtained by rotating of 180° a catenary and a parabola around their axis of symmetry. The linear analysis was conducted by comparing a paraboloid and a catenoid with the same thickness, height and span. A uniform load over the dome surface was considered as acting load. From a geometrical point of view, a radius a = 5m, a height h = 5m and a thickness t = 0.1m were assumed. The material employed is compacted snow/ice with the material properties summarized in Table 5.16.

Table 5.16. Material properties of compact snow/ice [42]

MATERIAL PROPERTIES OF ICE				
Density (Kg/m^3)	**Tensile Strength (KPa)**	**Elastic Modulus (MPa)**	**Compressive Strength (KPa)**	**Poisson Ratio**
430	N/A	9000	180	0.33

It is important to highlight that the values of the density and the compressive strength of ice strongly depend on the temperature. Therefore, a constant value for them does not exist. The distribution of the principal stresses for the catenoid igloo is shown in Fig. 5.19 and 5.20:

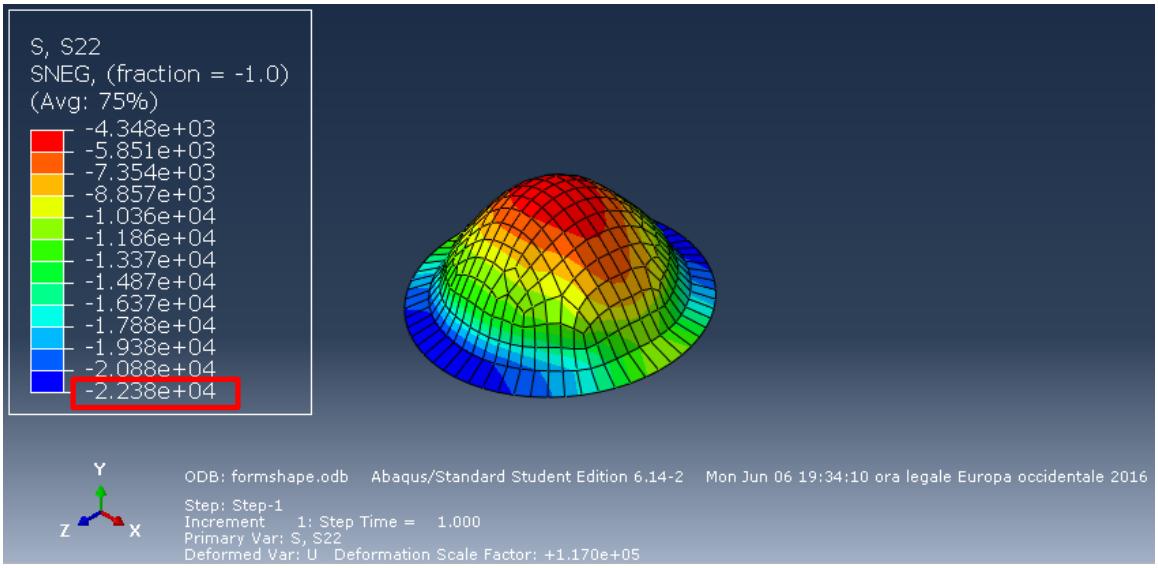

Figure 5.17. Illustration of the meridional stresses for catenoid igloo

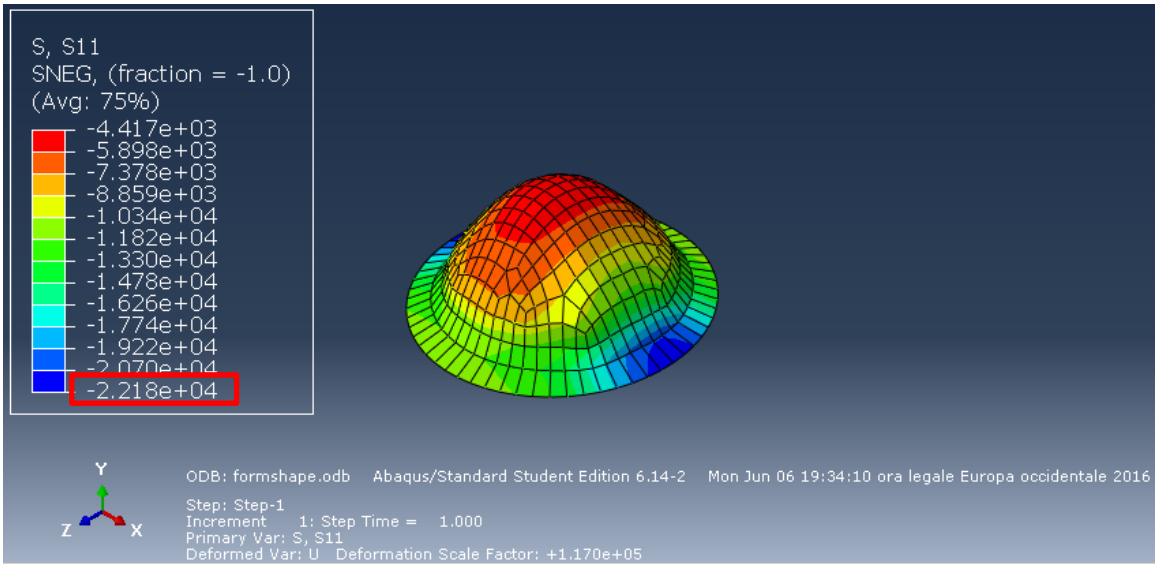

Figure 5.18. Illustration of the hoop stresses for catenoid igloo

As it was expected, the meridional and the hoop stresses are pure in compression for the catenoid. Considering the Mohr's failure criterion:

$$\left|\frac{\sigma_{\Phi}}{\sigma_c}\right| + \left|\frac{\sigma_{\theta}}{\sigma_t}\right| < 1 \rightarrow \left|\frac{22380}{180000}\right| = 0.12 < 1$$

Therefore it can be affirmed that, according to the linear analysis, the material strength is higher than the stresses sustained by the structure when it is subjected to its own weight.

The distribution of stresses for paraboloid igloo instead is shown in Fig. 5.21 and 5.22:

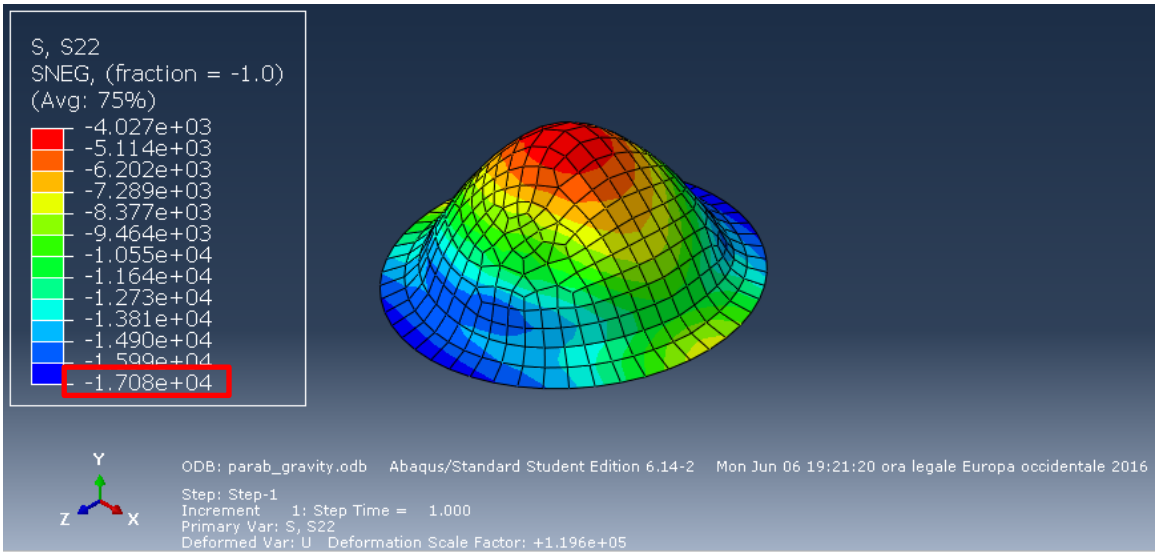

Figure 5.19. Illustration of the meridional stresses for paraboloid igloo

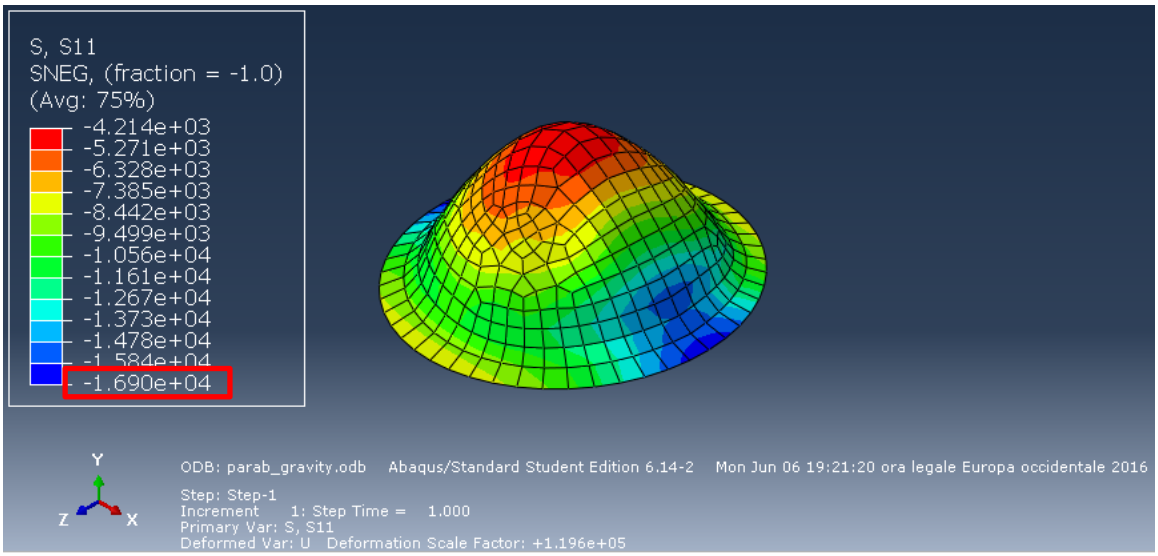

Figure 5.20. Illustration of the hoop stresses for paraboloid igloo

As it can be seen, the meridional and the hoop stresses are again pure compression also for the paraboloid. According to the Mohr's failure criterion:

$$\left|\frac{\sigma_{\Phi}}{\sigma_c}\right| + \left|\frac{\sigma_{\theta}}{\sigma_t}\right| < 1 \rightarrow \left|\frac{17080}{180000}\right| = 0.09 < 1$$

Therefore it can be affirmed that, according to the linear analysis, the material strength is higher than the stresses sustained by the structure when it is subjected to its own weight.

Table 5.17. Comparison between catenoid and parabloid for linear analysis

CASE 1	UNIFORM LOAD OVER THE DOME SURFACE		
	σ_{Φ} (Pa)	σ_{θ} (Pa)	**Mohr's Criterion**
Catenoid	-22380	-22180	0.12
Paraboloid	-17080	-16900	0.09

Comparing the two types of igloos one can observe that the distributions of the principal stresses are very similar, but higher for catenoid. This unexpected result might be due to the fact that form-finding process is conducted manually, influencing the overall accuracy of the response. For the buckling study, a uniform external pressure and a uniform load over a horizontal projection over the dome surface were considered. As shown in this chapter, the value of the height/span ratio that maximizes the critical buckling load P_{cr} under a uniform external pressure results to be 0.5, while for the critical buckling load F_{cr} under a uniform load over a horizontal projection of the dome surface is 0.75. Therefore, in the first case a radius a = 5m and a height h = 5m, whereas in the second one a radius a = 5m and a height h = 7.5 m were employed. Thickness and material properties remain always as before the same. The illustrations of buckling modes of the two types of igloo under uniform external pressure, respectively for catenoid and paraboloid, are shown in Fig. 5.23 and 5.24:

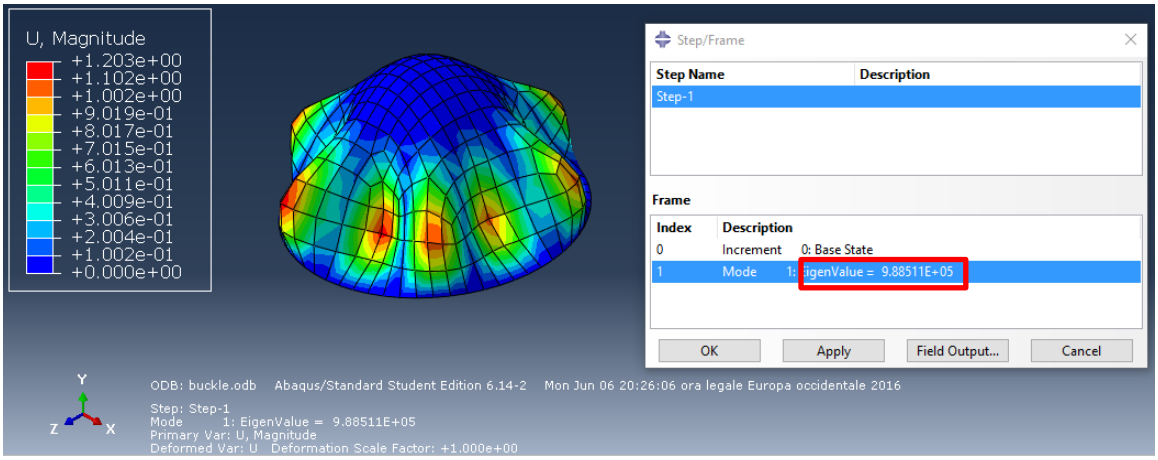

Figure 5.21. Illustration of the buckling load P_{cr} of catenoid igloo

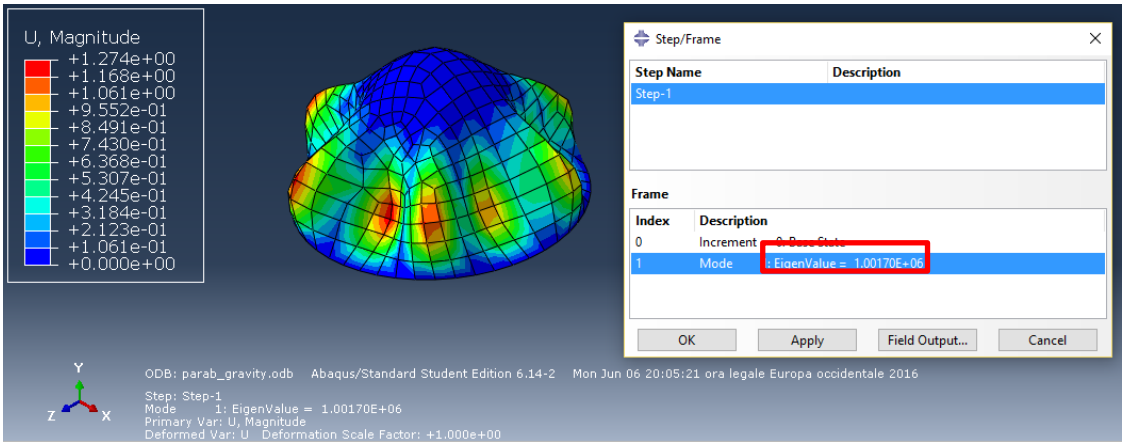

Figure 5.22. Illustration of the buckling load P_{cr} of paraboloid igloo

As it can be seen in Table 5.18, the two values of the buckling loads P_{cr} are very similar, at the point that the difference between them is around 1%.

Table 5.18. Comparison between catenoid and paraboloid for the critical buckling load P_{cr}

CASE 1	CRITICAL BUCKLING LOAD P_{cr} (Pa)
	Numerical solution
Catenoid	988511
Paraboloid	1001700

The illustrations of buckling modes of the two types of igloo under uniform distributed load over a horizontal projection of the dome surface, respectively for catenoid and paraboloid, are shown in Fig. 5.25 and 5.26:

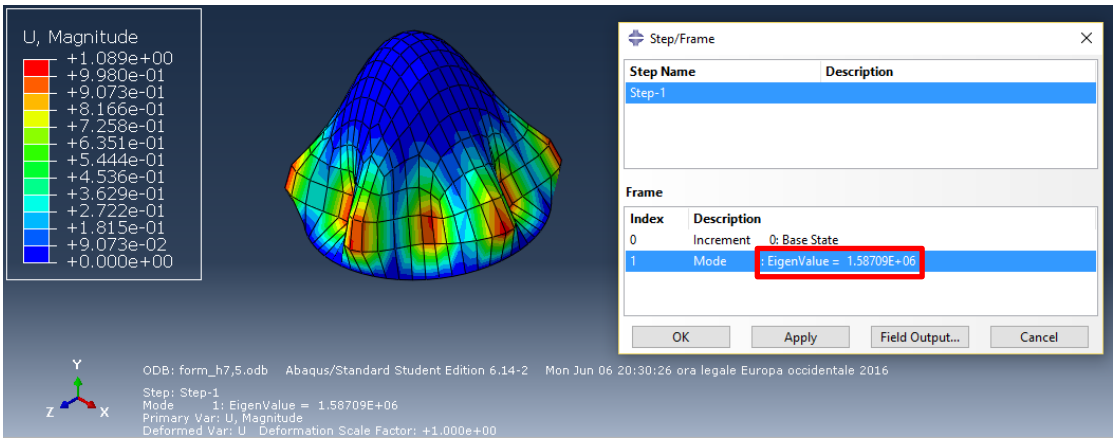

Figure 5.23. Illustration of the buckling load Fcr of catenoid igloo

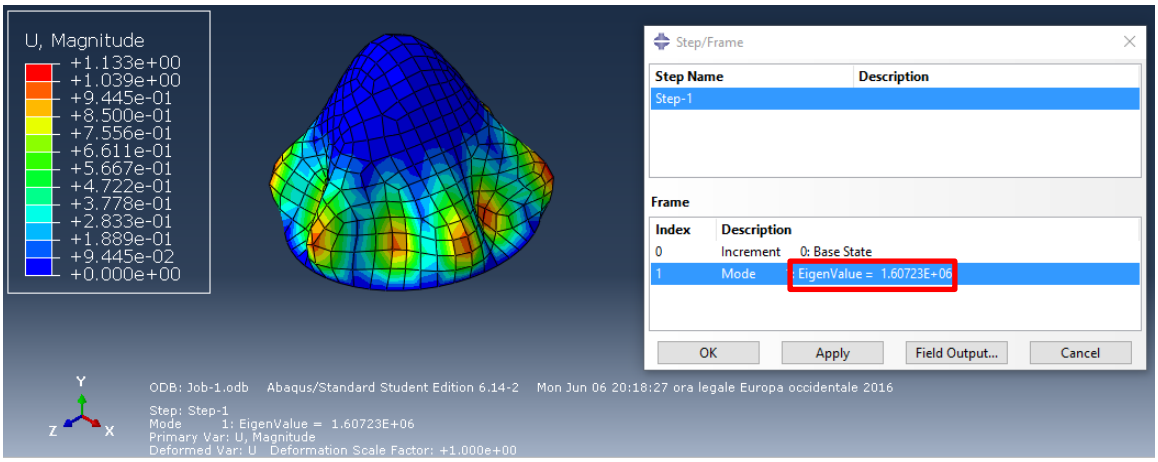

Figure 5.24. Illustration of the buckling load F_{cr} for paraboloid igloo

Also the vaue of the two buckling loads F_{cr} are very similar, with a difference between them again around the 1%.

Table 5.19. Comparison between catenoid and paraboloid for the critical buckling load F_{cr}

CASE 2	CRITICAL BUCKLING LOAD F_{cr} (Pa)
	Numerical solution
Catenoid	1587090
Paraboloid	1607230

As general conclusion, it can be affirmed that the linear static and buckling behaviors of a catenoid and a paraboloid are almost the same. The results have shown a higher discrepancy in linear analysis respect to buckling analysis.

Chapter 6: Conclusions

According to the analyses conducted in this study, it is evident that shells are characterized by a peculiar structural behavior which distinguishes them from other structural elements. The comparisons between analytical formulations and numerical studies using the finite element software confirm the validity of the classical shell theory, as well as the reliability of the finite element models. It can thus be concluded that mycological fungi can be employed as a constitutive material for domes. In fact, the stresses experienced in the dome structures analyzed never reached the ultimate strength of the material highlighting the importance of an appropriate shape. However, buckling analysis demonstrates that the use of mycelium as a constitutive material in domes results in weaker structures compared to concrete for this type of failure. Regarding the "form-finding" process, the numerical results obtained with the finite element validate the principle of Hooke's law and its inversion: all form-found domes are in pure compression when subjected to vertical loads. Although the form-found domes show better performance in linear elastic analysis compared with the hemispherical domes, the opposite trend is found when it comes to buckling. From a technical point of view, this study allows to draw the following conclusions:

- For hemispherical mycelium-based domes with a radius of curvature equal or greater than 10 m, the hoop stresses, which are in pure tension, exceed the ultimate tensile strength of the material. Therefore, for large scale structures, the use of reinforcement becomes necessary.

- For mycelium-based domes, increasing the thickness does not necessarily guarantee a better structural performance. In fact, the additional stiffness is

"balanced" by the additional self-weight that the structure has to sustain. A greater level of stiffness could be reached through other considerations such as changing the shape or adding reinforcement.

- Fixed boundary conditions produces a different distribution of the stresses with respect to the simply supported conditions. Furthermore, for hemispherical domes subjected to vertical loads, the maximum compression is higher for fixed supports, whereas the maximum tension is much lower, making the dome overall safer by Mohr's criterion compared to simply supported conditions. Conversely, for hemispherical domes subjected to uniform external pressure, both meridional and hoop stresses are higher for fixed boundary conditions, making the domes less safe by Mohr's criterion.

- The value of the critical buckling load P_{cr} generated by a uniform external pressure increases with the increasing of the angle of cut and the thickness, while it decreases with an increase of the span (radius).

- For hemispherical domes, the ratio between the buckling loads P_{cr} and F_{cr} (respectively generated by a uniform external pressure and a uniform load over a horizontal projection of the dome surface) seems to be always approximately equal to 1.5, as long as the geometrical parameters of the considered dome are the same. Therefore, it is assumed that the formulation of F_{cr} has the same degree of dependency of P_{cr}, especially looking at the slenderness ratio and the material properties.

- The critical buckling loads P_{cr} and F_{cr} are higher for fixed conditions respect to the pinned conditions. This result is due to the fact that blocking rotations confers an overall greater stiffness and stability to the structure.

- For domes with opening the values of the buckling loads P_{cr} and F_{cr} are lower than the ones obtained for domes without opening. Furthermore, according to the finite element model, the deformations due to buckling seem to concentrate more around windows rather than doors.

- Form-found domes perform better in linear analysis but worse in buckling analysis compared to hemispherical domes of comparable geometry when they are subjected to the same type of loads reflecting the fact that linear analysis and buckling analysis do not have the same degree of dependency on the geometrical parameters and material properties.

- Differently from hemispherical domes, for form-found domes a correlation between the buckling loads P_{cr} and F_{cr} (respectively generated by a uniform external pressure and a uniform load over a horizontal projection of the dome surface) was not found.

- According with the numerical results of this study, the optimal height/span ratio to resist the buckling load P_{cr} and F_{cr} passes from 0.3 for the planar case of catenarian arches to 0.75 for the tridimensional case of form-found domes.

- Paraboloids show better performance both in linear and buckling analysis compared to catenoids. However, looking at the order of magnitude, the mechanical responses are very similar.

Chapter 7: Future works

Although the results obtained through this study reflect the special character of shell structures as well as the potential of mycological fungi as a construction material, they also underline the need of further investigations. First of all, in order to have a deeper understanding of the structural behavior of domes, non-linear analyses need to be performed. In addition, the effect of imperfections as well as the edge effect have to be taken into consideration. Similarly, the buckling analysis, that was performed solely using finite element modeling, should also be extended considering non-linearity and imperfections as well as multiple buckling modes while being validated through experimental testing. Regarding the material, a deeper knowledge about the behavior of mycological fungi is also required. In particular, a life-cycle analysis and the long-term behavior (shrinkage, creep and cracking) need to be investigated. Last but not least, in order to clarify the performances of the material associated to the optimization of the shape (form-finding), future works should also involve experimental testing of near full scale structures.

References

(1) The Roman Pantheon http://www.crystalinks.com/romepantheon.html (accessed June 22, 2016).

(2) Tuscany people http://www.tuscanypeople.com (accessed June 22, 2016).

(3) Billington, D. P. *Thin shell concrete structure, McGraw Hill*, **1982**.

(4) A God Amongst Men and His Night of a Centur. http://pabook2.libraries.psu.edu/palitmap/Wilt100.html (accessed June 22, 2016).

(5) Costruire correttamente | Concorso nazionale per le scuole ispirato alla figura e all'opera di Pier Luigi Nervi http://costruirecorrettamente.org/site/chi-e-pier-luigi-nervi/index.php? doc_id=76 (accessed June 22, 2016).

(6) Museo Torino | Palazzo della Moda e Torino Esposizioni http://www.museotorino.it/view/s/9f3e93adabe8447e994c76c46ed3336a (accessed June 22, 2016).

(7) The History of Thin-Shells and Monolithic Domes http://www.monolithic.org/blogs/engineering/the-history-of-thin-shells-and-monolithic-domes/photos (accessed June 22, 2016).

(8) Timoshenko, S. Theory of plates and shells. *McGraw-Hill*, **1987**.

(9) Hauso, H. Analysis methods for thin concrete shells of revolution. *Norwegian university of science and technology*, **2014**.

(10) South, N. A Finite element analysis of the monolithic dome, *Idaho state university*, **2005**.

(11) Houston, R.; Josephs, H., Ch.31 Buckling of spherical shells, Practical stress analysis in engineering design, 3rd Edition, *Taylor and Francis Group* LLC, **2008**.

(12) Niezgodzinski, T.; Swiniarski, J. Numerical calculations of stability of spherical shells, *Mechanic and mechanical engineering Vol.14 No.2, Technical University of Lodz*, **2012**, 325-337.

(13) Mekjavic, I. Buckling analysis of concrete spherical shells, *ISSN 1330-3651, University of Zagreb*, **2011**, 633-639.

(14) Chang, Z.-T.; Bradford, M. A., Gilbert, R. I. Short-term behavior of shallow thin-walled concrete dome under uniform external pressure, *Thin-walled structures, Elsevier Ltd.*, **2011**, 112-120.

(15) Von Karman T, Tsien H-S. The buckling of spherical shells by external pressure. *Journal of Aeronautical Sciences*, **2008**, 1939:43–50.

(16) NASA SP-8032, Buckling of thin-walled doubly curved shells, *NASA MSFC library*, **1969**, 1-32.

(17) Adriaenssens, S.; Block, P.; Veenendaal, D.; Williams, C. Form finding and optimization of shell structures, *Taylor and Francis group*, **2014**.

(18) Isler, H. Concrete shells derived from experimental shapes, *Structural engineering international*, Vol.4, **1994**, 142-147.

(19) Adriaenssens, S.; Asce, M.; Ney, L., Bodarwe, E.; Williams C. Finding the form of an irregular meshed steel and glass shell based on construction constraints, *Journal of architectural engineering, ASCE*, **2012**, 206-213.

(20) Bletzinger, K.-U.; Ramm, E. Form finding of shells by structural optimization, *Engineering with computers*, **1993**, 9:27-35.

(21) Ramm, E.; Mehlhorn, G. On shape finding methods and ultimate load analyses of reinforced concrete shells, *178 Engineering structures*, Vol.13, **1991**, 178-198.

(22) Douthe, C.; Baverel, O.; Caron, J.-F. Form-finding of a grid shell in composite materials, *Journal of international association for shell and spatial structures: IASS, Vol.47 n.150*, **2006**.

(23) Tomàs, A.; Martì, P. Shape and size optimization of concrete shells, *Engineering structures Elsevier Ltd*, **2010**, 1650-1658.

(24) Qaqish, S. S. Buckling behavior of symmetric arches, *University microfilms international, University of Arizona*, **1977**.

(25) Kromoser, B.; Kollegger, J. Pneumatic forming of hardened concrete-building shells in the 21st century, *Ernst and Sohn, Structural concrete, No.2*, **2015**, 161-171.

(26) Sadid, H.; South, N. Finite element modeling of monolithic dome structures, *Engineering Structures and mechanics*, **2005**.

(27) Lanham, C. Keeping students safe: introducing the monolithic dome, *School business affair*, **2009**, 14-16.

(28) Travaglini, S.; Noble, J.; Ross, P.G.; Dharan, C.K.H. Mycology Matrix Composites Proceedings of the American Society for Composites, Twenty-Eighth Technical Conference, *ASC conference paper*, **2013**, 1-20.

(29) Carlile, M. J. The success of the hypha and mycelium: The growing fungus. *Springer Netherlands*, **1994**, 3-19.

(30) Gibson, L.J. and M.F. Ashby. Cellular Solids: Structure and Properties. 1st and 2nd ed. *Cambridge University Press*, **1999**.

(31) Home | We Grow Materials http://www.ecovativedesign.com (accessed June 22, 2016).

(32) Hi-Fi, The Organic Mushroom-Brick Tower Opens At MoMA's PS1 Courtyard http://www.archdaily.com/521266/hy-fi-the-organic-mushroom-brick-tower-opens-at-moma-s-ps1-courtyard (accessed June 22, 2016).

(33) Science4All | The Cubic Ball of the 2014 FIFA World Cup http://www.science4all.org/article/brazuca/ (accessed June 22, 2016).

(34) Efunda | Maximum Normal Stress Criterion http://www.efunda.com/formulae/solid_mechanics/failure_criteria/failure_criteria_brittle.cfm (accessed June 22, 2016).

(35) Logan, D. L. A first Course in the Finite Element Method, *Cengage learning, 5th edition*, **2012**.

(36) Carboni,F. Norme tecniche per le costruzioni, Module 3, Costruzioni di calcestruzzo, *Università politecnica delle Marche*.

(37) Iacobelli, F. Progetto e verifica delle costruzione in muratura in zona sismica, *EPC libri*, **2008**, 1-22.

(38) Wikipedia | Santuario della Madonna di San Luca https://it.wikipedia.org/wiki/Santuario_della_Madonna_di_San_Luca (accessed June 22, 2016).

(39) Soprintendenza del comune di Bologna.

(40) Studio associato Manfredi Casu, Progetto di messa in sicurezza e allestimento del percorso di salita e visita della cupola del santuario della natività di Maria "Regina Montis Regalis", *Architettura urbanistica design*, **2014**.

(41) Auroville | Earth Institute | Stability Notion | Basic Structural Principle http://www.earth-auroville.com/stability_notions_en.php (accessed June 22, 2016).

(42) Handy, R. L. The igloo and the natural bridge as ultimate structure, *Engineering research institute and civil engineering dept., Iowa state university*, **1973**, 276-281.

(43) Abaqus 6.12, Example Problems Manual, Volume I: Static and Dynamic Analyses, *Dassault Systemes*, **2012**.

(44) Mayoral Gonzàlez, E. Growing architecture through mycelium and agricultural waste, *AAR, Columbia University, GSAPP,* **2009**,1-28.

(45) Malek, S.; Wierzbicki, T.; Ochsendorf, J. Buckling of spherical cap gridshells: a numerical revisiting the concept of the equivalent continuum, *Engineering Structures, Elsevier Ltd.*,**2014**., 288-298.

(46) Ross, C. T. F.; Popken, D. Buckling of tube-stiffened prolate domes under external water pressure, *Thin walled structures, Elsevier Ltd.*, **1995**, 159-179.

(47) Bradshaw, R. R. Application of the general theory of shells, *Journal of the American concrete institute, No.58-5, **1961***, 129-148.

(48) Chilton, J.; Isler, H. Finding the form and proving its strength, *Ch. 2, The engineer's contribution to contemporary architecture: Heinz Isler, , ICE Publishing,* **2000**, 31-47.

(49) Siu, S.; Rhode-Barbarigos, L.; Wagner, S.; Adriansssens, S. Dynamic relaxation study and experimental verification of dielectric-elastomer minimum-energy structures, *AIP publishing LLC*, **2013**.

(50) Brinkmeyer, A.; Santer, M.; Pirrera, A.; Weaver, P.M. Pseudo-bistable self-actuated domes for morphing applications, *International journal of solids structures, Elsevier Ltd.*, **2012**, 1077-1087.

(51) Young, W. C.; Budynas, R. G. Roark's formulas for stress and strain, *7th Edition, McGraw-Hill*, **1989**.

(52) DISEG-Centro di ricerca sui ponti in muratura, Caratteristiche meccaniche della muratura, *Università degli studi di Genova*, 1-35.

(53) Novello,G.; Piumatti, P. La geometria come filo di Arianna: note di approfondimento sul rapporto ideazione-costruzione della più grande cupola di forma ovata del mondo, *Disegnarecon*, **2012**, 167-176.

(54) Cazzani, A. Statica delle murature, *Università degli studi di Cagliari,* **2006**, 1-86.

(55) Ameen, H. A., Finite element analysis of large diameter concrete spherical shell domes, *Dirasat, Engineering sciences, Vol.38, No.1*, **2011**, 85-100.

(56) Mbakogu, F. C., Pavlovìc, M. N. Bending and stretching actions in shallow domes, Part 1. Analytical Derivations, *Thin walled structures Vol.26, No.1, Elsevier Ltd.,* **1996**, 61-82.

(57) Mbakogu, F. C., Pavlovìc, M. N. Bending and stretching actions in shallow domes, Part 2. A comparative study of various boundary conditions, *Thin walled structures Vol.26, No. 2, Elsevier Ltd,* **1996**, 147-158.

(58) Sadid, H., Ghang, N. Finite element analysis of dome of a home subjected to hurricane, *SEM annual conference and exposition on experimental and applied mechanics*, **2007**, 1-9.

(59) Coan, C. H., Plaut, R. H., Dynamic stability of a lattice dome, Earthquake engineering and structural dynamics, *Vol. 11, Elsevier LTd,* **1983**, 269-274.

(60) Montes, P.; Fernandez, A. Behavior of hemispherical dome subjected to wind loading, *Journal of wind engineering and industrial aerodynamics, Elsevier Ltd.*, **2001**, 911-924.

(61) South, A.; Zweifel, C. Disaster survivability of thin-shell concrete dome structures: experience and practice, *International association for shell and spatial structures (IASS),* **2014**.